Magnetotransport Effects in Lateral and Vertical Ferromagnetic Semiconductor Junctions

Dissertation zur Erlangung des
naturwissenschaftlichen Doktorgrades
der Bayerischen Julius-Maximilians-Universität Würzburg

vorgelegt von
Christian Rüster
aus Wertheim

Würzburg, Juni 2005

Eingereicht am: 30.06.2005

bei der Fakultät für Physik und Astronomie

1. Gutachter: Prof. Dr. L.W. Molenkamp

2. Gutachter: Prof. Dr. R. Claessen

3. Gutachter: Prof. Dr. B.D. McCombe, SUNY Buffalo

der Dissertation.

1. Prüfer: Prof. Dr. L.W. Molenkamp

2. Prüfer: Prof. Dr. R. Claessen

3. Prüfer: Prof. Dr. R. Oppermann

im Promotionskolloquium

Tag des Promotionskolloquiums: 21.10.2005

Doktorurkunde ausgehändigt am: ....

Contents

Chapter 1

Introduction

A key ingredient of today's computerized society is the existence of high density nonvolatile information storage devices that are readily available to everyone. Commercially available magnetic hard disk drives nowadays offer total capacities exceeding 300 GB at prices below 0.5 \$/GB. In this respect hard disk drives are unmatched by competing storage systems and are thus dominating a multi-billion dollar market. State of the art hard disk drive read heads employ metallic multilayer components that work on the principles of electron spin dependent transport. The working principle of these multilayers exploits the giant magnetoresistance (GMR) or spin valve effect (see section 2.4) which also has a huge market potential in the field of magnetic field sensors for automotive applications. Another noteworthy magnetoresistive device is the magnetic tunnel junction, based on the tunnelling magnetoresistance (TMR) effect (see section 2.5.1). Due to superior signal levels, tunneling spin valves are a prime candidate for inclusion into future magnetic random access memory.

Fuelled by large-scale commercial exploitation and considerable scientific interest, the development of heterostructures based on ferromagnetic metals has been very rapid. Despite this, some fundamental limitations remain. Magnetic properties of metals are not tunable and integration into semiconductor devices is difficult. The novel field of spintronics tries to address these shortcomings by developing materials and devices that have ferromagnetic as well as semiconducting properties. Out of the group of ferromagnetic semiconductors one of the most promising and well understood is (Ga,Mn)As, a random alloy of the transition metal Mn with the III-V semiconductor GaAs. The first successful growth of this material dates back to as early as 1989 [Mun89]. It took a long time however until, around 2000, theoretical understanding of the rich magnetic and transport properties of the material was realized. Here the most successful and influential works are the theories of carrier mediated ferromagnetism that were independently derived by Dietl and MacDonald [Die00, Abo01]. They show that the pd-interaction between localized Mn magnetic moments and itinerant holes ensures ferromagnetism and spin polarization of the carriers at the same time. It is this interweaving of electronic and magnetic properties that makes (Ga,Mn)As a promising material for spintronics devices with novel properties not obtainable in ferromagnetic metal systems.

The usage of spin-polarized electronic currents in turn is a major goal of spintronics and a recurring theme in all parts of this thesis. The objective of the work presented in the following was to carry out an investigation of spin valve-like transport effects in and possible applications of (Ga,Mn)As based nano- and heterostructures. The initial situation in 2001 was such that

ferromagnetic (Ga,Mn)As thin films ($T_c \geq 40$ K) with metallic conduction properties could be grown reliably. With this prerequisite met, successive steps towards electronic devices were taken, the results of which are presented in the later sections of this thesis. The effort was concentrated on answering the question up to which extent (Ga,Mn)As based spintronics devices can mimic or surpass the functionalities of their metal-based counterparts. Furthermore this work was aimed at finding novel functionalities in ferromagnetic semiconductor structures. Ignoring the drawback of ferromagnetism being present only well below room-temperature, the idea was to fabricate test structures that enable the investigation of important electrical phenomena like giant magnetoresistance, tunnel magnetoresistance and the electrical resistance of magnetic domain walls. In order to fabricate efficient test structures it was also necessary to understand and at the same time to beneficially control key characteristics of the material like magnetic anisotropies and bulk magnetoresistive effects. The initial objective of this work had been to explore novel magnetoresistive effects in a ferromagnetic semiconductor. However, due to the strong interplay between magnetic and transport properties in this material, particular attention has been given to the complex characteristics of the magnetic anisotropy in the used (Ga,Mn)As thin films.

This thesis is organized as follows. Chapter 2 highlights some important fundamentals of magnetism and magnetotransport that can be understood independently of specific materials, i.e. which do not need any knowledge of the material properties of (Ga,Mn)As. The latter are given in chapter 3 along with key aspects of carrier mediated ferromagnetism. The experimental setup used for magnetotransport studies is described in chapter 4. The subsequent chapters are devoted to the experimental results obtained in the course of this Ph.D. work with bits of more specialized theoretical topics presented inside the respective chapters. Chapter 5 contains an investigation of domain-wall related magnetoresistance effects in lateral nanostructures of (Ga,Mn)As. These spin valve-like magnetoresistance effects are observed in the ballistic and tunneling regimes. They are explained using arguments based on giant magnetoresistance and tunneling magnetoresistance models. Chapters 6 and 7 both deal with vertical (Ga,Mn)As based tunnel structures and report the discovery of a novel magnetoresistive effect called tunneling anisotropic magnetoresistance (TAMR). The basic phenomenology of TAMR both in experiment as well as theory is laid out using the example of a single ferromagnet tunnel junction in chapter 6. Chapter 7 builds upon these foundations while pointing out a way to maximizing TAMR signals by using two ferromagnetic layers and an epitaxial tunnel barrier. Both TAMR related chapters supply considerable information about the magnetic anisotropy and magnetization reversal mechanisms in (Ga,Mn)As thin films. Finally, a summary of the work focussing on the novel results that were obtained is given in chapter 8.

Chapter 2

Theoretical Background

2.1 Magnetism

2.1.1 Spin and Orbital States of Electrons

From the quantum-mechanical treatment of independent atoms using the Schrödinger equation we know that electrons occupy distinct energy levels. These can be characterized by four quantum numbers:

i. The principal quantum number n with values $n = 1, 2, 3...$ determines the size of the orbit and the energy. The latter is only true for one electron travelling about the nucleus of a hydrogen atom. In case interactions with other electrons, electrical or magnetic fields are present, the energy of the electron is modified and n is no longer sufficient.

ii. The orbital angular momentum quantum number l describes the angular momentum of the electronic orbit. The number l can take any one of the values $0, 1, 2, ..., n - 1$, depending on the orbit. The orbital angular momentum $\mathbf{l}$ is a vector and its magnitude l is given by $\hbar\sqrt{l(l+1)}$. Often, electrons with $l = 0, 1, 2, 3, 4, ...$ are referred to as $s, p, d, f, g, ...$ electrons, respectively.

iii. The magnetic quantum number l_z describes the projection of the orbital angular momentum along a particular quantization direction. In most cases, this direction is chosen as the direction of an existing external or internal magnetic field. For a given value of l, l_z can assume the values $l_z = -l, -l + 1, ...0, ..., l - 1, l$.

iv. In a classical picture, the spin quantum number s describes the component of the electron spin vector $\mathbf{s}$ along a particular direction, for example the direction of an applied field. Spin is the intrinsic angular momentum stemming from the rotation of an electron about an internal axis. The allowed values are $s = \pm 1/2$.

Just as classical current that flows along a wire, an atomic orbit of an electron carries with it a magnetic moment μ. An electron characterized by the orbital angular momentum quantum number l has an associated magnetic moment

$$\mu_l = -\frac{e}{2m}\hbar\mathbf{l} = -\mu_B\mathbf{l}, \tag{2.1}$$

with μ_B the Bohr magneton. Its projection along the direction of the applied field is

$$\mu_{l,z} = -l_z \mu_B. \tag{2.2}$$

For the spin angular momentum, the situation is slightly different. Here the associated magnetic moment is

$$\mu_s = -g_e \mu_B \mathbf{s}, \tag{2.3}$$

where $g_e = 2.002290716(10)$ is the g-factor for the free electron. The component along the field direction is

$$\mu_{s,z} = -g_e s \mu_B. \tag{2.4}$$

The energy of a magnetic moment μ in a magnetic field $\mathbf{H}$ is given by the Hamiltonian

$$H = -\mu_0 \mu \cdot \mathbf{H} = -\mu \cdot \mathbf{B}, \tag{2.5}$$

where $\mathbf{B}$ is the magnetic flux density and $\mu_0 = 4\pi \cdot 10^{-10} TA^{-1}$ is the permeability of vacuum.

2.1.2   Ground State of Ions with a Partially Filled Shell: Hund's Rules

Suppose we have an atom or ion in which all electronic shells are filled or empty except for one. Suppose also that this shell is characterized by an orbital angular momentum l. For a given l, there are $2l+1$ values for l_z and additionally the two spin orientations corresponding to $s = \pm 1/2$. Since electrons have to obey Pauli's principle according to which they have to differ from each other in at least one quantum number, the maximum number of electrons in the shell is $2(2l+1)$. Because the electrons interact with each other, the various ways of arranging n electrons in more than n states are not energetically degenerate. When searching for the ground state of the magnetic ion, both complex quantum-mechanical calculations and the analysis of atomic spectra have shown that (except for the heaviest ions) three simple rules determine the lowest lying states.

i. *Russell-Saunders Coupling* The total orbital angular momentum of the atom is given by $\mathbf{L} = \sum_i \mathbf{l}_i$, where i extends over the whole number of electrons. Equivalently the total spin angular momentum is given by $\mathbf{S} = \sum_i \mathbf{s}_i$. In both cases, the total moment of a fully filled shell is zero. The spin-orbit interaction is the coupling mechanism between $\mathbf{L}$ and $\mathbf{S}$. Together, they form the resulting total angular momentum $\mathbf{J} = \mathbf{L} + \mathbf{S}$.

ii. *Hund's First Rule* Electrons are subsequently filled into empty states according to the rule that $\mathbf{S}$ takes its maximum value as far as allowed by the exclusion principle.

iii. *Hund's Second Rule* The value of $\mathbf{L}$ also takes its maximum as far allowed by Hund's First Rule.

iv. *Hund's Third Rule* Obeying Hund's first two rules that govern $\mathbf{L}$ and $\mathbf{S}$ still leaves $(2L+1)(2S+1)$ possible states. Their degeneracy is lifted by the spin-orbit coupling. The spin orbit term in the Hamiltonian is of the form $\lambda(\mathbf{L} \cdot \mathbf{S})$ and it favors maximum $\mathbf{J}$ (parallel $\mathbf{L}$ and $\mathbf{S}$) if λ is negative and minimum $\mathbf{J}$ (antiparallel $\mathbf{L}$ and $\mathbf{S}$) if λ is positive. Since λ is

positive for shells that are less than half filled and negative for shells that are more than half filled, the lowest state of energy is characterized by

$$J = |L - S|, \ n \leq (2l + 1)$$
$$J = L + S, \ n \geq (2l + 1). \tag{2.6}$$

2.1.3 Paramagnetism of Insulators Containing Ions with a Partially Filled Shell

The following analysis applies for materials with noninteracting permanent magnetic moments. In reality this can be a system of isolated atoms or insulating crystals containing magnetic ions[1].

Once Hund's rules have been applied to find the quantum numbers J, L, S of the ground-state multiplet of a given atom that is part of an ensemble, the magnetic properties of the whole system can be described on the basis of these quantum numbers and the numbers of atoms N in the system alone.

Suppose the shell of an atom under investigation has $J \neq 0$. When Russell-Saunders coupling applies, this is the case for all electronic configurations except closed shells and shells that are just one electron short of being half filled. If a quantization axis (e.g. an external magnetic field H) along the z-direction is present, the z-component of this atom may adopt $2J + 1$ values ($m_j = -J, -J + 1, ...0, ..., J - 1, J$) and these values are no longer degenerate. They are given by

$$E_H = -\mu_0 \boldsymbol{\mu} \cdot \mathbf{H} = -\mu_0 \mu_z H = g(JLS) m_J \mu_0 \mu_B H, \tag{2.7}$$

where $\boldsymbol{\mu}$ is the atomic magnetic moment vector, μ_z is its component along the field direction and

$$g(JLS) = 1 + \frac{J(J+1) + S(S+1) - L(L+1)}{2J(J+1)} \tag{2.8}$$

is the Landé g-factor. For sufficiently low temperatures, only the $2J + 1$ lowest states of the atoms are populated with appreciable probability. The magnetization density $M(H)$ of this system of discrete states is defined in thermodynamics as

$$M = -\frac{1}{V} \frac{\partial F}{\partial H}, \tag{2.9}$$

where F is the magnetic Helmholtz free energy and V is the volume of the quantum-mechanical system. The Helmholtz free energy is given by the statistical rule

$$e^{-F/k_B T} = \sum_n e^{E_n(H)/k_B T}, \tag{2.10}$$

with the Boltzmann constant $k_B = 1.3806505(24) \cdot 10^{-23} J K^{-1}$. The index n takes on the values $n = 0, 1, ...$; E_0 is the ground state energy and higher n correspond to the energies of the excited states of the system. For the case of the $2J + 1$ angular momentum multiplet, the free energy can be calculated from

$$e^{-\beta F} = \sum_{m_j = -J}^{J} e^{-\beta \gamma H m_j}, \quad \gamma = g(JLS) \mu_B, \quad \beta = \frac{1}{k_B T} \tag{2.11}$$

---

[1]The analysis holds well for rare earth ions in insulating crystals. Out of the group of transition metals it only holds well for Mn^{2+} and Fe^{3+}. For details refer to [Ash76].

This represents a geometric series whose sum is

$$e^{-\beta F} = \frac{e^{\beta \gamma H (J+1/2)} - e^{-\beta \gamma H (J+1/2)}}{e^{\beta \gamma H/2} - e^{-\beta \gamma H/2}}. \tag{2.12}$$

With Equ. 2.9, the definition for the magnetization of N such atoms in a volume V one gets

$$M = \frac{N}{V} \gamma J B_J(\beta \gamma J H), \tag{2.13}$$

where the Brillouin function $B_J(x)$ is defined as

$$B_J(x) = \frac{2J+1}{2J} coth \frac{2J+1}{2J} x - \frac{1}{2J} coth \frac{1}{2J} x. \tag{2.14}$$

Another way of analyzing a paramagnetic system is by means of their magnetic susceptibility χ that is defined as

$$\chi = \frac{\partial M}{\partial H} = -\frac{1}{V} \frac{\partial^2 F}{\partial H^2}. \tag{2.15}$$

In the high temperature limit, when the thermal energy by far exceeds the level splitting ($k_B T \gg \gamma H$), the susceptibility takes an especially simple and useful form. Using the small-x expansion of the Brillouin function (Equ. 2.14)

$$B_J(x) \approx \frac{J+1}{3J} x + O(x^3), \tag{2.16}$$

and taking the derivative of the magnetization $M(T,H)$ with respect to H, one gets the high temperature susceptibility

$$\chi = \frac{N}{V} \frac{(g(JLS)\mu_B)^2}{3} \frac{J(J+1)}{k_B T}, \quad (k_B T \gg \gamma H). \tag{2.17}$$

This dependence of the susceptibility of paramagnetic systems with permanent magnetic moments on the inverse of the temperature is known as Curie's law.

2.1.4 Ferromagnetism

The Exchange Interaction

Some solids, called ferromagnets, are characterized by a nonzero magnetic moment even in the absence of an external magnetic field. This spontaneous magnetization M_s can not be explained within the theory of paramagnetism that was derived in the previous section, as seen from the $H = 0$ limit of Equ. 2.13.

Paramagnetism was derived under the assumption that the microscopic magnetic moments in the solid do not interact with one another. In ferromagnetic substances however, this assumption no longer applies. M_s is caused by a long range order of the magnetic moments that is induced by a strong interaction energy. Classically, one would perhaps expect that this energy is the magnetic dipolar interaction. However, it can easily be estimated that the order of magnitude of this effect for two magnetic moments with $\mu \approx 1\mu_B$ that are separated by $r \approx 1\text{Å}$ is

equivalent to 1 K in temperature [Blu01]. This can certainly not account for the magnetic ordering in many materials which persists up to much higher temperatures (in some cases up to ≈ 1000 K).

A much higher energy contribution comes from the quantum mechanical phenomenon of exchange interaction. To understand exchange interactions, we consider a hydrogen-like molecule with two electrons as a simple starting point. We will see how the Pauli principle can lead to magnetic effects in such a system, even though only a spin-independent Hamiltonian is used. The starting point is to consider a molecule as sketched in Fig. 2.1, where nuclei A and B with
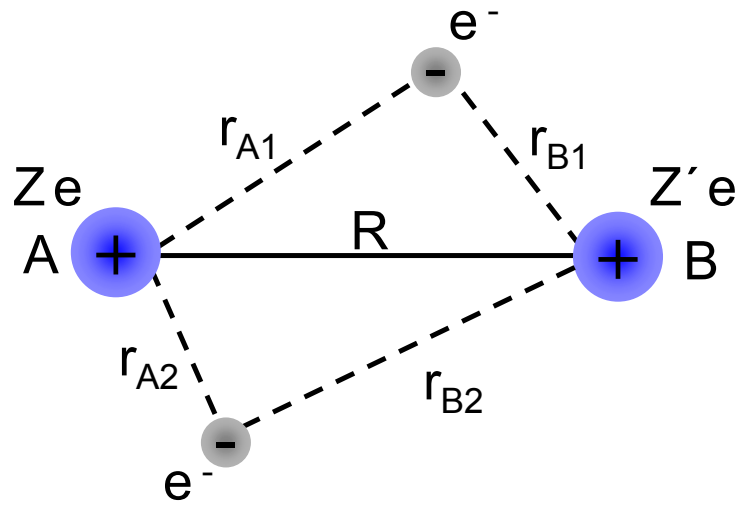
Figure 2.1: Sketch of a hydrogen-like molecule serving as the model system to derive the exchange interaction between two independent electrons.

charges Z, Z' are separated by a distance R. When two electrons 1 and 2 are bound to the nuclei, the spin-independent Hamiltonian $H(1,2)$ of the system can be decomposed into three parts

$$H(1,2) = H(1) + H(2) + H_{int}(1,2).$$ (2.18)

Here, $H(1)$ and $H(2)$ are the one-electron Hamiltonians of the form

$$H(i) = -\frac{\hbar^2}{2m}\nabla_i^2 - \frac{Ze^2}{4\pi\varepsilon_0 r_{Ai}} - \frac{Z'e^2}{4\pi\varepsilon_0 r_{Bi}} + \frac{ZZ'^2}{8\pi\varepsilon_0 R}, \quad i = 1,2$$ (2.19)

which contain the Coulomb energies of the electrons in the electrical field of the nuclei. Note that the Coulomb interaction between the nuclei is equally distributed into both one-electron Hamiltonians. $H_{int}(1,2)$ is the residual interaction between the electrons. In the following, we choose the independent electron approximation, neglecting $H_{int}(1,2)$ and retaining only the interaction of each electron with the two nuclei. Then the remaining Hamiltonian is a sum of one-electron Hamiltonians. We can then solve the Schrödinger equation using total orbital wavefunctions constructed from the product of the well-known one-electron solutions[2]. The

---

[2]For the solution of the Schrödinger equation of one-electron atoms refer to [Bra83], for example.

ground state wave function would then be

$$\Psi(1,2) = [\Phi_A(1) + \Phi_B(1)][\Phi_A(2) + \Phi_B(2)]. \tag{2.20}$$

Expanding the product, this reads

$$\Psi(1,2) = \Phi_A(1)\Phi_A(2) + \Phi_A(1)\Phi_B(2) + \Phi_B(1)\Phi_A(2) + \Phi_B(1)\Phi_B(2). \tag{2.21}$$

Terms one and four correspond to both electrons being located on the same nucleus, which is a natural consequence of neglecting the Coulomb repulsion between the electrons. However, for a real system this is a poor postulate. Therefore, we omit these ionic states completely, which leads to the Heitler-London approximation

$$\Psi(1,2)_s = \Phi_A(1)\Phi_B(2) + \Phi_B(1)\Phi_A(2). \tag{2.22}$$

It can be easily seen that this orbital part of the wave function is symmetric with respect to the coordinates of the electrons. The total wavefunction including spin is just the product of orbital and spin part. The generalized Pauli principle states that the total wave function, including the spin part must be antisymmetric under the exchange of both spin and orbital coordinates of the electrons. Consequently, the symmetric wave function in Equ. 2.22 must belong to an antisymmetric spin state (a singlet with antiparallel spin orientation). A triplet state with parallel spin orientation is described by an orbital wave function that is antisymmetric, i.e.

$$\Psi(1,2)_t = \Phi_A(1)\Phi_B(2) - \Phi_B(1)\Phi_A(2). \tag{2.23}$$

The last step is to calculate the expectation value of the energy difference between the singlet and the triplet configuration,

$$E_s - E_t = \frac{<\Psi(1,2)_s|H(1) + H(2)|\Psi(1,2)_s>}{<\Psi(1,2)_s|\Psi(1,2)_s>} - \frac{<\Psi(1,2)_t|H(1) + H(2)|\Psi(1,2)_t>}{<\Psi(1,2)_t|\Psi(1,2)_t>}. \tag{2.24}$$

In the limit of large spatial separations this splitting reduces to the expression

$$J = E_s - E_t = 2\int dr_1 dr_2 [\Phi_{A1}(r_1)\Phi_{B2}(r_2)](\frac{e^2}{r_{12}} + \frac{e^2}{R_{AB}} - \frac{e^2}{R_{A1}} - \frac{e^2}{R_{B2}})[\Phi_{A1}(r_1)\Phi_{B2}(r_2)]. \tag{2.25}$$

The quantity J is called the exchange constant and gives the energy difference between antiparallel and parallel alignment of the electron spins. This difference is also referred to as an exchange splitting or as an exchange interaction. For the simple hydrogen-like molecule investigated here, it is always negative, meaning that the singlet state is the ground state.

2.1.5 The Heisenberg Spin Hamiltonian

When considering Equ. 2.25 for the exchange splitting of a simple two electron system, one notices that only electrostatic interactions appear as the driving force for magnetic ordering. Therefore the exchange splitting should also be of the order of electrostatic energy differences and in many cases it can be the dominant energy contribution. However, there is a model Hamiltonian which only affects the spin functions and produces the same splitting between the energy levels for parallel and antiparallel orientations.

This so called Heisenberg spin Hamiltonian is of the form

$$H_{spin} = -J\mathbf{S_1} \cdot \mathbf{S_2},$$
(2.26)

with $J = E_s - E_t$ the exchange splitting of the system and $\mathbf{S_1}, \mathbf{S_2}$ the spin operators of the pair of interacting particles. To demonstrate that this Hamiltonian correctly describes the exchange splitting of our two-electron system, consider that the square of the total spin angular momentum operator $\mathbf{S}^2$ is given by

$$\mathbf{S}^2 = S_x{}^2 + S_y{}^2 + S_z{}^2,$$
(2.27)

with eigenvalues for any spin state $|\Psi >$

$$\mathbf{S}^2|\Psi >= (S_x{}^2 + S_y{}^2 + S_z{}^2)|\Psi >= \left(\frac{1}{4} + \frac{1}{4} + \frac{1}{4}\right) = \frac{3}{4}|\Psi > .$$
(2.28)

Of course this can be applied for particles with spin quantum number $s > \frac{1}{2}$ as the eigenvalue of $\mathbf{S}^2$ generally is $s(s+1)$. Since each individual electron spin operator satisfies the above condition, the total spin $\mathbf{S_t}$ for the two coupled electrons satisfies

$$\mathbf{S_t}^2 = (\mathbf{S_1} + \mathbf{S_2})^2 = \frac{3}{2} + 2\mathbf{S_1} \cdot \mathbf{S_2}.$$
(2.29)

Since $\mathbf{S_t}^2$ has the eigenvalue $S(S+1)$ in states of spin S, it follows by comparison with Equ. 2.29 that the operator $\mathbf{S_1} \cdot \mathbf{S_2}$ has an eigenvalue of $-\frac{3}{4}$ in the singlet state ($S = 0$) and $+\frac{1}{4}$ in the triplet state ($S = 1$). Thus an operator of the form

$$H_{spin} = \frac{1}{4}(E_s + 3E_t) - (E_s - E_t)\mathbf{S_1} \cdot \mathbf{S_2}$$
(2.30)

has eigenvalue E_s in a singlet spin configuration and E_t in any of the three triplet states. By simply redefining the zero of energy we can omit $\frac{1}{4}(E_s + 3E_t)$, which is a constant energy offset common to all four states. The remaining part is the spin Hamiltonian in the form of Equ. 2.26.

The spin Hamiltonian depends only on the relative orientation of the two spins. It contains the scalar product of the vector spin operators $\mathbf{S_1}$ and $\mathbf{S_2}$ and thus it will favor parallel alignment if J is positive and antiparallel alignment if J is negative. The main advantage of using the spin Hamiltonian arises for systems where the number of magnetic moments N is large. When N ions with spin S are widely separated, the ground state of the system is $(2S + 1)^N$-fold degenerate. When the states are closer together, exchange interaction plays a role and the ground state is split. Quite remarkably, in many cases an adequate operator function of the spin operators S_i, is simply the expression

$$H_{spin} = -\sum_{i,j} J_{ij}\mathbf{S_i} \cdot \mathbf{S_j},$$
(2.31)

with J_{ij}, the exchange coupling constants This is known as the Heisenberg Hamiltonian and it has the form of the two-spin case described by Equ. 2.26, summed over all pairs of magnetic moments.

Mean Field Theory

The earliest and simplest approach to a quantitative analysis of the ferromagnetic transition temperature is due to Pierre Weiss and it is known as mean (or molecular) field theory. Its starting point is to state that in ferromagnets there exists an internal effective magnetic field, that interacts with the existing magnetic moments. This so-called molecular field is responsible for long range order and spontaneous magnetization.

Consider the Heisenberg Hamiltonian in Equ. 2.31. The Heisenberg Hamiltonian of an individual spin $\mathbf{S}_0$ in an external magnetic field $\mathbf{H}$ is

$$H_0 = -g\mu_B \mathbf{S}_j \cdot \mathbf{H} + \mathbf{S}_j \sum_{i \neq i_0} J_i \mathbf{S}_i, \tag{2.32}$$

where i sums over all lattice sites except the one occupied by spin $\mathbf{S}_0$. This is the form of the energy of a spin in an effective external magnetic field

$$\mathbf{H_{eff}} = \mathbf{H} + \frac{1}{g\mu_B} \sum_{i \neq j} J_i \mathbf{S}_i. \tag{2.33}$$

However, H_{eff} is an operator that depends in a complex way on the microscopic configurations of all the spins on all the lattice sites. However, instead of treating the spins individually and microscopically, one can use the thermal equilibrium mean value. This is called the mean field approximation and in the case of a ferromagnet, every spin has the same mean value which can be expressed in terms of the total volume magnetization by

$$< \mathbf{S}_i > = \frac{V}{N} \frac{\mathbf{M}}{g\mu_B}. \tag{2.34}$$

The effective field is thus transformed into the expression

$$\mathbf{H_{eff}} = \mathbf{H} + \lambda \mathbf{M}, \quad \lambda = \frac{V}{N} \frac{\sum_i J_i}{(g\mu_B)^2}. \tag{2.35}$$

Since this mean field theory assumes that the only effect of interactions is to replace the external field by the effective field $\mathbf{H}_{eff}$, we can continue the analysis analogous to the previous section of paramagnetism. By replacing 2.35 into Equ. 2.13 it follows for the sample magnetization that

$$M = M_0 \left(\frac{H_{eff}}{T} \right), \tag{2.36}$$

where M_0 is the magnetization density in the external field H and temperature T as calculated above for the case without magnetic interactions. Equ. 2.36 is an implicit expression for the magnetization M as a function of temperature T that can be solved numerically in a self-consistent way. The temperature dependence of the spontaneous magnetization ($M_s(H = 0)$) can be evaluated with a graphical method that is demonstrated in Fig. 2.2. Since $H_{eff} = \lambda M$ when $H = 0$, it follows that

$$M(T) = M_0 \left(x = \frac{\lambda M}{T} \right), \ and \ M(T) = \frac{T}{\lambda} x. \tag{2.37}$$
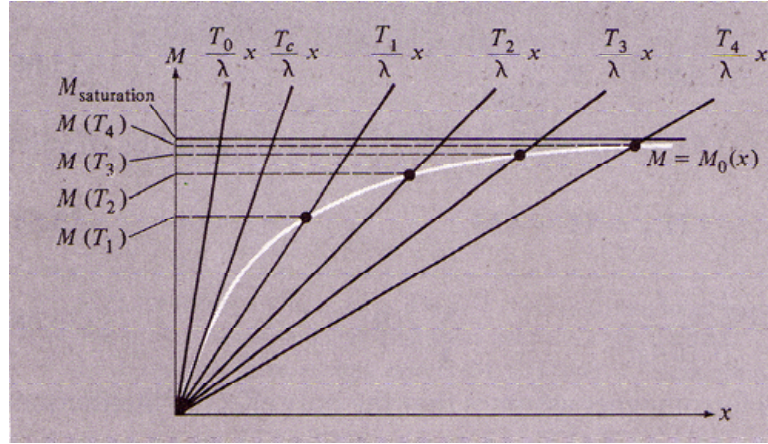
Figure 2.2: Graphical Method to determine the spontaneous magnetization of a ferromagnet in mean field theory (taken from [Ash76]).

The graphical solution for these two equations is displayed in Fig. 2.2. Solutions occur whenever $M_0(x)$ intersects one of the lines with slope $\frac{T}{\lambda}x$. From the graph it is clear that for high temperatures, the slope of the straight line is bigger than the slope of the Brillouin function at $x = 0$. Thus, as in the case of temperature T_0, there is only an intercept at the origin, where $M_s = 0$. At low temperatures and $x = 0$, the slope of the straight line is smaller than the slope of the Brillouin function. These temperatures correspond to the ferromagnetic region with nonzero M_s. In this interval, there are two solutions, one for $M_s = 0$ and the other one corresponding to $M_s \neq 0$. The solution for $M_s = 0$ is unstable, as it is clear that in the presence of net ferromagnetic interactions any fluctuation of the system will result in a nonzero value of the sample magnetization[3]. The other solution is stable and it is the desired value of the magnetization. The critical temperature or Curie temperature T_c corresponds to the special case of identical slopes of the two functions at x=0. In this case

$$\frac{T_c}{\lambda} = \frac{N}{V} \frac{(g\mu_B)^2}{3k_B} S(S+1), \tag{2.38}$$

where we have used the small x series expansion of the Brillouin function given by Equ. 2.16 and Equ. 2.37. The mean field expression for the critical temperature T_c thus becomes

$$T_c = \frac{N}{V} \frac{(g\mu_B)^2}{3k} S(S+1)\lambda = \frac{S(S+1)}{3k_B} J_0. \tag{2.39}$$

Figure 2.3 displays the temperature dependence of the mean field solution of the spontaneous magnetization of ferromagnets for a range of values of J. The y-scale is normalized by the saturation value M_s. It can be seen that the magnetization is nonzero below the critical temperature T_c and zero above. The magnetization is continuous at T_c but its derivative with respect to temperature is not. This classifies the ferromagnetic to non-magnetic phase transition as a second-order phase transition, i.e. there is no latent heat.

---

[3]In this simple system, magnetic domains are neglected.
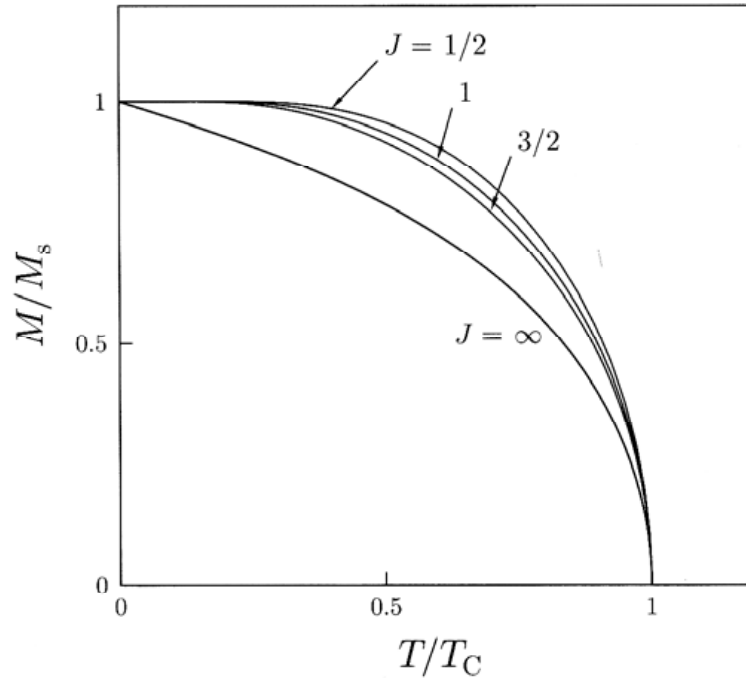
Figure 2.3: The mean-field magnetization as a function of temperature, deduced for different values of J. Figure taken from [Blu01].

2.2 Transport Effects in Magnetic Materials

2.3 The Anisotropic Magnetoresistance Effect

In 1857, William Thomson discovered that the resistance of iron and nickel depends on the angle enclosed between the current path and the direction of the magnetization [Tho57]. This bulk magnetoresistance effect is called anisotropic magnetoresistance (AMR). It is especially well known in ferromagnetic 3d metals but is also present in (Ga,Mn)As [Wan02]. The microscopic origin of AMR is anisotropic scattering of the charge carriers due to spin-orbit interaction [McG75]. The resistance change due to the AMR effect is typically on the order of a few percent in (Ga,Mn)As.

In materials that exhibit AMR, the electrical resistivity $\rho_\parallel$ for current flowing along the magnetization direction of a magnetic domain is not the same as for current flowing perpendicular to the domain orientation ($\rho_\perp$). This behavior is shown schematically in Fig. 2.4 for a hypothetical ferromagnetic sample that is supposed to be in a multi-domain state before the magnetoresistance measurement. The two curves correspond to the resistivity of this sample, measured in magnetic fields parallel ($\parallel$) and perpendicular ($\perp$) to the current path, respectively. The resistance at zero magnetic field is the same, because the two initial magnetic configurations are assumed to be identical. For increasing magnetic fields, the two curves move apart, because more and more domains align along the external field. At sufficiently high magnetic fields all the domains in the sample point along the applied magnetic field and both curves have

approached the final resistivity values of $\rho_{\parallel}$ and $\rho_{\perp}$, respectively. Note that this effect also occurs in the absence of an external magnetic field, for different orientations of the spontaneous magnetization of the ferromagnet.
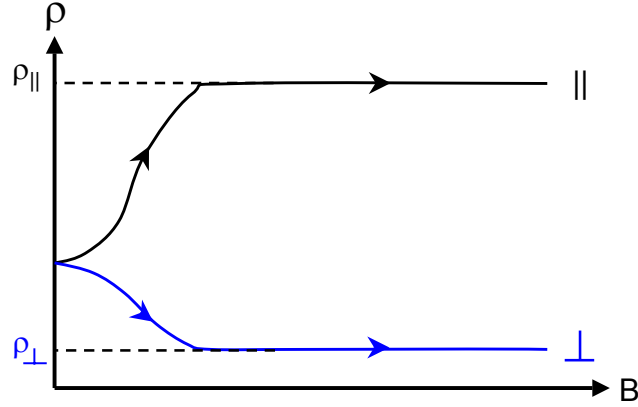

Figure 2.4: Schematic depicting the anisotropic magnetoresistance of a ferromagnetic multidomain sample. For simplicity it is assumed that the initial magnetic configurations are identical before the start of each magnetoresistance sweep.

For arbitrary angles θ between the direction of the sample magnetization **m** and the current density **j**, the electrical field due to the AMR effect is given in vector form by

$$\mathbf{E} = \rho_{\perp}\mathbf{j} + [\rho_{\parallel} - \rho_{\perp}][\mathbf{m} \cdot \mathbf{j}]\mathbf{m} + \rho_H \mathbf{m} \times \mathbf{j}, \tag{2.40}$$

where the last term gives the anomalous or extraordinary Hall electric field [McG75]. When multiplying this expression with $\mathbf{j}/j^2$ one gets

$$\rho(\theta) = \rho_{\perp} + (\rho_{\parallel} - \rho_{\perp})cos^2(\theta), \tag{2.41}$$

the resistance of the sample as a function of the angle between the magnetization direction and the electric current. This simple $cos^2(\theta)$ dependence can be easily employed to build sensitive magnetic field sensors and was a concept used in the early hard disk drives for computers.

In a laboratory environment, the AMR effect can be a useful tool in the characterization of unknown ferromagnetic layers like (Ga,Mn)As for example. Provided the sample under investigation behaves as a single domain and AMR is the dominant contribution to the magnetoresistance of the layer, the knowledge of Equ. 2.41 can be used to extract detailed information about the magnetic anisotropy from transport measurements alone. First, one has to acquire the values for $\rho_{\parallel}$ and $\rho_{\perp}$ by saturating the sample magnetization in high external magnetic fields of the appropriate directions and then one measures the resistance. While the magnetic field is lowered back to zero along a well-defined path, the magnetization settles on the energetically most favorable easy axis. The relative orientation of this anisotropy axis with respect to the current direction can then be easily deduced using Equ. 2.41 and the experimentally extracted resistance anisotropy.

2.4 The Giant Magnetoresistance Effect

2.4.1 Phenomenology

In contrast to the AMR effect described in the previous section, the Giant Magnetoresistance (GMR) effect occurs in magnetic multilayers. It is the increase of the resistance of adjacent magnetic layers upon the change of the alignment of their magnetizations from parallel to antiparallel. GMR was first reported in multilayered Fe/Cr magnetic structures by Baibich et al. [Bai88] and by Binasch et al. [Bin89]. A prototypical GMR structure using the minimum amount of layers needed to measure the effect is displayed in Fig. 2.5.
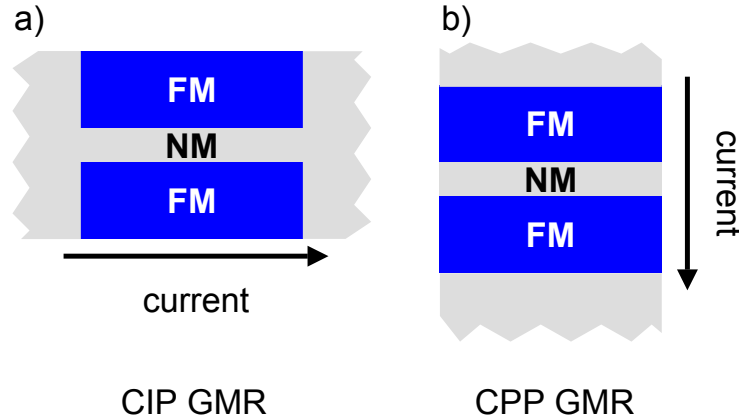
Figure 2.5: Giant Magnetoresistance is an effect occurring in structures consisting of alternating layers of ferromagnets (FM) and thin nonmagnetic spacers (NM). The effect can be measured in two different geometries, CIP-GMR with the electrical current in the plane of the layers (a) and CPP-GMR with the current perpendicular to the interfaces (b).

As can be seen, a thin nonmagnetic spacer layer is sandwiched between two ferromagnetic layers. There are two geometries in which GMR can be measured: the current-in-plane (CIP) and the current-perpendicular-plane (CPP) geometry. In both geometries, the resistance of the transport structures depends on the relative orientation of the magnetizations of neighboring ferromagnets: the resistance is high for antiparallel alignment of the magnetizations and it is low for parallel alignment. Accordingly, the GMR ratio is defined as

$$GMR = \frac{R_{ap} - R_p}{R_p},\tag{2.42}$$

with R_{ap} the resistance in the antiparallel state and R_p the parallel state resistance. Generally, the GMR ratio is a positive number that increases with decreasing temperature and it is higher for CPP than for CIP-GMR.

Some early GMR measurement curves are shown in Fig. 2.6. Fig. 2.6a is measured on Fe/Cr superlattices with 30,35 and 60 periods, where the thickness of the nonmagnetic spacer is 18Å, 12Å and 9Å, respectively. This is taken from the original publication of Baibich et al. [Bai88].
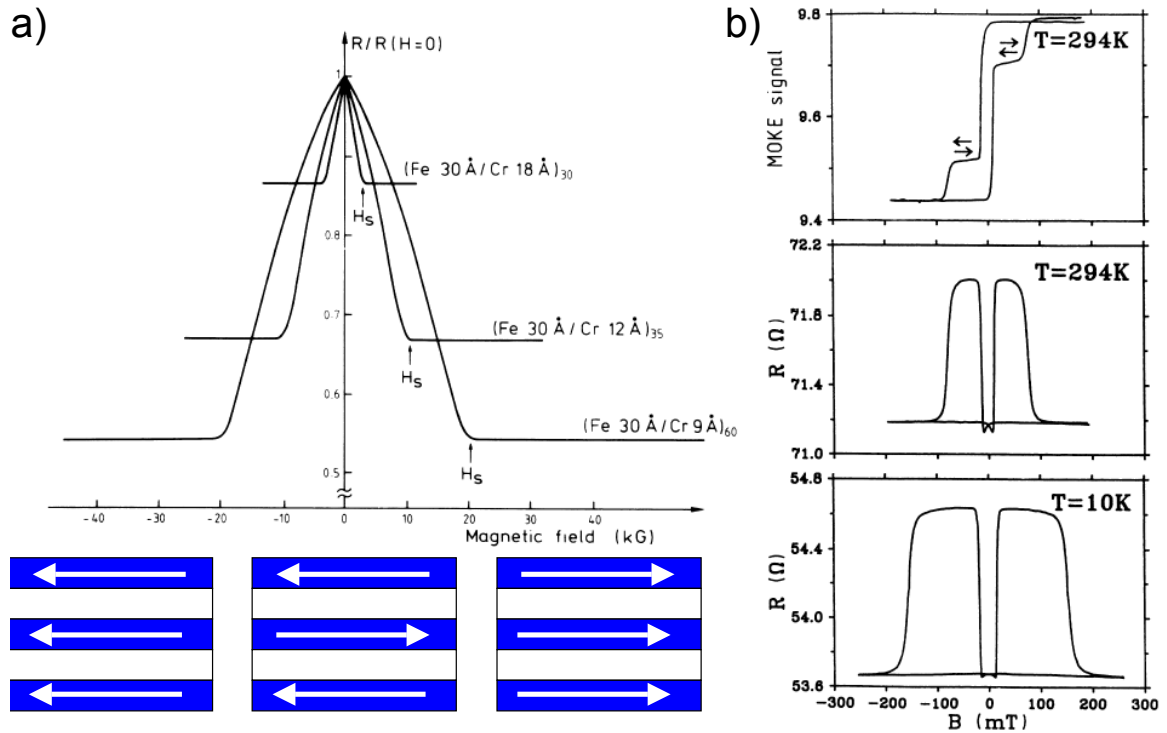
Figure 2.6: a) Magnetoresistance of three Fe/Cr multilayers with different Cr spacer thicknesses. The strong variation of the resistance is due to the Giant Magnetoresistance Effect. Adjacent Fe layers couple antiferromagnetically, creating a high resistance state at zero magnetic field. Curve taken from [Bai88]. b) From top to bottom: MOKE signal, magnetoresistance at 294K and 10K on a Co/Au/Co GMR structure. Curves taken from [Bar90].

The magnetic field and the current are both aligned along the same [110] crystallographic direction. For all three spacers, the resistance has a maximum at zero magnetic field. This state corresponds to antiparallel alignment of neighboring ferromagnets, as sketched below the data. The reason for this is that for the range of thicknesses chosen for the spacer layer in this experiment, the magnetic layers exhibit antiferromagnetic exchange coupling. When the field is increased along either the positive or the negative direction, the ferromagnets align increasingly collinear, indicated by the monotonically decreasing resistance. The change in resistance increases for decreasing spacer thickness. At high enough magnetic fields, all layers are fully aligned in parallel and the low resistance state is reached.

However, antiferromagnetic coupling between the ferromagnets is not a necessary condition for the GMR effect. Building a magnetic multilayer that does not show interlayer coupling simply results in a different shape of the magnetoresistance curve, as depicted in Fig. 2.6b. The data shown here was measured on a Co/Au/Co trilayer evaporated on a [110]-oriented GaAs substrate [Bar90]. To create both the antiparallel and the parallel alignment state between the layers, this sample relies on the different coercive fields of the two Fe layers instead. Since the lower Co layer was grown on a GaAs surface and the upper one is grown on Au, both layers exhibit slightly different magnetic properties, i.e. coercivities. Another way to state this

is to say that the layer with higher coercivity is magnetically "hard" the other one is "soft". The magnetoresistance of such a system without interlayer exchange coupling leads to the so-called spin valve feature shown in the middle and lower panels of Fig. 2.6b for two different temperatures. At high negative magnetic fields, both magnetizations are aligned in parallel and pointing along the field direction. The sample is in the low resistance state. When the magnetic field is increased, the layers remain in parallel until at small positive magnetic fields the Co layer with the smaller coercive field reverses its magnetization. This shows up as a simultaneous step in the magnetization measurement of the top panel in Fig. 2.6b and an abrupt switch to the high resistance state. At slightly higher positive values of the field, the second layer also reverses the magnetization and the sample returns into the low resistance state. It is thus due to the different magnetic anisotropy that the effect is the inverse of the data shown in Fig. 2.6a, the underlying transport mechanism is the GMR effect in both cases.

Another common scheme to create a hard and a soft magnetic layer is to pin one of the ferromagnetic layers with an adjacent antiferromagnet. In 1998, IBM successfully implemented this idea into GMR based read heads in magnetic hard disk drives [Bel05]. Compared to the previously available AMR based read heads, this has lead to a much increased magnetic field sensitivity and therefore much higher data storage capability. Since that time GMR read heads have become the industry standard in the multi-billion dollar magnetic storage industry. This incredible success has since been one of the major motivations for increased research in spintronics.

2.4.2   Simple Model of CPP GMR

In the previous section it was stated that the phenomenology of the GMR effect, i.e. a change in resistance upon a change in magnetization of one of the magnetic layers, is the same for both CIP and CPP GMR. In contrast to that, the physical interpretation of the resistance change is quite different. Among the relevant mechanisms for CPP-GMR are spin injection and accumulation between adjacent layers. Thus, the critical length scale for the effect is the spin flip length l_{sf}. It is clear from comparing the two different geometries that spin injection can not be a pertinent mechanism in the CIP geometry, since the current runs parallel to the layers. In CIP-GMR the scaling length is given by the ballistic mean free path [Har00, Fer94]. In the following, the discussion will be limited to the CPP geometry and the corresponding Valet-Fert model for spin injection, because it is the pertinent geometry for the interpretation of the domain wall resistance results presented in section 5.6.

The basis for the understanding of many aspects of spin-polarized transport including GMR was set in 1936 by the work of Mott [Mot36a, Mot36b]. Mott tried to explain the increase in resistivity of ferromagnetic metals above the Curie temperature. The main point of his idea is that the electrical conductivity in these spin-polarized ferromagnetic metals can be described in terms of two largely independent conduction channels, one for spin-up carriers and one for spin-down carriers. Here, spin-up and spin-down refers to the projection of the carrier spin with respect to the magnetization of the magnet. This picture is applicable as long as there is only small mixing between the majority and minority spins. This is usually true for sufficiently low temperatures, where the probability of a spin-flip scattering process in metals is normally small compared to the probability of a spin-conserving scattering event. Consequently, spin up and spin down carriers contribute to electrical conduction in parallel at least on the length scale of
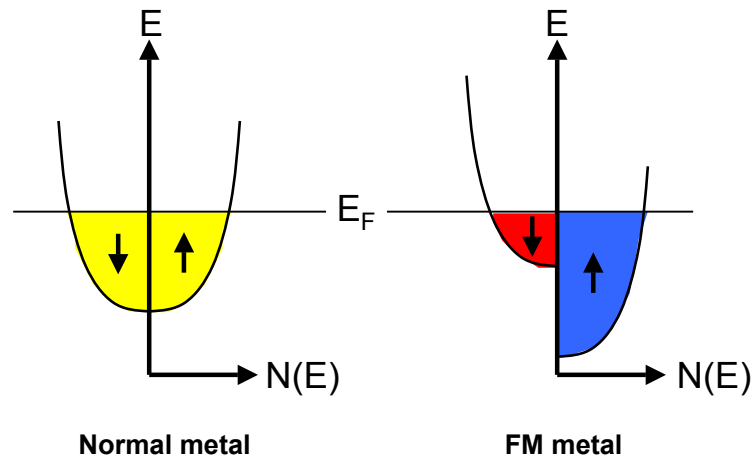
the spin-flip length.

Figure 2.7: Schematic Representation of the density of states (DOS) $N(E)$ in a normal metal (left) and a ferromagnetic metal (right). It can be seen that the DOS at E_F is the same for both spins in a normal metal and that the ferromagnetic metal has a net spin polarization.

Correspondingly, carrier states in metals can be ascribed to spin-dependent density of states (DOS) as depicted in Fig. 2.7 for a nonmagnetic and a ferromagnetic metal. A nonmagnetic metal has equal numbers of spin up and spin down electrons at the Fermi energy. In contrast, a ferromagnetic metal has more spins of one orientation than the other due to the spin splitting stemming from exchange interactions. Thus, there is a nonzero spin polarization at the Fermi edge.

From this starting point, it is possible to formulate an intuitive model of GMR in a very straightforward way. The spin asymmetry of the DOS can be analyzed in analogy with an experiment using polarized light. The device under consideration is the two terminal GMR device depicted in Fig. 2.8. For simplicity it is assumed that the ferromagnets in the GMR trilayer are half-metallic, i.e. in the DOS at the Fermi energy there is a partially filled band for the majority spin carriers and a forbidden gap for the minority carriers. In this case, when an appropriate voltage is applied to the structure, a spin polarized current consisting only of majority spin carriers is injected from the left into the nonmagnetic spacer. This causes a net spin accumulation in the nonmagnetic metal to appear. This spin accumulation decays with increasing distance from the interface. If the thickness of the spacer is smaller than or comparable to the spin-flip length in the material, a nonzero spin accumulation will reach the interface with the ferromagnet on the right. The left ferromagnet thus acts as a polarizer by presenting different amounts of spin up and down electrons to the one on the right. The latter then takes the role of the analyzer as it transmits different currents depending on its magnetization direction relative to the polarizer. From this simple model it is clear that the resistance of a GMR device follows a cosine behavior, as the "extinction angle" is $180°$.
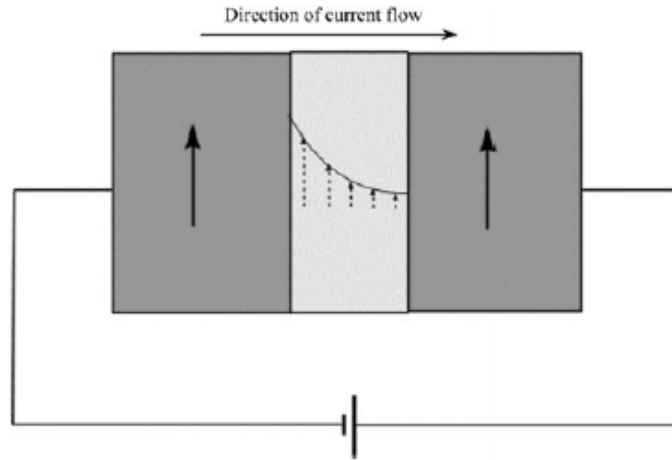
Figure 2.8: Schematic of a simple two-terminal GMR device. When a driving voltage is applied, a spin-polarized current is injected from the "injector" ferromagnet on the left into the nonmagnetic spacer. It then decays exponentially and for a sufficiently thin spacer it is detected by the "analyzer" ferromagnet on the right. Picture taken from [Gre02].

2.4.3 The Valet-Fert Model at an Abrupt Interface of Regions of Opposite Magnetizations

In this section, the main points of the model of Valet and Fert [Val93, Fer94] will be presented, which is the most widely used model for comparison with CPP GMR experiments. It takes into account spin accumulation and spin relaxation effects as the main origin of magnetoresistance in this geometry. The model is only valid at low temperatures, where electron-magnon spin-flip scattering events are negligible and the main source of spin flip is through spin-orbit interactions on defects or impurities and through exchange scattering by localized diluted magnetic moments. The following analysis will be limited to the special case of an abrupt interface between adjacent regions of opposite magnetization, because it is a good approximation for a sharp domain wall as described in the experimental part of this work. The analysis closely follows the description given in section III of [Val93].

The interface between the magnetizations is assumed to have zero resistance. A current density j flows along the z axis of the device, from one ferromagnet into the other one (see Fig. 2.9a). The two magnets are assumed to be semi-infinite single domains with a common interface at $z = 0$. For both layers, parabolic bands, identical effective masses m^* and identical Fermi velocities v_F are assumed. The magnets are assumed to be magnetized along the x-direction and the notation $\pm$ is for the absolute spin direction ($s_x = \pm\frac{1}{2}$). In the following, the indices $\uparrow, \downarrow$ signify properties belonging to the majority and minority spin directions respectively (parallel and antiparallel spin with respect to the local magnetization).

The starting point of Valets and Ferts model is a microscopic calculation of the transport properties of a system by means of the linearized Boltzmann equation. The Boltzmann transport equation incorporates both spin conserving and spin flip transition probabilities. The distribution function is modelled as the Fermi-Dirac function plus small first order perturbations to
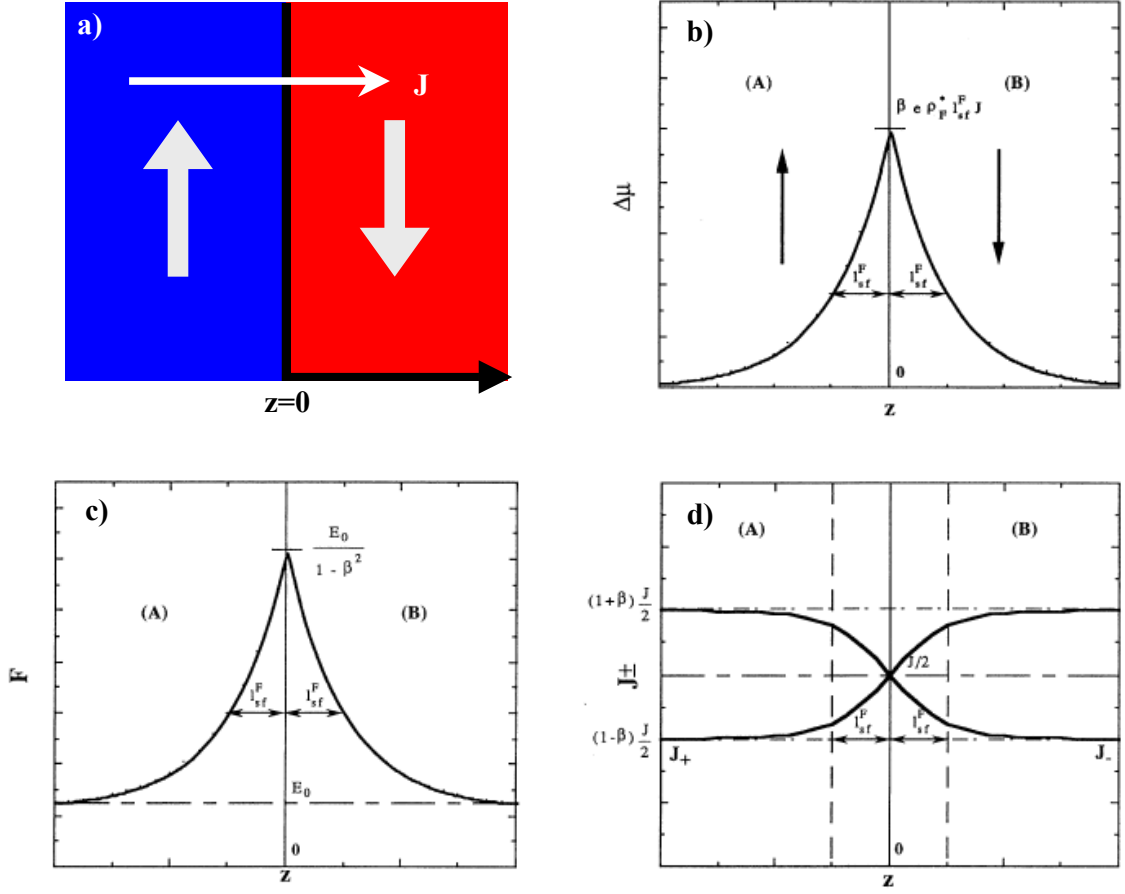
Figure 2.9: a) Schematic of two semi-infinite single domains of opposite magnetizations with an abrupt interface at $z = 0$. A current density **J** flows along the z direction. b) Spatial variation of the chemical potential at the interface due to spin accumulation effects. c) Variation of the electric field at the interface due to spin accumulation. d) Current densities J_+, J_- of charge carriers with spin pointing along the positive and negative x-directions. Figures b) to d) are taken from [Val93].

account for variations of the chemical potential due to spin accumulation effects. Because of the symmetry of the CPP transport geometry, the solution of the problem is thus developed using Legendre polynomials. One important result of this calculation is that regardless of the layer dimensions, macroscopic transport equations are recovered whenever $\lambda_s/l_{sf} \ll 1$. This means, that whenever the spin-flip length l_{sf} is much larger than the ballistic mean free path λ_s, the microscopic corrections are small. The current densities are then related to the electrochemical potential involving macroscopic transport equations. These equations are given as

$$\frac{e}{\sigma_s}\frac{\partial J_s}{\partial z} = \frac{\mu_s - \mu_{-s}}{l_s^2}, \tag{2.43}$$

$$J_s = \frac{\sigma_s}{e}\frac{\partial \mu_s}{\partial z}, \tag{2.44}$$

where J_s is the current density for spin s, $\sigma_s = n_e 2\tau_s/m$ is the conductivity for the spin s channel, l_{sf} is the spin diffusion length for spin s and $\mu_s = \mu \pm \Delta\mu$ is the spin-dependent chemical potential for spin s, with $\Delta\mu$ the term related to spin accumulation. Equation 2.44 is just Ohm's law and Equ. 2.43 expresses the fact that in the steady state the spin accumulation buildup by current divergence is balanced by equally strong spin-flip processes. These equations lead to a diffusion-type equation for $\Delta\mu = (\mu_+ - \mu_-)/2$,

$$\frac{\partial^2 \Delta\mu}{\partial z^2} = \frac{\Delta\mu}{l_{sf}^2}, \tag{2.45}$$

where $(1/l_{sf})^2 = (1/l_\uparrow)^2 + (1/l_\downarrow)^2$ is the appropriate "averaged" spin-diffusion length. It also leads to

$$\frac{\partial}{\partial z}(J_\uparrow + J_\downarrow) = \frac{\partial^2}{\partial z^2}\frac{1}{e}(\sigma_\uparrow \mu_\uparrow + \sigma_\downarrow \mu_\downarrow) = 0. \tag{2.46}$$

The last equation is just the statement that the total charge current is continuous throughout the sample. The formal general solutions to equations 2.45 and 2.46 are

$$\Delta\mu = A\,exp(z/l_{sf}) + B\,exp(-z/l_{sf}), \tag{2.47}$$

$$\sigma_\uparrow \mu_\uparrow + \sigma_\downarrow \mu_\downarrow = C\,z + D. \tag{2.48}$$

Since the spin channels contribute in parallel to the conductivity of the layer, their resistivities $\rho_\uparrow, \rho_\downarrow$ can be written in terms of a spin polarization parameter β as

$$\rho_\uparrow = \frac{2\rho_0}{1+\beta} \text{ and } \rho_\downarrow = \frac{2\rho_0}{1-\beta}, \tag{2.49}$$

where ρ_0 is the layer resistivity and β is expressed using the conductivities of the spin channels as

$$\beta = \frac{\sigma_\uparrow - \sigma_\downarrow}{\sigma_\uparrow + \sigma_\downarrow}. \tag{2.50}$$

In this simplest of models which is shown schematically in Fig. 2.9a, the spin relaxation at the interface and the interface resistance are assumed to be zero. This means that there is only spin scattering in the bulk. The boundary conditions at the interface of the two ferromagnets for solving equations 2.45 and 2.46 are that the up and down spin current densities and chemical potentials are continuous across the interface. With this and the solutions given by equations 2.47 and 2.48 in mind, the overall variation of chemical potential, electric field and spin currents across the interface, shown in Fig. 2.9b to d, becomes clear. In these figures, the arrows stand for the majority spin directions. The current flows from left to right and the interface is located at z=0. When a spin up electron attempts to cross the interface, it experiences an exponentially increasing extra chemical potential barrier and electric field $F(z)$ due to the spin accumulation. Correspondingly, the variation of the charge current carried by spin s is also governed by an exponential function. The exact solutions as derived and given in [Val93] are

$$\Delta\mu(z) = \frac{\beta}{1-\beta^2}eE_0 l_{sf}\,exp\left(\frac{z}{l_{sf}}\right), \tag{2.51}$$

$$F(z) = E_0 \left[1 + \frac{\beta^2}{1 - \beta^2} \, exp \left(\frac{z}{l_{sf}} \right) \right], \tag{2.52}$$

$$J_+(z) = (1 - \beta) \frac{J}{2} \left[1 + \frac{\beta}{1 - \beta} \, exp \left(\frac{z}{l_{sf}} \right) \right], \tag{2.53}$$

$$J_-(z) = (1 + \beta) \frac{J}{2} \left[1 - \frac{\beta}{1 + \beta} \, exp \left(\frac{z}{l_{sf}} \right) \right], \tag{2.54}$$

where E_0 is the electric field far away from the interface. Equation 2.52 contains the important result that the case of antiparallel magnetizations introduces an additional voltage drop due to spin accumulation, as compared to the parallel case. This voltage drop equals

$$\Delta V_{ap} = \int_{-\infty}^{+\infty} [F(z) - E_0] dz = 2\beta^2 \rho_0 l_{sf} J. \tag{2.55}$$

A simple conversion shows that this is equivalent to the magnetization reversal introducing an additional resistance Δr_{AP} per unit area with magnitude

$$\Delta r_{AP} = 2\beta^2 \rho_0 l_{sf}. \tag{2.56}$$

The physical interpretation is that the spin accumulation effect which extends over a length scale of l_{sf} on both sides of the interface increases the electric field, thus adding an additional interface resistance. This is the GMR effect in our pedagogically simple case, however there is also an analogy with the resistance of a sharp domain wall located at the position of the interface.

2.5 The Tunnelling Magnetoresistance Effect

When a biasing voltage is applied between two conductors that are separated by a thin insulating barrier, an electrical current can flow because of the quantum-mechanical phenomenon of tunnelling.

Elastic Tunnelling, General Case

Consider the simple case sketched in Fig. 2.10, a one-dimensional model in which two non-magnetic conductors are separated by a rectangular tunnel barrier.

Only elastic tunnelling events are considered. When a voltage V is applied to this system, then the currents flowing from left to right and from right to left across the barrier are given by

$$\begin{aligned} I_{l \to r}(V) &= C \cdot \int_{-\infty}^{+\infty} N_l(E) f(E) \cdot T(E) \cdot N_r(E - eV)(1 - f(E - eV)) dE, \\ I_{r \to l}(V) &= C \cdot \int_{-\infty}^{+\infty} N_l(E)(1 - f(E)) \cdot T(E) \cdot N_r(E - eV) f(E - eV) dE, \end{aligned} \tag{2.57}$$

where C is a constant, f is the Fermi-Dirac distribution and N is the density of states of the materials left and right of the tunnel barrier. The tunnelling probability T depends on the exact height and shape of the tunnelling barrier. The net tunnelling current flowing across the barrier is simply the difference between these currents, i.e.

$$I \equiv I_{l \to r} - I_{r \to l} = C \cdot \int_{-\infty}^{+\infty} T(E) \cdot N_l(E) N_r(E - eV) \cdot (f(E) - f(E - eV)) dE. \tag{2.58}$$

The last expression is true for a general shape of the density of states in the electrodes.
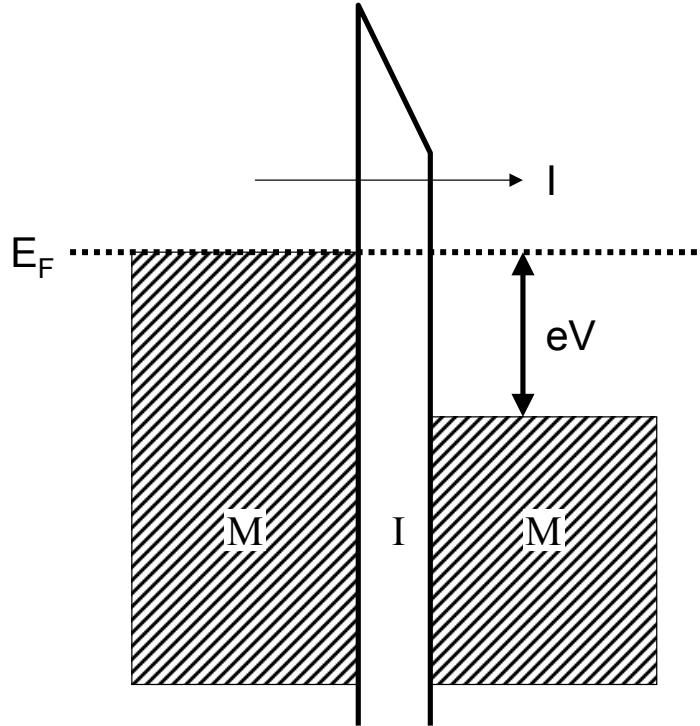
Figure 2.10: Two nonmagnetic metals separated by an insulator. When a voltage V is applied across the structure, a tunnelling current flows.

MIM Contact at Small Bias

An especially simple case arises for tunnelling between two metallic conductors that are separated by an infinitely high barrier. Then the following assumptions can be made:

- The energy dependence of the density of states in both conductors is negligible (free electron gas: $N(E) \propto \sqrt{E} \approx const.$ at $E = E_F$ and small bias).

- The tunnelling probability T is independent of energy E and applied voltage V.

This simplifies Equ. 2.58 and we get

$$I = C \cdot T \cdot N_l N_r \int_{-\infty}^{+\infty} (f(E) - f(E - eV))dE, \qquad (2.59)$$

which means that at very small biases the tunnelling current depends linearly on the applied voltage and is simply proportional to the product of the two participating density of states.

2.5.1   The Julliere Model of Tunnelling Magnetoresistance

An interesting case arises when the electrodes are exchanged with ferromagnetic metals, e.g. Fe, Co or Ni, because the density of states at the Fermi energy are not equal for spin up and spin

down electrons in these materials. Consequently, the charge currents carried by spin up and spin down electrons are asymmetric as well, as can be easily understood from equation 2.57. Two terminal electric devices containing magnetic tunnel junctions exhibit large changes in resistance as a function of the relative alignment of the magnetizations. Spin-dependent tunnelling is the
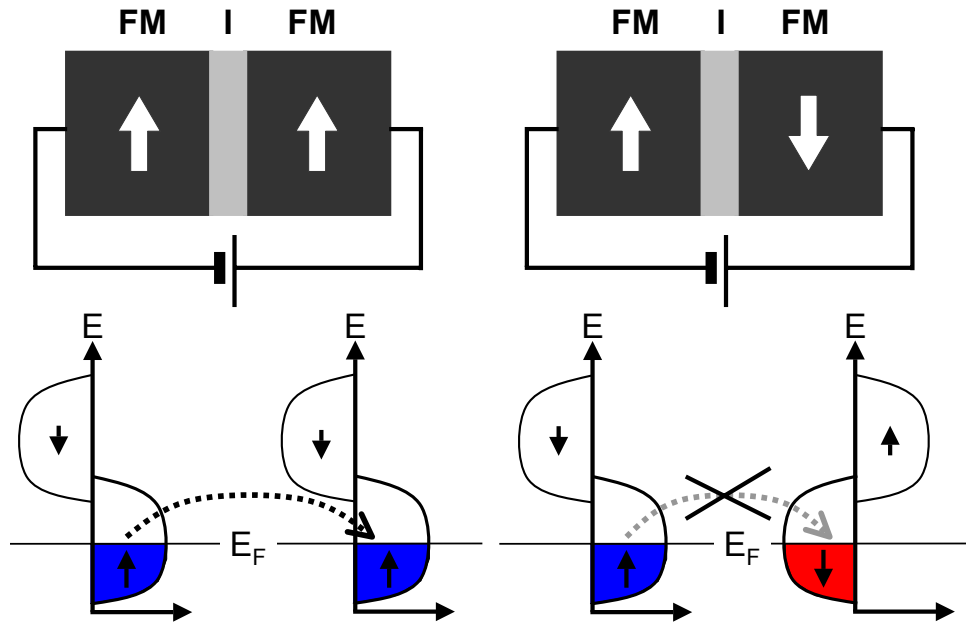
Figure 2.11: Schematic of a two-terminal TMR device. For simplicity, a half-metallic band structure and a fully spin-conserving tunnelling process is considered. Upper half: Parallel and antiparallel magnetization state. Lower half: Corresponding band alignment. In the antiparallel state, the tunnelling process is suppressed because of opposite spin directions at the Fermi energy.

basic mechanism leading to these resistance changes and it is schematically shown in Fig. 2.11. For simplicity, half-metallic electrodes and a fully spin-conserving tunnelling process are assumed. In the parallel magnetization state of the device, the tunnelling process between the two electrodes is possible. Because of the half-metallicity, the current consists entirely of spin up carriers tunnelling from filled states on one side into empty states on the other side. When one of the ferromagnets is switched, then there is a finite number of filled states for spin up on one side but there are no empty spin up states in the other material. Then the product of initial and final states and thus the tunnelling current is zero. Consequently, the sample resistance is highest in the antiparallel magnetization state and lowest in the parallel magnetization state.

In 1975, in a pioneering work, M. Julliere studied the conductance properties of Fe/Ge/Co tunnel junctions [Jul75]. He found that the conductance of his trilayer structure exhibited large changes in resistance depending on the relative alignment of the magnetizations of Fe and Co. He developed a simple quantitative model for the magnetoresistance that is based on the spin splitting of the two electrodes at the Fermi edge and the simple picture of the total tunnelling

conductance given above.

In the ferromagnetic electrodes the fractions of majority spin electrons a_i and of minority spin electrons $(1 - a_i)$ in electrode i are given by

$$
\begin{aligned}
a_i &\equiv \frac{N_{i\uparrow}}{N_{i\uparrow} + N_{i\uparrow}} = \frac{1 + P_i}{2}, \\
(1 - a_i) &= \frac{N_{i\downarrow}}{N_{i\uparrow} + N_{i\uparrow}} = \frac{1 - P_i}{2},
\end{aligned}
\tag{2.60}
$$

with N_{is} the spin-dependent density of states at the Fermi energy and

$$
P_i = \frac{N_{i\uparrow} - N_{i\downarrow}}{N_{i\uparrow} + N_{i\downarrow}},
\tag{2.61}
$$

the spin polarization of the ferromagnet. We assume that the tunnelling current is given by Equ. 2.59, i.e. it is proportional to the product of the density of states at the Fermi energy of the two electrodes. Furthermore, the tunnelling process is fully spin conserving and thus the two spin channels contribute in parallel to the total conductivity G. Thus in the parallel magnetization configuration we have

$$
G_P \propto N_{1,\uparrow} \cdot N_{2,\uparrow} + N_{1,\downarrow} \cdot N_{2,\downarrow} \propto a_1 a_2 + (1 - a_1)(1 - a_2) = (1 + P_1 P_2)/2,
\tag{2.62}
$$

whereas for antiparallel magnetizations

$$
G_{AP} \propto N_{1,\uparrow} \cdot N_{2,\downarrow} + N_{1,\downarrow} \cdot N_{2,\uparrow} \propto a_1(1 - a_2) + (1 - a_1)a_2 = (1 - P_1 P_2)/2.
\tag{2.63}
$$

The resulting magnetoresistance ratio is now a matter of definition. Julliere considered relative changes in the tunnelling conductance, the so-called junction magnetoresistance

$$
JMR \equiv \frac{G_P - G_{AP}}{G_P} = \frac{2P_1 P_2}{1 + P_1 P_2},
\tag{2.64}
$$

thus arriving at the simple result that differences between the two different states are given by the spin polarizations of the electrodes alone. However, in literature it is perhaps more common to quote the tunnel magnetoresistance

$$
TMR \equiv \frac{R_{AP} - R_P}{R_P} = \frac{2P_1 P_2}{1 - P_1 P_2}.
\tag{2.65}
$$

The above simple model treats the two electrodes as independent electronic systems and the barrier shape is assumed to be unchanged in the range of the experimentally applied bias. As a consequence it does not correctly predict the dependence of TMR on the barrier material and height, on temperature and bias that is present real systems. Nevertheless it is the best known model of TMR and it gives an intuitive insight into the main physical origin of the effect.

Chapter 3

(Ga,Mn)As Material Properties

The group of nonmagnetic III-V semiconductors and especially GaAs is widely used in a multitude of microelectronics devices. High carrier mobility and a direct band gap have lead to applications in high frequency devices and in the field of optoelectronics. By introducing magnetic Mn ions into GaAs, the semiconductor can be made paramagnetic and, for sufficiently high concentrations, also ferromagnetic. Since its discovery in 1989, (Ga,Mn)As has become the most widely used and most well-understood ferromagnetic semiconductor [Mun89, Ohn96]. It is the base material for all devices presented in this work. In the following, the most important material properties will be presented by highlighting both key experimental and theoretical breakthroughs.

3.1   Growth

Thin films of (Ga,Mn)As are most commonly grown using molecular beam epitaxy (MBE). Early attempts have shown that under equilibrium growth conditions the solubility of Mn in III-V semiconductor lattices is below 0.1 %. This is too low for the incorporated Mn to significantly change the magnetic character of the compound semiconductor. It was found in 1989 by Munekata et al. that low-temperature molecular beam epitaxy (LT-MBE) allows one to dope InAs and GaAs with the magnetic element Mn over its solubility limit, making it possible to realize an alloy of III-Vs and magnetic elements [Mun89]. This special growth technique involves keeping the substrate temperature between 150 and 350 °C. Under these conditions, Mn concentrations in excess of 5% can be obtained (see Fig. 3.1).

The most important parameters that influence the material properties of low temperature grown (Ga,Mn)As are substrate temperature T_s, III/V equivalent beam pressure ratio and the temperature of the Mn elementary source. The transport experiments presented in this thesis require (Ga,Mn)As thin films with metallic transport behavior, high Curie temperature ($\approx$60 K) at a doping density of a few percent Mn and the absence of unwanted inhomogeneities due to segregation of Mn or Mn compounds. As can be seen from the schematic growth phase diagram in Fig. 3.1, there is a well defined growth window with respect to T_s and x, where metallic high quality (Ga,Mn)As can be grown. An attempted growth that is too far outside this window can result in insulating (Ga,Mn)As layers with low Curie temperature or no ferromagnetism at all, or layers exhibiting bad crystalline quality or MnAs related precipitates. Over the past
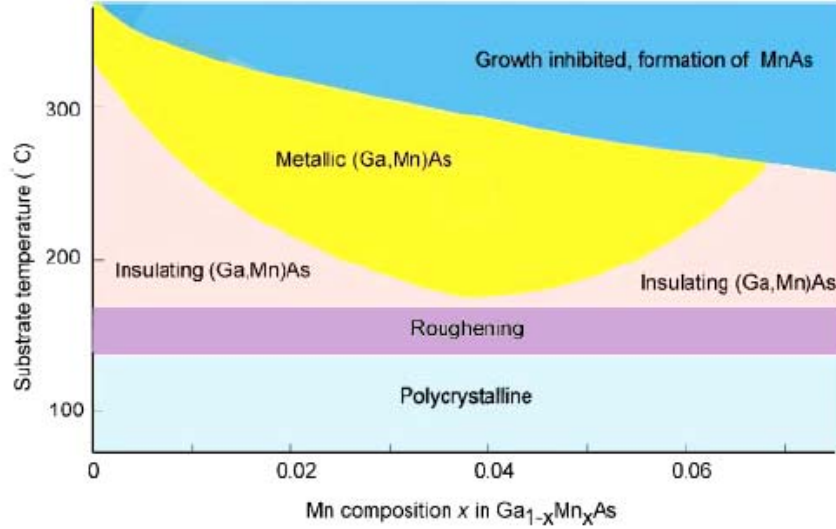
Figure 3.1: Schematic growth phase diagram relating the growth parameters (substrate temperature T_s and Mn content) with the characteristics of the resulting (Ga,Mn)As thin film. Diagram taken from [Ohn98].

years, much effort has been put into optimizing (Ga,Mn)As properties by understanding the details of its growth. This has resulted in improved Curie temperatures for as-grown thin films ($T_C \approx 70$ K, x=6%, see section 6.2.1) as well as for thermally annealed layers (T_C=140 K, x=6%, see [Edm02]) that can be routinely obtained. For further details about the growth of (Ga,Mn)As thin films refer to [Sch04, She97, Cam03], for example.

3.2 The Mn Impurity in GaAs

The (Ga,Mn)As crystal structure is zinc blende. When Mn is incorporated into the zinc blende lattice, its most common and stable position is the Ga site. On this substitutional site, it contributes its $4s^2$ electrons to the $s - p^3$ bondings with the nearest As atoms. The electronic configurations of the isolated Ga,As and Mn atoms are

$$
\begin{aligned}
Ga: & \quad [Ar]3d^{10} \quad 4s^2 \quad 4p^1 \\
Mn: & \quad [Ar]3d^5 \quad 4s^2 \\
As: & \quad [Ar]3d^{10} \quad 4s^2 \quad 4p^3.
\end{aligned}
\tag{3.1}
$$

From these electronic valence configurations one can see that Mn has one electron less than Ga available for bonding, and therefore, each Mn on a substitutional site can donate one hole to the Γ^8 valence band.

The electronic structure of the Mn acceptor has been extensively investigated by various techniques including fourier transform infrared spectroscopy, Hall measurements, photoluminescence, absorption and space-charge techniques (refer to [Lin97] and the references therein). Its energetic position is about 113 meV above the top of the valence band.

In III-V compounds, there are essentially three possible types of Mn centers [Szc99b]. The first one is formed by substitutional manganese Mn^{3+}, which is in d^4 configuration, with the ground state spin $S = 2$ (center C1). The second type of Mn center occurs when the center C1 traps an electron and binds it tightly at the d shell (center C2). This is equivalent to a d^5 configuration, with $S = 5/2$. The Mn center C2 is negatively charged and can therefore attract and weakly bind a hole, forming a (d^5+h) complex center C3.

Of these three different possibilities, only C2 and C3 fit to the vast majority of experimental observations for (Ga,Mn)As. Moreover, the neutral center C3 is only observed in a narrow range of the Mn content x. The reason for this is that for very small x, the material tends to be self-compensated and that starting at several fractions of a percent and higher, (Ga,Mn)As shows p-type and metallic conductivity.

In summary, the effect of the Mn doping in GaAs is to provide hole carriers with an angular momentum of $j = 3/2$ as well as localized magnetic moments with $S = 5/2$ to the material. Both of these aspects are vital ingredients to the carrier-induced ferromagnetism described in detail in the following section.

3.3   Hole-Mediated Ferromagnetism in (Ga,Mn)As

The most widely used theoretical approach to ferromagnetism in zinc-blende magnetic semiconductors in general and particularly (Ga,Mn)As is the Zener model description of carrier-mediated ferromagnetism. This model was originally proposed by T. Dietl in 2000 [Die00] and subsequently developed more thoroughly in [Die01b]. In parallel with the latter work, a similar but independent and equally important study by A.H. MacDonald et al. was presented [Abo01]. In both works, the exchange coupling between the itinerant holes inside the (Ga,Mn)As sp^3 valence band and the localized magnetic moments of the Mn 3d valence states is treated using in the mean field approximation.

Before turning to a more detailed description it is useful to highlight the basic physical mechanism leading to ferromagnetism in (Ga,Mn)As. As pointed out above, the substitutional Mn impurities in GaAs are incorporated in a Mn^{2+} valence configuration which leads to localized magnetic moments of spin S=5/2, according to Hund's rules. The direct exchange mechanism between these localized moments is antiferromagnetic but because of the high dilution of Mn impurities it is rather weak. Without the presence of a sufficiently large number of holes (for example in electrically compensated samples) there is little or no magnetic ordering. However, since the Mn impurity acts as a shallow acceptor, each Mn ideally provides one hole to the valence band. The magnetic interaction between the Mn and the valence band holes is antiferromagnetic as well. However, the valence band holes are not strongly localized on a single impurity but tend to be spread out over many lattice sites. Thus they interact with a large number of Mn ions. This tends to align all Mn magnetic moments inside the range of the hole spin antiparallel with respect to the hole spin and thus parallel with each other, creating islands of ferromagnetic ordering. For increasing hole concentrations these islands increasingly overlap and above a threshold Mn concentration of ≈0.5% long range ferromagnetic order is observed.

Carrier States

Virtually all properties of ferromagnetism in (Ga,Mn)As are strongly affected by the fact that hole carriers mediate the net ferromagnetic interaction between the localized Mn moments. Hence it is vital to include a realistic picture of the valence band states of (Ga,Mn)As into the modelling. In order to derive the role of the carriers in ferromagnetism of (Ga,Mn)As, both the calculations in [Die01b] as well as in [Abo01] are based on an effective mass Hamiltonian

$$H = H_{KL} + H_{pd} + H_s, \tag{3.2}$$

with three main contributions. The influence of the GaAs host lattice is modelled by employing the 6×6 Kohn-Luttinger Hamiltonian H_{KL} which captures the effects of the spin-orbit interaction of the hole carriers ($j = 3/2$ and $1/2$). The phenomenological Luttinger parameters (γ_1, γ_2, γ_3)=(6.85,2.1,2.9) and spin-orbit splitting Δ_{so}=0.34 eV are adopted with their standard values[1].

The GaAs host valence bands are modified by the substitutional Mn impurities which introduce localized d-electrons that hybridize with the p-like hole states. This hybridization is accounted for in the term H_{pd}, which contains an effective exchange coupling J_{pd} between the itinerant hole and localized Mn moments. In the virtual crystal and mean field approximations,

$$H_{pd} = -J_{pd}N_{Mn}m_I\hat{M} \cdot \mathbf{s}, \tag{3.3}$$

where J_{pd} is the exchange coupling constant, N_{Mn} is the Mn concentration, $\mathbf{s}$ is the hole spin and m_I is the mean azimuthal quantum number in the direction of the local-moment orientation $\hat{M}$, averaged over all local moments. The virtual crystal approximation assumes an equally spaced distribution of Mn impurities in the GaAs lattice and the mean field theory replaces local variations in the orientation of the Mn spins by an average, homogeneous magnetic field.

The term H_s in Equ. 3.2 accounts for the existence of strain in the crystal, e.g. due to lattice mismatch with the underlying substrate and buffer layers. The inclusion of strain is of utmost importance for the comparability with experiments, where it often determines the net magnetic anisotropy of a (Ga,Mn)As thin film.

Curie Temperature

One of the main achievements of the mean field theory of carrier-mediated ferromagnetism (Ga,Mn)As is the modelling of the ferromagnetic transition temperature. One possible formal path to derive the (Ga,Mn)As mean field Curie temperature is given in [Abo01] and sketched in the following. The starting point is to formulate the p-d interaction term by introducing a mean magnetic field of magnitude $h_{MF} = J_{pd}N_{Mn}m_I$ acting on the carriers. With this, one can write down the mean-field free energy

$$F_{MF}(m_I) = F_b(\vec{h_{MF}} = J_{pd}N_{Mn}m_I\hat{M}) - k_BTN_Is(m_I) \tag{3.4}$$

of the Mn plus hole system. Here, $N_{Mn} = N_I/V$ is the density of Mn impurities, s(M) the entropy per impurity, F_b is the free energy of a system of noninteracting fermions with the

---

[1]The matrix representations of all terms of the Hamiltonian are given in detail in the appendices of [Die01b] and [Abo01]. Although slightly different nomenclatures are used, both these works share the same fundamental approach to carrier mediated ferromagnetism in (Ga,Mn)As.

single-particle Hamiltonian $H_{pd} - h_{MF}\hat{M} \cdot \vec{m}_I$. Note that the above formula applies only in the absence of external magnetic fields or, in other words, describes the spontaneous magnetization. To find the ground state of the system it is necessary to minimize the free energy, i.e. to look for solutions of $dF/dm_I = 0$. This yields

$$\frac{ds(m_I)}{dm_I} = \frac{J_{pd}}{k_B T V} \frac{dF_b(h_{MF}\hat{M})}{dh_{MF}}. \tag{3.5}$$

The response of the localized spins to the exchange field coming from the valence band holes is treated by considering an auxiliary system that is well known. It consists of a number of isolated magnetic impurities coupled only to an external magnetic field H. This problem is solved in section 2.1.3, with the result that the magnetization follows

$$M(H) = JB_J(x), \tag{3.6}$$

where $B_J(x)$ is the Brillouin function given by Equ. 2.14 and $x = g\mu_B HJ/(k_B T)$. In the ground state

$$\frac{ds(m_I)}{dm_I} = -g\mu_B H/(k_B T). \tag{3.7}$$

From a comparison of Equs. 3.5 and 3.7 it follows that F_{MF} is minimized by

$$M = JB_J(g\mu_B H_{eff}/(k_B T) = JB_J(x_{eff}), \tag{3.8}$$

where

$$x_{eff} \equiv \frac{g\mu_B H_{eff}}{k_B T} = -\frac{J_{pd}}{k_B T V} \frac{dF_b(h_{MF}\hat{M})}{dh_{MF}}. \tag{3.9}$$

It follows that the effective Zeeman magnetic field $h_{MF} = N_{Mn}J_{pd}m_I$ is determined by solving the self-consistent equation

$$h_{MF} = N_{Mn}J_{pd}JB_J[x_{eff}(h_{MF})] \tag{3.10}$$

numerically. The calculations can be simplified when the experimental temperatures are considerably smaller than the itinerant carrier Fermi energy, which is often the case in experiment. Then, it is allowed to replace the free energy $F_b(\vec{h}_{MF})$ of the carriers by their ground state energy $E_b(\vec{h}_{MF})$. The ground state energy is calculated by solving the eigenvalue problem of the $H_{pd} - h_{MF}\hat{M} \cdot \vec{m}$ and integrating over the Fermi sphere. A single numerical calculation of $E_b(\vec{h}_{MF})$ over the range from $h = 0$ to $h = \frac{5}{2}N_{Mn}J_{pd}$ may be used to determine the local moment magnetization M(T) and mean field free energy at all temperatures. By linearizing the self-consistent equation at small h_{MF}, the mean-field theory critical temperature T_c is found to be

$$k_B T_c = -\frac{J(J+1)}{3} \frac{N_{Mn}J_{pd}^2}{V} \frac{d^2 F_b(h_{MF}\hat{M})}{dh_{MF}^2} \tag{3.11}$$

at $h_{MF} = 0$. According to [Abo01], the second derivative is proportional to $p^{1/3}$ at small p. Hence

$$T_c = CN_{Mn}p^{1/3}, \tag{3.12}$$

with a material constant C. The last expression states that in order to maximize the Curie temperature one has to maximize the Mn doping concentration as well as the carrier concentration.

Magnetic Anisotropy

A calculation of the ground state energy E_b for fixed parameter sets (p, T, h_{MF}) and various directions of the magnetization enables the authors in [Abo01] to predict the orientation of easy axes in (Ga,Mn)As in good qualitative agreement with experiment. The experimentally most relevant parameter for the magnetic anisotropy is the strain of the thin film that originates from a lattice mismatch with the underlying substrate and buffer layers. The mechanism by which strain influences the magnetic anisotropy is that it causes a shift of heavy and light hole energies relative to each other. This causes a shift in the relative importance of heavy and light hole bands whose Fermi surfaces exhibit quite different anisotropies.
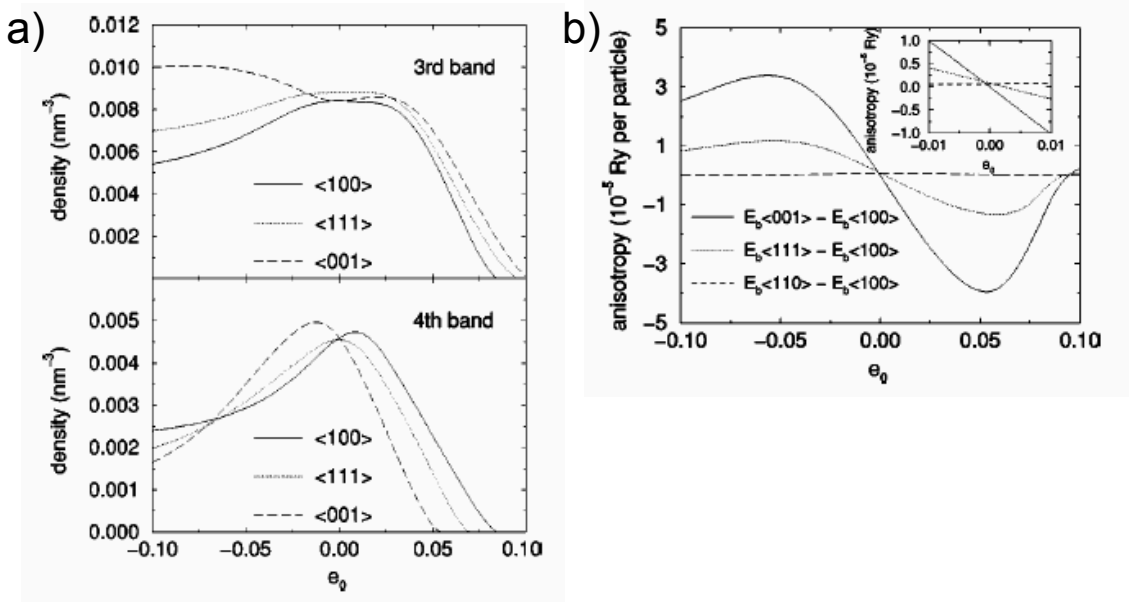
Figure 3.2: a) Third and fourth-band densities for [100], [111], and [001] magnetization orientations versus in-plane strain at h=0.01 Rydberg and $3.5 \cdot 10^{20}$ cm^{-3}. Curves for the [110] magnetization orientation are not shown here since they are similar to those for the [100] orientation. b) Energy differences among [001], [100], [110], and [111] magnetization orientations versus in-plane strain at h=0.01 Rydberg and $3.5 \cdot 10^{20}$ cm^{-3}. For compressive strains the system has a easy magnetic plane perpendicular to the growth direction. For tensile strains the anisotropy is easy with the preferred magnetization orientation along the growth direction. The anisotropy changes sign at large tensile strain. Pictures taken from [Abo01].

The repopulation among bands is demonstrated in Fig. 3.2, which is taken from [Abo01]. The calculations were carried out for a hole density of $3.5 \cdot 10^{20}$ cm^{-3} and a mean field theory exchange field of $h_{MF} = 0.01$ Rydberg that corresponds to a Mn doping level of 5%. The lattice mismatch with respect to the substrate is defined as

$$e_0 = \frac{a_S - a_F}{a_S} \tag{3.13}$$

Here, a_S and a_F are the lattice constants of substrate and thin film, respectively. Hence $e_0 < 0$

corresponds to compressive strain found in (Ga,Mn)As on (LT)-GaAs and $e_0 > 0$ corresponds to (Ga,Mn)As grown on a (In,Ga)As buffer, for example. Figure 3.2a demonstrates the behavior of the hole band occupation density that is a complex function of both the sign and magnitude of the strain as well as the orientation of the magnetization. The growth direction is defined as the [001] crystal direction. Hole densities vary dramatically as a function of strain and orientation of the magnetization.

Figure 3.2b shows calculated energy differences that occur when the magnetization points along [001], [111] and [110] as compared to the [100] direction. Note that there is an in-plane biaxial symmetry between [100] and [010]. According to these calculations, for compressive strains ($e_0 < 0$) the system has in-plane magnetic anisotropy with preferred directions along [100] and [110]. For tensile strain the anisotropy is easy along the growth direction, except for the highest strains, where there is a change in sign of the anisotropy. Mean field theory predictions concerning the magnetic anisotropy are consistent with a large number of experiments. Compressive strain induced by (Ga,Mn)As growth in a (In,Ga)As buffer is a frequently used tool to create perpendicular magnetic anisotropy [Yam04] and mean field theory is even able to explain reorientations of the easy axis in compressively strained (Ga,Mn)As that occur as a function of temperature [Saw04].

3.4   Mn Interstitials in (Ga,Mn)As and Effect of Annealing

In low temperature grown (Ga,Mn)As the Mn atoms can occupy three types of lattice sites [Yu02]. Substitutional Mn occupies the Ga lattice sites and thus forms the (Ga,Mn)As random alloy. Furthermore, the Mn atoms can occupy interstitial sites and finally, it can precipitate out to form different phases (e.g. MnAs inclusions). The latter process can be quite efficiently prevented through optimization of the growth parameters.

The Mn interstitial point defects however, cannot be prevented in that way. Even in the highest quality layers grown nowadays, these defects can amount to as much as a few tens of percent of the total Mn concentration. As all interstitials of metal atoms, Mn interstitials act as donors and thus passivate substitutional Mn atoms. Furthermore, since the direct exchange interaction between Mn atoms is antiferromagnetic [Abo01], interstitial Mn can effectively diminish the number of ferromagnetically ordered Mn [Yu02]. Both of these effects are detrimental to the Curie temperature of the material which is determined by the mean field expression $T_C \propto xp^{1/3}$, as derived in the previous section.

The presence of Mn interstitials is believed to be the main reason why as grown layers regularly exhibit much lower (by more than a factor of two) critical temperatures as can be expected from the nominal Mn concentration and simply using formula 3.12. However, evidence is presented in [Yu02] in the form of channeling Rutherford backscattering experiments that Mn interstitials can be removed by thermal annealing at temperatures that are on the order of the substrate temperature during growth of the (Ga,Mn)As layer. Consistent with the above statements, the reduction of Mn interstitials is shown to result in an increased hole density, conductivity and critical temperature of the layers.

Excellent results are obtained by low temperature annealing in air over periods of many days [Edm02]. The annealing temperature is kept at $\approx 180°C$, which is considerably below the substrate temperature during growth (≈ 250 °C), whereas temperatures much higher than

T_s are known to create Mn related precipitates. The mechanism responsible for the reduction of interstitials is identified in [Edm04] as the outdiffusion of Mn atoms along interstitial paths towards the surface where it is believed to be passivated by air.

For the reasons presented above it becomes clear that for the usage of ferromagnetic, low temperature-grown (Ga,Mn)As in multilayers one has to keep in mind that the material is very temperature sensitive. Since the growth of many epitaxial materials involves temperatures much higher than the typical (Ga,Mn)As growth temperature, the respective materials have to be grown before the first (Ga,Mn)As layer. Otherwise unwanted precipitates can form or at least the electrical and magnetic properties of the (Ga,Mn)As will be considerably and perhaps irreproducibly altered.

Note that all (Ga,Mn)As based transport samples presented in this thesis were measured in an as grown state. This procedure has ensured a high reproducibility of (Ga,Mn)As material characteristics from wafer to wafer. Another reason why annealed samples were not considered for transport is that the surface layer of passivated Mn that is present in these samples presents difficulties during the fabrication of electrical contacts.

Chapter 4

Experimental Setup

4.1 Electrical Measurement Setup

For the purpose of electrical measurements, all devices are mounted inside chip carriers offering a maximum of 18 electrical contacts to an external measurement circuit. The sample itself is electrically connected to the chip carrier using gold wires attached with an ultrasonic wire bonder. In Fig. 4.1a arrows indicate the chip carrier. The figure also indicates how the chip carrier is mounted inside a socket at the end of a sample stick. Wires run inside the sample stick and an electrical measurement circuit can be connected to the sample by means of standard coaxial cabling.
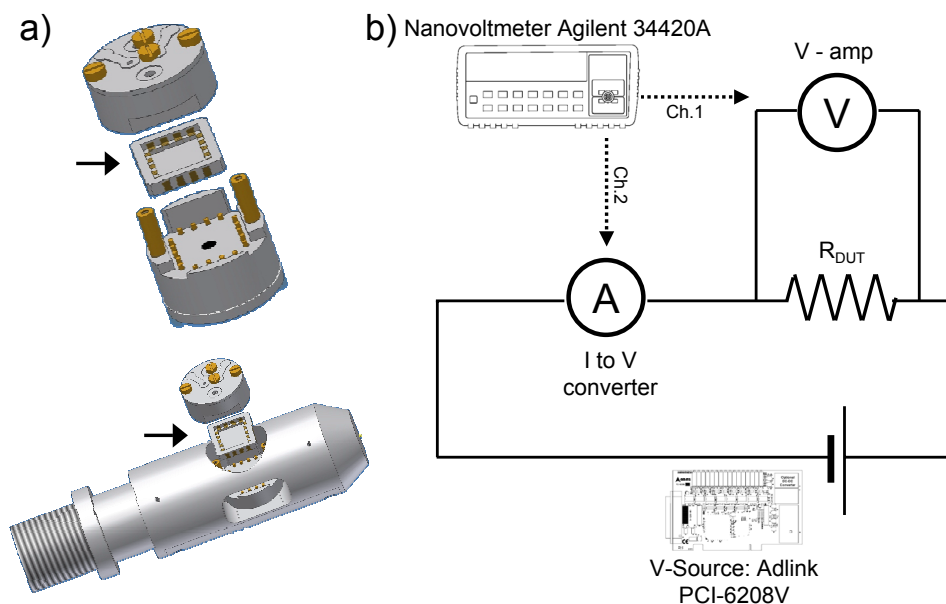

Figure 4.1: a) The arrows indicate the 18 contact electrical chip carrier along with its mounting scheme on the electrical sample stick. The chip carrier contains the device under test during electrical measurements. b) Schematic diagram of the measurement circuit being used for DC electrical measurements.

A schematic of the electrical circuit that was being used for all electrical measurements presented in chapters 5 to 7 is given in Fig. 4.1b. Electrical measurements were performed using DC excitation voltages only. An eight-channel computer-controlled analog output card model Adlink PCI-6208V serves as variable DC voltage source. The D/A card has a maximum output range of ± 10 V, the voltage output is adjustable with 16 bit resolution. The voltage output of the card has an offset of ≈ 5 mV which is constant over the whole output range. In order to decrease both the offset voltage as well as the minimum possible excitation voltage step size, a 1000:1 voltage divider was used most of the time. The voltage divider consists of two metal-oxide resistors (100 kΩ and 100 Ω) connected in series. The sample is connected in parallel with the 100 Ω resistor. Due to the sample impedances being considerably higher compared to the voltage divider output resistance, all measurements were thus performed in constant voltage mode. The current through the sample was measured using a custom-built zero input-impedance current to voltage converter circuit whose proportional output was connected to one measurement channel of a nanovoltmeter model Agilent 34420A. The voltage drop over the device resistance under test R_{DUT} was measured using a custom-built GΩ input-impedance voltage amplifier whose proportional output was connected to the second measurement channel of the nanovoltmeter. Control of the analog output card as well as data collection from the nanovoltmeter is fully automated using a custom National Instruments Labview program.

4.2   Magnetocryostats

Measurements on Lateral (Ga,Mn)As Nanoconstrictions

Measurements of the magnetoresistance and current-voltage characteristics of all lateral samples with nanoconstrictions were carried out in a He bath cryostat fitted with a superconducting magnet. The magnetic field was applied in the plane of the epilayer. A custom-built high precision current source was used to produce magnetic fields with a maximum of ± 0.5 T in the field center of the magnet coil, where the sample was located. Using this cryostat, measurements are only possible at a fixed temperature of 4.2 K.

Measurements on Vertical TAMR Tunnel Junctions

Transport measurements presented in chapters 6 and 7 were carried out in a He bath magnetocryostat fitted with three sets of mutually orthogonal Helmholtz coils. A schematic of the coil arrangement is shown in the left panel of Fig. 4.2. The right panel is a drawing of the actual 3D magnet system indicating the X, Y and Z field directions. The diameter of the magnet's access bore is 55 mm. Each set of Helmholtz coils is connected to a custom-built high precision current source. The current sources can be independently controlled using an analog voltage produced by one out of eight channels of an analog voltage output card model Adlink PCI-6208V. The 3D magnet system allows the application of magnetic fields **H** of up to 300 mT in any direction by superposition of the X, Y and Z fields. The cryostat is fitted with a variable temperature insert driven by a temperature controller operating on the basis of a proportional-integral-derivative (PID) feedback loop. Electrical measurements are possible over the full temperature range of 1.7 to 250 K.

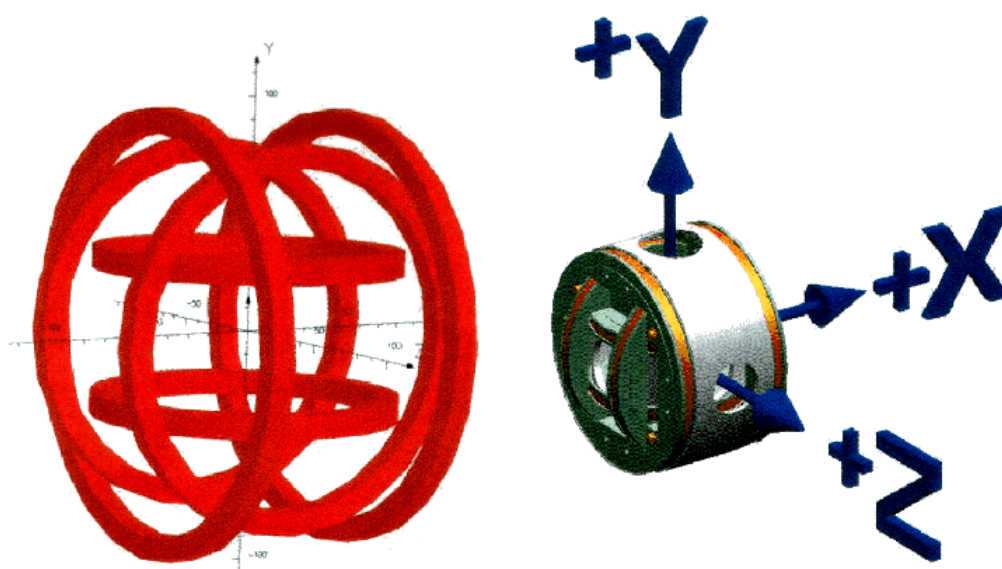Figure 4.2: Transport measurements conducted on vertical TAMR tunnel junctions were carried out in a magnetocryostat fitted with three sets of mutually orthogonal Helmholtz coils. Left panel: Schematic of the coil arrangement. Right panel: Drawing of the actual 3D magnet system indicating the direction of the independently controllable X, Y and Z field. The diameter of the access bore is 55 mm.

Chapter 5

Magnetotransport Effects in Lateral Ferromagnetic Semiconductor Junctions

5.1 Motivation

The discovery of the giant magnetoresistance effect around 1989 [Bin89] with its large scientific and commercial impact has drawn a lot of interest towards finding novel low field magnetoresistive phenomena. In the field of ferromagnetic semiconductors, as seen from a materials and application point of view, (Ga,Mn)As is the most promising candidate for magnetoresistance effects. Thus, in the past, a lot of effort has been concentrated on this material system. However, an investigated magnetoresistive effect needs to be sufficiently large compared to other (unwanted) bulk effects, if one wants to unambiguously identify the true origin of the investigated phenomenon. Unfortunately, this prerequisite is not convincingly fulfilled in all of the published results in literature.

5.2 Difficulty to Observe Sizable GMR Effects in (Ga,Mn)As

Early attempts at mimicking the GMR effect, which is well established in metals, using (Ga,Mn)As seem to indicate that despite being a high spin polarization material, (Ga,Mn)As results lag behind the metal results in terms of amplitude. For example, N. Akiba et al. have investigated the spin dependent scattering effects in corresponding (Ga,Mn)As/AlGaAs/(Ga,Mn)As trilayer structures [Aki00]. The thickness of the nonmagnetic spacer layer in these experiments was 2.8 nm and the Al content was 14% and 30%. The authors report very small CIP-GMR ratios of 0.2% and 0.04% at 30 K. These MR ratios are lower by several orders of magnitude compared to metal trilayers. One possible reason for this could be that the carriers in (Ga,Mn)As are holes with very small mean free paths. In contrast to electrons in ferromagnetic metals these holes exhibit very strong spin-orbit coupling and thus the spin diffusion length is considered to be much lower. Because of high disorder in the material, the ballistic mean free path is also rather small. As mentioned above, the mean free path and the spin diffusion length are the critical scaling parameters for CIP and CPP-GMR, respectively.

From this point of view, small GMR ratios are to be expected. Besides, extrinsic magnetoresistance contributions from AMR for example are also on the order of a few percent and can be expected to play a role in these measurements.

5.3   Domain Wall Resistivity

Another particularly promising candidate for sizable magnetoresistance effects is the electrical resistivity of a ferromagnetic domain wall (DW). A DW is an interface between regions of uniform magnetization and different magnetization directions. Domain walls are regions where the local magnetization direction rotates continuously from an initial to a final orientation.

Historically, magnetic domains and domain walls have been extensively studied theoretically. Quite naturally this work was stimulated by the phenomenology found in ferromagnetic metals. The fundamental work on the energetics and structure of domain walls dates back as early as the 1930s and it assumes a continuous distribution of magnetic moments in the ferromagnet. This has proven to be a good approximation for ferromagnetic metals and is the basis of a vast majority of conventional micromagnetic theories. However, an important question for the field of diluted magnetic semiconductors is whether the continuous medium approximation is also valid in diluted magnetic semiconductors.

The reason for this is a comparably low concentration of magnetic ions and in the case of (Ga,Mn)As, an even lower concentration of hole carriers participating in carrier mediated ferromagnetism. This fundamental question has been addressed in the literature [Die01a]. The exact details of this analysis are beyond the scope of this work, however, it should be noted that the authors conclude that the micromagnetic theory in its standard continuous medium form is suitable for modelling the domain structure in thin layers of (Ga,Mn)As with properties very similar to what was used in the course of this thesis[1]. Thus in the following, micromagnetic models and terminology will be used in their standard form, assuming that they are valid in (Ga,Mn)As as well.

The two most common types of domain walls are the Bloch wall and the Néel wall. They are schematically depicted in Figure 5.1 for the case of a $180°$ change of the magnetization direction between the neighboring domains.

In a Bloch wall, the magnetization rotates in a plane parallel to the plane of the wall. In ferromagnetic films with in-plane easy axis of magnetization, Néel walls are more favorable. Here, the magnetization rotates in a plane perpendicular to the wall.

This rotation is equivalent to an internal exchange field or an effective potential for an itinerant spin inside the wall. Historically, DW resistivity was intensively studied in ferromagnetic metals like Fe, Co, FePt [Ken01]. The observed resistance due to the contribution of a single DW is clearly below 0.1% as compared to the resistance of the sample. Additionally, there are serious complications in the measurement of such a small contribution because of the existence of AMR, anomalous Hall effect and Lorentz magnetoresistance in these magnetic materials.

However, several theoretical considerations of domain wall resistivity (DWR) predict that bigger results can be expected in high spin polarization ferromagnetic semiconductors, especially when the DW thickness is small. For completeness, some of the early models that

---

[1]The validity of standard micromagnetic theory was confirmed for $Ga_{0.957}Mn_{0.043}As$ on $Ga_{0.84}In_{0.16}As$ with $T_c = 80\ K$ and carrier concentrations of $p \geq 1 \cdot 10^{20}\ cm^{-3}$ [Die01a].
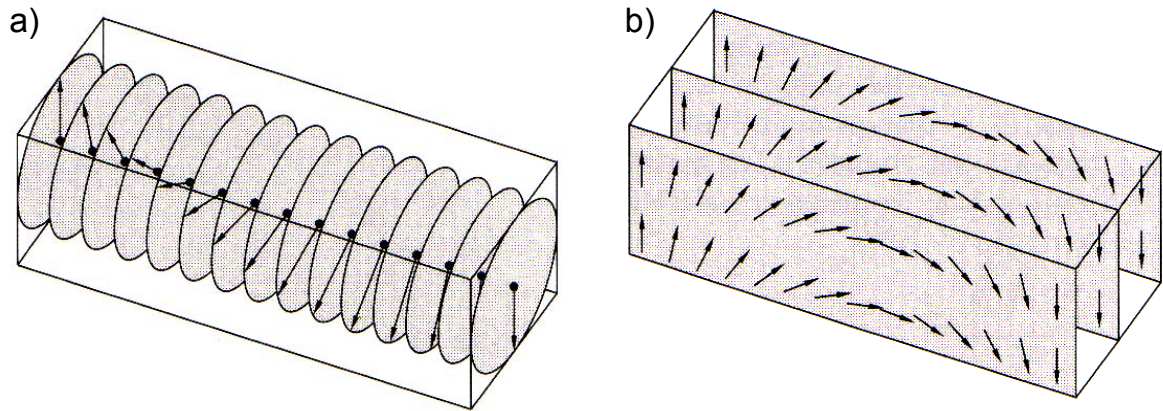
Figure 5.1: Two common types of $180°$ domain walls: a) Bloch wall, where the magnetization direction rotates in a plane perpendicular to the initial and the final state. b) Néel wall, where the magnetization rotates within the plane that encompasses initial and final state. Picture taken from [Blu01].

were developed with ferromagnetic metals in mind will be briefly highlighted in the following [Ken01]. The main mechanism for the DW resistance in these models is spin-dependent scattering in a non-uniform potential caused by the DW. A different approach is taken by Flatté and coworkers. Their unipolar spin diode model fits well to the presented experimental results and will therefore be presented in a dedicated section below.

The earliest model of scattering inside DWs was presented by Cabrera and Falicov who considered the reflection of incoming electrons on the above mentioned effective potential inside the DW [Cab74]. The reflection probability was found to depend on the ratio of the DW width w to the Fermi wavelength λ_F in an exponential fashion ($\propto e^{-w/\lambda_F}$). For DWs in the 10 nm range this contribution is negligible in ferromagnetic metals, because of the small Fermi wavelength of ≈ 0.1 nm.

Another model that was developed by Levy and Zhang for the application in metals takes into account spin-dependent potentials and scattering rates that are different for minority and majority spins [Lev97]. This picture is important in the current understanding of the GMR effect and it predicts a larger DW related resistance than the simple electron reflection model. The expected DW resistance from this model is larger for larger differences in the resistivities of spin up and down channels. Consequently it should be larger in high spin polarization material. The DWR is also predicted to increase with decreasing domain wall width. In order to get high DW resistivities, the spin must cross the DW non-adiabatically. This can be understood using a semiclassical picture. When the domain wall is wide, it takes a long time for the spin to ballistically traverse the wall. If this time is comparable to the precession time of the electron in the exchange field, then the spin never has a large angle with respect to the local magnetization direction and there is only a small resistance increase. Consequently, in a DWR experiment, the DW thickness should be made as small as possible.

5.4   Nonlinear Transport Properties of a Ferromagnetic Domain Wall

A somewhat different theoretical approach to the transport properties of magnetic domain walls is pursued in the model of the unipolar spin diode proposed by M. E. Flatté and coworkers [Fla01, Vig02]. The proposed spin diode consists of two adjacent layers with antiparallel majority carrier spin polarization. One possible experimental realization of this device is of course a magnetic DW between regions of opposite magnetization.

Again, it is found that for optimum results the domain wall should be thin enough that the spin of a passing carrier is not able to precess significantly. If the DW is thick and the carrier spin follows adiabatically the direction of magnetization, then an applied voltage will drop uniformly over the whole device length. Such a thick domain wall will exhibit a transport behavior similar to that of the host ferromagnet.

In contrast, if the domain wall is thin, then its resistance will be large compared to the bulk value and a charge current flowing through it will obtain nonlinear characteristics. These nonlinear I-V characteristics arise from a similarity between the energy band diagrams of a unipolar spin diode and those of a traditional nonmagnetic $p-n$ diode. This analogy, which is surprising at first, becomes obvious when considering Fig. 5.2. In the first column, the conduction and valence band edges of a regular $p-n$ diode are shown at zero bias, forward bias and reverse bias ($\pm eV$). The Fermi level is indicated by a dashed line and a charge current J_q flows under bias. The middle column is just a different visualization of the $p-n$ diode under the same respective conditions. The schematics in the middle column are easily understood by noting that in standard diagrams, the energies of the hole carriers in the valence band are negative relative to the chemical potential and the electron energies are positive. In the middle column, the energies of both carrier types are plotted as positive energies to emphasize similarities with the unipolar spin diode shown in the rightmost column of Fig. 5.2.

In both devices, the majority carriers on one side are minority carriers on the other side. Of course, in the case of the $p-n$ diode this applies to holes and electrons and in the unipolar spin diode this applies to spin up and down carriers. In the figure, the carriers of the spin diode are assumed to be electrons, however such a device could also be realized using p-type material. An important difference between a $p-n$ diode and the spin diode results from the different way the carrier energy bands shift under the application of an electrical bias.

In the $p-n$ diode, both the valence band and the conduction band edges shift up and down together under the application of a forward or reverse bias. As shown in Figs. 5.2d and 5.2e, forward biasing decreases both electron and hole transport barriers and creates a charge current J_q to the right that is due to an increased contribution of both minority and majority carriers.

On the other hand, applying the same (forward) bias to the spin diode has opposite effects on minority and majority electrons. As illustrated in Fig. 5.2f, only the barrier for the spin up electrons that move to the left-hand side is decreased. The barrier for the spin down electrons moving to the right-hand side is increased. Because the carriers are electrons, this results in opposite directions for the charge current J_q which flows to the right, and the spin current J_s which flows to the left.

When a reverse bias is applied, the charge current in the spin diode just changes its direction, there is no rectification as in the $p-n$ diode. The spin up current on the other hand is rectified,
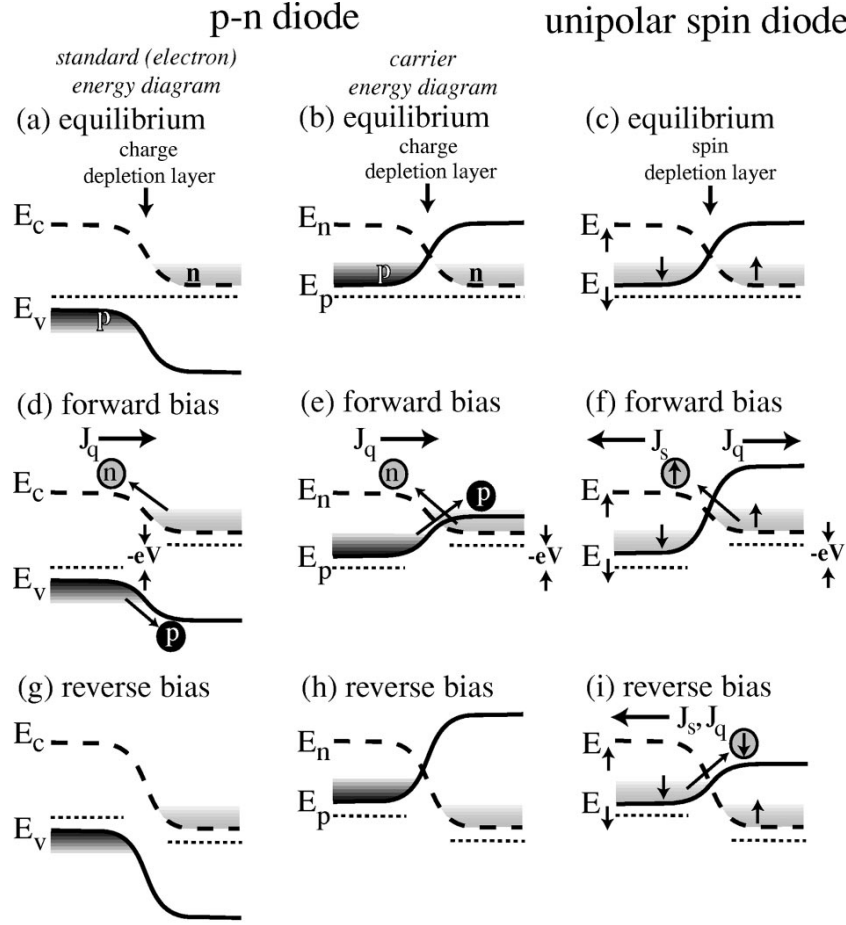
Figure 5.2: Standard and carrier energy diagrams for a p-n diode and the unipolar spin diode. Figure taken from [Fla01].

as the transport barrier for spin up electrons moving to the left is increased and the barrier for spin down electrons moving to the right is decreased.

When treating the unipolar spin diode in a similar way as an ideal $p-n$ diode, the resulting dependencies of charge current J_q and spin current J_s on the applied voltage V are

$$J_q = 2qJ_0 sinh\left(\frac{qV}{kT}\right),$$ (5.1)

$$J_s = 2\hbar J_0 sinh\left(\frac{qV}{2kT}\right)^2,$$ (5.2)

where $J_0 = Dn_m/L_m$, q is the electronic charge, V is the applied voltage, k is the Boltzmann constant, T is the temperature, D is the diffusion constant, n_m is the minority carrier density and L_m is the minority spin diffusion length.

For Equs. 5.1 and 5.2 to be valid, the following assumptions for an ideal Shockley diode must be satisfied:

   i. The voltage that is applied over the device should drop over the depletion region.

  ii. The Boltzmann approximation for transport is valid.

 iii. The injected minority carrier densities are small compared with the majority carrier densities.

 iv. No generation currents exist within the depletion region.

Assumption (i) is true in our case if the domain wall resistance dominates the device resistance. As will be shown below this is the case for constricted domain walls which can have a much higher resistance than regular Néel or Bloch walls. Assumption (ii) is satisfied in semiconductor devices as long as the applied voltages are on the order of the thermal energy. If the unipolar spin diode is realized using a host ferromagnet with a large spin polarization, i.e. when the spin splitting is large compared to the thermal energy, then assumption (iii) also holds true. Finally, assumption (iv) is satisfied as long as the spin coherence time is much larger than the transit time through the spin depletion region. This should also be increasingly satisfied for very short domain walls, where spin transport across the wall is ballistic.

In summary, the unipolar spin diode model for a sharp domain wall that dominates the device resistance predicts a strongly nonlinear voltage dependence of the DWR, according to Equ. 5.1. For large voltages ($qV > kT$) the DWR should exhibit an exponential decrease with increasing bias, with the slope equal to the thermal energy kT. Moreover, Equ. 5.1 predicts a constant DWR for the linear regime ($qV \ll kT$) and, according to [Vig02], leads to the well-known interfacial resistance of Valet and Fert (Equ. 2.56).

5.5   Geometrically Constrained Magnetic Wall

As mentioned above, measurements of the transport properties of a magnetic DW are facilitated by maximizing the DW resistivity by a choice of suitable experimental conditions. From an experimental point of view, the need for high DW resistivities arises from the fact that only above a certain DW resistance threshold, which is on the order of a few percent of the device resistance, can bulk contributions coming from AMR be unambiguously eliminated. Secondly, from the point of view of theory, all the models that are presented above imply that thinner or sharper domain walls have a higher resistivity. Consequently it is important to find a way to control and reduce the DW dimensions reliably.

A possible solution is pointed out in a theoretical work by P. Bruno, who investigates the structure and energy of a DW trapped in a constriction separating two wider ferromagnetic regions [Bru99]. He finds that constricted DWs constitute a new kind of domain wall. In contrast to Bloch or Néel walls, the structure and width of a constricted DW are determined by the details of the constriction geometry and not by the intrinsic anisotropies of the host ferromagnet. This work suggests that trapping DW in nanometer-sized constrictions can be an efficient tool to engineer their thickness.

Bruno's model consists of a ferromagnetic wire running along the x-direction in which there exists a single constriction. The wire cross section is given by $S(x) = S_0$ for $|x| \leq d$ and $S(x) = S_1 > S_0$ for $|x| \geq d$. Thus, the constriction is modelled as a step of width S_0 and length $2d$. The local magnetization direction inside the DW is assumed to remain in the *yz*

plane (similar to a Bloch wall) and is described by the angle $\theta(x)$ with respect to the z-axis. In this simplified model, the only contributions to the total energy E of the DW come from the exchange interaction between neighboring spins and an assumed uniaxial anisotropy. The DW energy is thus given by

$$E(\theta) = \int_{-\infty}^{\infty} dx \left[A \frac{d}{dx} \theta^2 + F(\theta) \right] S(x), \tag{5.3}$$

where A is the exchange stiffness and $F(\theta) = K cos(\theta)^2$ is the uniaxial anisotropy term. The structure of the domain wall is obtained by solving the differential equation

$$\frac{d^2\theta}{dx^2} + \frac{1}{S}\frac{dS}{dx}\frac{d\theta}{dx} - \frac{1}{2A}\frac{dF}{d\theta} = 0, \tag{5.4}$$

with the boundary conditions that $\theta(\pm\infty) = \pm\pi/2$ and $d\theta/dx(\pm\infty) = 0$. The second term in the differential equation is not present in the case of a regular Bloch wall, where the width of the ferromagnet is constant along the x-direction. However, it is needed here, because it expresses the influence of the shape of the constriction on the wall structure.

The solution of Equ. 5.4 leads to qualitatively different shapes of the DW depending on the values of the parameters w_0/d and S_1/S_0. Here, $w_0 = 2\sqrt{A/K}$ is the width of the unconstrained Bloch wall, whose properties only depend on material parameters host ferromagnet. Both when the regular Bloch wall is much shorter than the length of the constriction ($w_0/d \leq 1$) and when it is very long ($w_0/d \geq S_1/S_0$), then its width and energy are not much affected by the constricting geometry. The interesting case arises when $1 \leq w_0/d \leq S_1/S_0$. In this intermediate regime, the domain wall obtains completely different properties. For DW width w and energy E one gets

$$w \approx \frac{8d}{\pi^2} \ and \tag{5.5}$$

$$E \approx \frac{\pi^2 A S_0}{2d}. \tag{5.6}$$

Equations 5.5 and 5.6 show that the properties of constricted DW differ considerably from the properties of regular Bloch walls. The wall energy is purely determined by the exchange interaction, it is independent of the uniaxial anisotropy in the sample. Most importantly the structure and width of the constrained wall depend only on the geometry of the constriction and not at all on material parameters. Thus, if the constriction is very small, the width of a trapped DW can also become small and larger DW resistances can be expected.

5.6 Experimental Results: Very Large Magnetoresistance in Lateral Ferromagnetic (Ga,Mn)As Wires with Nanoconstrictions

The theoretical considerations presented in sections 5.4 and 5.5 lay out a clear path for measuring sizable magnetoresistance effects using domain walls. The key objective is to design an experiment such that the spin ballistic transport regime is reached. In other words: DWs need to be sufficiently thin such that a passing carrier does not adiabatically align its spin direction

with the local magnetization within the wall. Sufficiently thin DW can be obtained by pinning the wall in nanometer sized constrictions in lateral ferromagnetic wires. Only then can the DW dominate the resistance of the transport device and the $p - n$ diode analogy suggested by Flatté applies. Since this model also predicts an analogy with a GMR like geometry under some experimental conditions, only materials with high spin polarizations should be considered. These considerations have led to investigations of the domain wall resistance in lateral nanofabricated constrictions in single domain ferromagnetic (Ga,Mn)As wires.

5.7 Sample Details

5.7.1 Bulk Material Properties

The nanoconstriction samples described in the following were all patterned from the same wafer with number $ND - 20805b$. The material was grown by T.J. Wojtowicz in professor J.K. Furdyna's lab at the university of Notre Dame. It consists of a 19 nm thick epilayer of the ferromagnetic semiconductor $Ga_{1-x}Mn_xAs$ (x≈2.4%), grown on a semi-insulating GaAs (100) substrate by low temperature molecular beam epitaxy (LT-MBE).

The sample exhibits good structural, electrical and magnetic properties. This can be seen from the carrier density which is about 3×10^{20} cm^{-3} as measured by etch capacitance-voltage calibrations . This corresponds to more than 55% of the incorporated Mn being electrically activated, i.e. contributing one hole carrier to the valence band. The sheet resistivity at 4.2 K is about 4.5 k$\Omega/\square$. Assuming parabolic bands and the same effective hole mass as in GaAs, $m^* \approx 0.5m_o$, where m_o is the free electron mass, these values imply a free hole model Fermi energy $E_F \approx 150$ meV, a Fermi wavelength $\lambda_F \approx 6$ nm, and a transport mean free path $l_t \approx 1$ nm. The Curie temperature of the as grown material is 65K, determined by SQUID. Fig. 5.3 is a measurement of the remanent magnetic moment of the layer after the sample was cooled in zero field from room temperature. The sample was magnetized at low temperatures along a magnetic easy axis. The applied magnetic field was then brought back to zero and the magnetic moment was measured upon heating. No significant magnetic moment is present above the Curie transition temperature. This shows that there are no appreciably detectable ferromagnetic inclusions present in the sample, a further characteristic of a high quality (Ga,Mn)As random alloy.

Figure 5.3b shows a SQUID measurement of the hysteresis of a piece of bulk material. The material is oriented with its [100] crystal direction parallel to both the magnetic field and the direction of sensitivity of the SQUID. The hysteresis loop is square-like with the magnetic moment at zero field being very close to the saturation value. The coercive field is ≈12 mT. Figure 5.4 shows a magnetoresistance measurement taken at T=4.2 K on a Hall bar patterned along the [100] (or equivalent) crystal direction. The magnetic field is applied parallel to the current. The sharp peaks around $|B| \approx$10 mT are associated with an easy axis magnetization reversal of the layer and their position fits to the SQUID hysteresis data. The inset shows the same measurement up to fields of ±500 mT. The sample resistance decreases slightly and monotonically with increasing fields which is due to the well-known negative isotropic magnetoresistance of bulk (Ga,Mn)As. A measurement of the transverse voltage in the same geometry reveals that during the whole magnetic field sweep the in plane Hall effect remains zero. Both the magnetic
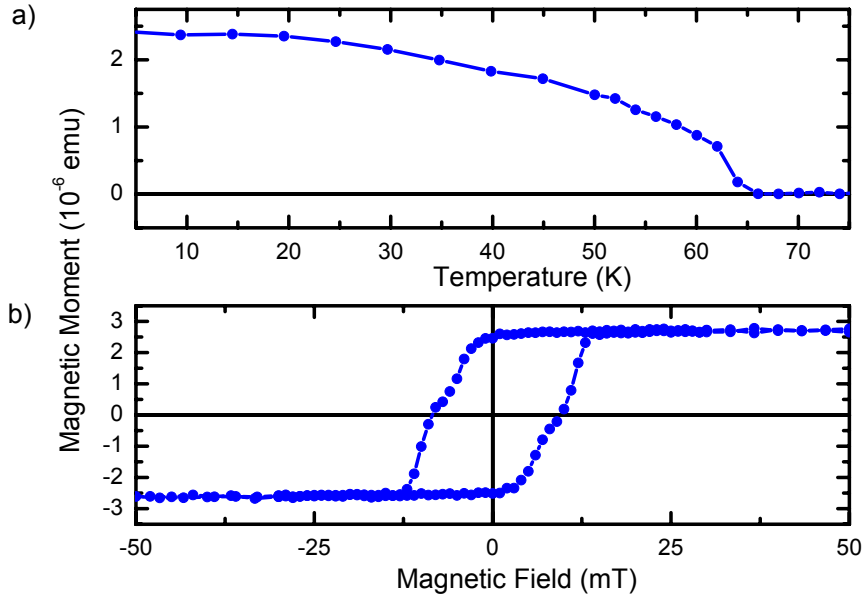
Figure 5.3: Bulk magnetic properties of wafer ND-20805b. a) Measurement of the Curie temperature. $T_c \approx 65K$, indicating high quality bulk material. b) Square-like hysteresis with the magnetic field along the [100] crystal direction confirms this direction to be the magnetic easy axis of the thin film.

data shown in Fig. 5.3 and the transport data shown in Fig. 5.4 thus establish that the magnetic easy axis of the bulk material is along the [100] crystal direction. This is consistent with and expected from theoretical and experimental results on similar bulk material, as for example presented in [Saw04].

5.7.2 Sample Layout and Fabrication

Figure 5.5 shows the basic sample design that was used to examine domain wall related resistance effects presented in this section. The transport sample consists of two outer 400 nm wide and 10 μm long wires and a narrow 100 nm wide and 500 nm long island in between them. The inner island and the outer wires are joined via two nanoconstrictions located left and right of the island region, as schematically depicted in Fig. 5.5b. Depending on the exact parameters during the fabrication process, the length of these nanoconstrictions can fall below 10 nm. Figure 5.5a is a SEM picture presenting a full view of the whole transport structure. In this image it can be seen that the outer 400 nm wide wires are contacted by four electrodes. The outer pair of electrodes serve as current leads. The inner pair of electrodes join the 400 nm wide wires close to the constrictions, serving as voltage leads.

The fabrication of the samples was done by Tanja Borzenko. In the first step of the process, the four large contact pads were defined on the (Ga,Mn)As layer by e-beam lithography, evaporation of a W sticking layer followed by a Au layer and lift-off. Subsequently, contact leads, nanowires and the constrictions were defined by negative electron beam lithography (30 kV acceleration voltage). Chemically Assisted Ion Beam Etching (CAIBE), a Cl_2 based dry
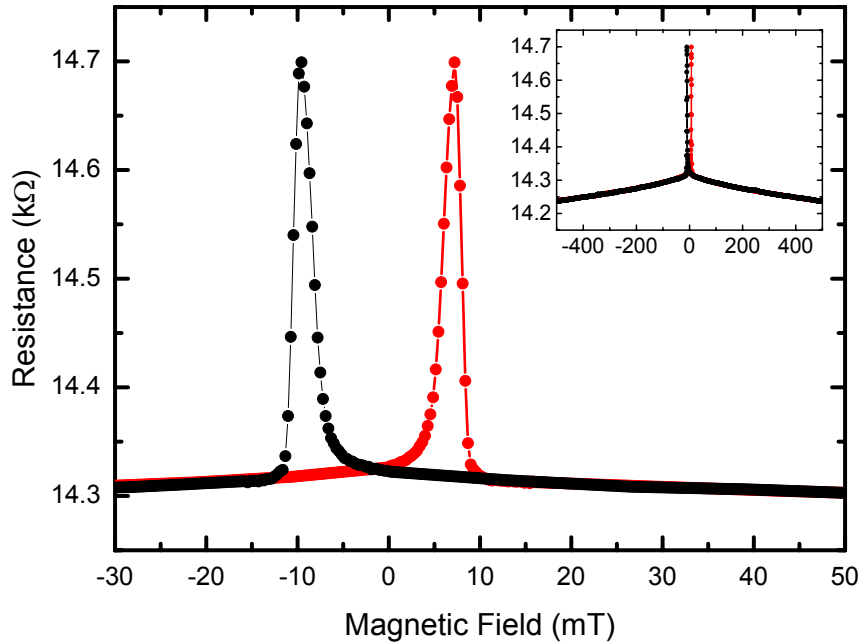
Figure 5.4: Bulk transport properties of layer ND-20805b at T=4.2 K. The magnetoresistance measurement shown was taken on a Hall bar structure with the current running along the [100] (or equivalent) crystal direction. The magnetic field is applied parallel to the current path.

etching process, was used in order to etch through the exposed (Ga,Mn)As layer, leaving a (Ga,Mn)As mesa only underneath the photoresist and the metallization.

5.7.3   Design Considerations

The double constriction sample layout was very carefully designed in order to be able to unambiguously detect domain wall related resistance effects.

Firstly it is imperative that the measurement of ferromagnetic bulk resistance effects be avoided. Here especially unwanted admixture of contributions coming from anisotropic magnetoresistance has to be prevented. Thus, the goal is to continuously control the direction of the magnetization during the experiment by making certain directions energetically favorable. During lithography, the island and outer wires were carefully oriented along the magnetic easy axis of the bulk (Ga,Mn)As. Furthermore, the large aspect ratio of island and wire introduces a large amount of shape anisotropy that also makes it energetically more favorable for the magnetization to lie along the [100] direction. Thus, crystalline and shape anisotropy energies add up and both tend to align the magnetization parallel or antiparallel to the current path. Hereby, AMR-related artifacts in magnetoresistance measurements are avoided.

A domain wall is the separation between two magnetic domains of non-collinear orientation. The observation of domain walls is facilitated when these neighboring domains have very different switching fields. In the present sample design this is achieved by introducing two constrictions, i.e. by defining the magnetic island structure. In order to understand the advantages of using two constrictions as compared to only one, one has to note that the transport nanowires
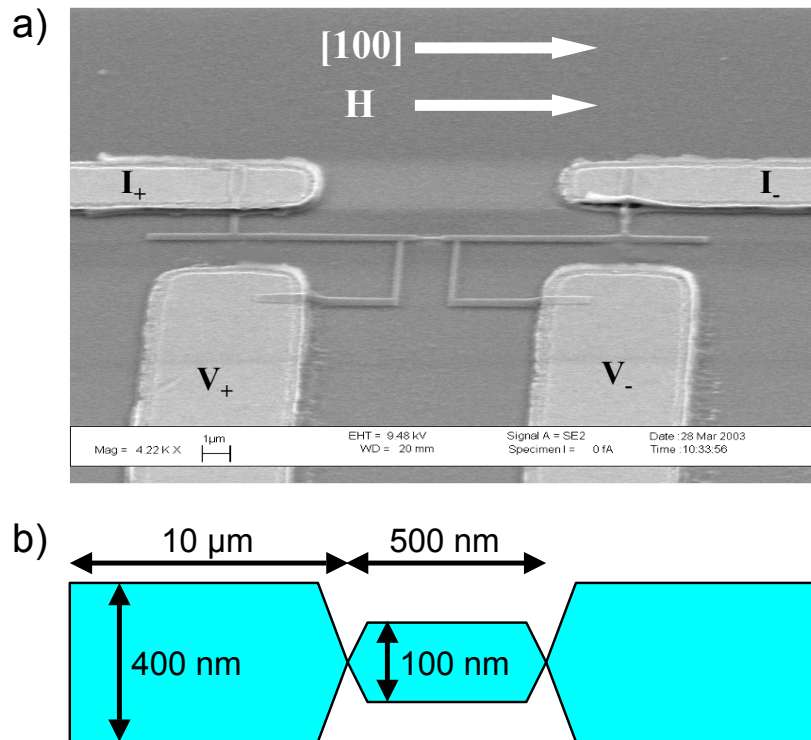
Figure 5.5: a) SEM picture giving a full view of a double constriction transport structure. The two outer contact pads and electrodes serve as sources of electric current through the nanostructure. The two inner electrodes are used to measure the corresponding voltage drop. b) Schematic of the inner island and the two constrictions giving the sample dimensions.

are connected to micron-sized electrical contact pads by means of (Ga,Mn)As mesas. Shigeto et al. have investigated the influence of large pads attached to the ends of magnetic wires on the switching behavior of the wires [Shi99]. Their samples are 150 nm wide wires patterned out of a NiFe/Cu/Co trilayer structure. As sketched in Fig. 5.6, two types of wires are investigated: one of the wires has a symmetrical shape with two flat ends and the other one has a square pad ($0.5\mu m \times 0.5\mu m$) attached to an end.

The detection scheme for the injection of a domain wall into the nanowire is a measurement of the GMR signature of the wire while an external magnetic field is swept in a direction parallel to the wire axis. By observing the locations of the resistance jumps in the magnetoresistance of the wires (compare the measurements shown in Fig. 5.6a and b) it is found that the Co layer of wires with a pad exhibits a dramatically reduced coercivity. This is attributed to a much lower domain wall nucleation energy in the large pad as compared to at the flat end of a wire. The process works as follows: After nucleation in the pad, the domain wall then propagates to the connection between the large pad and the nanowire where it is briefly pinned. At slightly higher fields it is injected into the nanowire, thus reversing its magnetization direction. Both the domain wall nucleation and depinning fields are much lower than the Stoner Wohlfarth switching field of the nanowires and thus the magnetization reversal is determined by the domain wall depinning energy. In a later publication by Yokoyama et al., the magnetization reversal
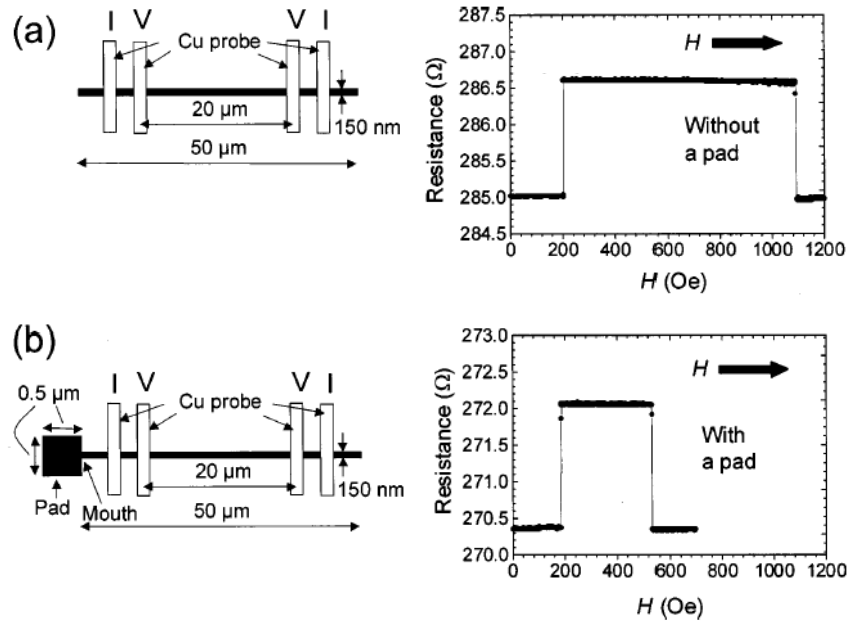
Figure 5.6: Investigation of the dependence of the domain wall-induced switching of ferro-magnetic wires on the shape of the wire ends. It is clearly found that wires with a square pad attached to one end (b) switch at much smaller magnetic fields than regular wires without a pad (a). Pictures taken from [Shi99].

process of NiFe wires with and without a square pad at one end was directly observed using Kerr microscopy images [Yok00]. The authors clearly observe and confirm that domain walls are preferably nucleated in the large magnetic pads and that these pads decrease the coercive field of the attached wires. When applying these observations to the sample structure shown in Fig. 5.5, an advantage of the double constriction design becomes immediately clear. The outer wide wires can be expected to switch at comparably low fields due to the introduction of domain walls from the large electrical contact pads. In contrast, the thin island will switch at much higher fields due to a higher domain wall nucleation energy, shape anisotropy and due to it being isolated from any sources of domain walls. As soon as domain walls are injected into the outer nanowires they will travel along the wires until they reach the constrictions. If the constrictions are sufficiently thin, they can act as energy barriers against further domain wall progress. If there was only one constriction, the two domain walls coming from opposite side would meet in the constriction area and possibly annihilate each other already at comparably low fields. In summary, the double constriction design can be expected to strongly enhance the regime where domain wall related effects can be observed.

In the above sections 5.3ff. it was justified why it is favorable to observe domain walls that are constricted or contained in mesoscopically small volumes. Quite naturally there exist a mul-titude of possible experimental realizations of the desired point contact geometry. For example, besides the approach to lithographically pattern appropriate samples, the pertinent literature also contains reports about mechanically established point contacts between separate pieces or parti-cles of ferromagnetic material. Among the employed sample types are millimeter-sized pointed

Ni wires that are joined in one point by means of a mechanical force [Gar99], a Ni electrodeposition technique that is self-terminating as soon as an electrical point contact between the two active electrodes is established [Hua03], junctions between carbon encapsulated Co magnetic nanoparticles and an electrodeposited Co and NiFe matrix [Weg03] and many other schemes. Whenever the employed method relies on electrically joining two separate magnetic pieces or particles, then a major difficulty lies in the fact that observed features of the magnetoresistance can originate from magnetostriction rather than from a ballistic magnetoresistance effect. Magnetostriction is the changing of a material's physical dimensions in response to changing its magnetization. In other words, a magnetostrictive material can become smaller or larger when it is subjected to an external magnetic field. It is the magnetic equivalent of the piezoelectric effect. The magnetostrictive coefficient L is most commonly defined as the fractional change in length as the magnetization increases from zero to its saturation value. Most ferromagnetic materials exhibit some measurable magnetostriction. Ni for example is known to exhibit negative magnetostriction. It is obvious that if an experimental technique relies on a measurement of the resistance of two pieces of Ni that are just barely touching on the atomic level, even minute influences of negative magnetostriction can create huge and unwanted magnetoresistance effects. However, magnetostriction has been effectively avoided in the double constriction sample layout. The transport sample is lithographically patterned out of a thin (Ga,Mn)As layer that is MBE grown onto a quasi lattice matched low-temperature GaAs buffer layer. The geometry of the nanowires and constrictions are thus fully constrained by the underlying crystal lattice and magnetostriction is not an issue.

The fact that two constrictions are used in the transport sample instead of one has an advantage concerning the voltage measurement. Symmetric designs avoid the unwanted measurement of thermoelectric voltages: In a single constriction, a thermovoltage can in principle develop between the two regions of opposite magnetization. In our sample however, when two constrictions are connected in series, the thermovoltages will be of opposite sign in the two constrictions and therefore cancel.

One final advantage of our sample lies within a detail of the fabrication process. The negative electron beam lithography allows to multiply apply further lithography steps even when the sample is already in its final state, i.e. mounted and bonded inside the chip carrier that is used for the transport measurements. This comes from the fact that a negative lithography process relies on the principle that photo resist remains on the surface of the sample after the exposure. The last exposure step on the double constriction sample consists of defining electrical leads, the nanowires and the constrictions. Thus, as can be seen from the false-color SEM image in Fig. 5.5, the resist is still present on the wire after the lithography is finished. This allows to administer multiple etching steps on the sample anytime they are needed during the experiment. At the same time, the usage of dry instead of wet etching protects the chip carrier used for the electrical measurements. As will be shown later, the re-etching can be used as an effective tool to further decrease the constriction size and thus to enhance domain wall related resistance effects.

5.8   Measurement Details

All electrical measurements on the double constriction samples and on control samples without a constriction are carried out at 4.2 K in a He bath cryostat fitted with a superconducting magnet. The magnetic field is aligned parallel to the current direction and the axis of the nanowires is carefully aligned along the [100] or equivalent crystal direction, which is the magnetic easy axis of the bulk (Ga,Mn)As thin film. All electrical measurements are done in the four-probe geometry using DC currents only. An eight-channel Adlink analog output card model PCI-6208V is used as the DC current source and to control the magnitude of the magnetic field. For measurements with a voltage bias <10 mV the usage of a $1000 : 1$ voltage divider consisting of two metal-oxide resistors that are connected in parallel ensures a low DC voltage offset (<5 μV) and low electrical noise input from the current source. The output resistance of the divider is very small compared to the sample resistance and thus all electrical measurements are done in constant-voltage mode. Four-probe electrical measurements are done by injecting a DC current by means of the outer pair of electrical contacts (refer to Fig. 5.5). The actual measurement is done by connecting a custom-built ultra-low input resistance, zero offset current to voltage converter in series with the sample and then measuring the amplified output voltage. The corresponding voltage drop over the constrictions and the island is measured using the inner contact pair and a zero-offset voltage preamplifier. During a measurement of the magnetoresistance, the magnetic field is varied from full negative saturation of the magnetic material to full positive saturation and back. Measurements of the current-voltage characteristics of the sample are done by first bringing the sample into a desired magnetic state and then sweeping the excitation voltage.

5.9   Simple Model for Magnetoresistance

Figure 5.7 schematically depicts the expected magnetization and resistance response of a double constriction sample during a sweep of the external magnetic field.

The initial state (a) corresponds to a large negative magnetic field (i.e. pointing to the left) being applied along the wire axis. The magnetic field is strong enough such that the wire as well as the island magnetizations are pointing to the left. This corresponds to a parallel alignment of the magnetizations. The sample is assumed to be mono-domain, i.e. there are no domain walls present in the transport structure. The sample exhibits a low parallel magnetization state resistance R_P. While the magnetic field is swept to zero, the sample magnetization simply remains in its parallel state since the wire axis is the easy axis of the transport structure due to a combination of crystalline and shape anisotropy. When the magnetic field is swept into the positive direction, then the outer wires reverse their magnetization first. As pointed out above, the relatively low coercive field of these wires comes from the fact that they are connected to large contact pads that act as domain wall sources. After the domain walls are swept in from the contacts pads, they travel along the outer wires and are eventually trapped inside the constrictions. This antiparallel state (b) manifests itself as a sharp increase in resistance, the additional resistance being caused by the trapped domain walls.

Then, at slightly higher fields, the island structure switches as well. Its switching behavior is dominated by strong shape anisotropy. Consequently the sample is once again in a low
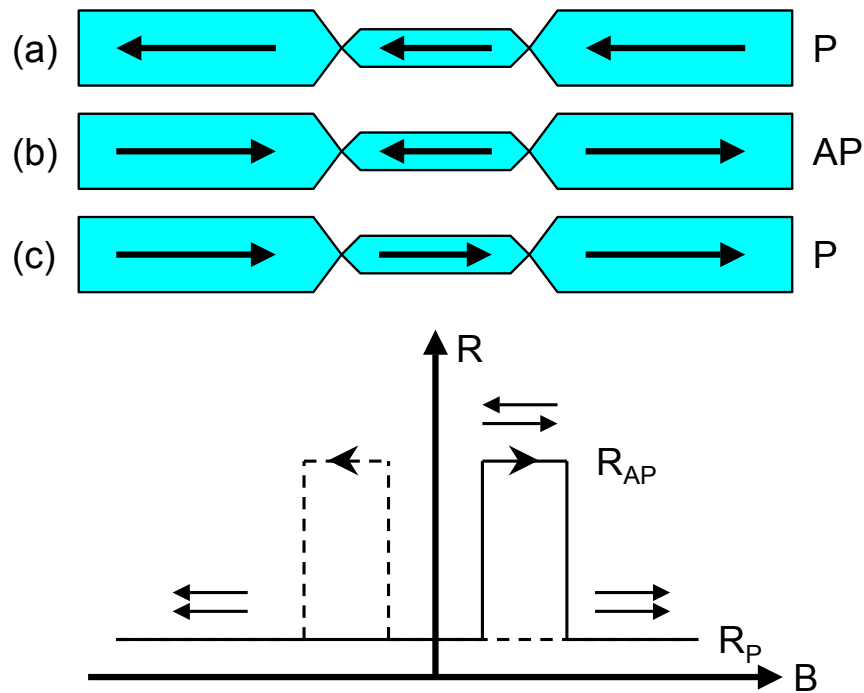
Figure 5.7: Expected magnetoresistance behavior for a double constriction transport sample. Upper part: schematic of the sample with expected magnetization alignment of wires and island. Lower part: Spin valve-like magnetoresistance due to domain walls being trapped in the constrictions during antiparallel magnetization alignment.

resistance, parallel magnetization state. A measurement of a full hysteresis loop of a double constriction sample leads to a spin valve-like magnetoresistance as schematically shown in the lower half of Fig. 5.7.

5.10   Experimental Results

In this section, the various experimental results on double constriction samples will be presented. Although all the experimental samples exhibit the above presented switching behavior and spin valve-like magnetoresistance, the results strongly depend on the resistance of the constriction area. An observation common to all samples is that the magnetoresistance increases with increasing constriction resistance. Furthermore it is found that two different transport regimes can be realized using the same basic double constriction geometry, also depending on the size of the constrictions. Measurements on samples where transport through the constriction is still classically allowed, i.e. where transport is in the diffusive regime will be presented first. These samples show a maximum positive magnetoresistance of $\approx 8\%$. It is also found that when the constriction dimensions are reduced beyond a certain critical dimension, surface effects play a role. This means that in the smallest constrictions under investigation (10 nm width and below), an electrically depleted surface layer can lead to the formation of a tunnel barrier in the constriction region. A further finding is that these high resistance samples exhibit

magnetoresistance effects that can be larger by more than two orders of magnitude than those found in low resistance constrictions. Quite naturally this means that the modelling for the two groups of samples has to be qualitatively different as well.

5.10.1   Domain Wall Resistance in the Diffusive Regime

Sample ND-20805b-T3-3

Figure 5.8 shows a four probe magnetoresistance measurement of a representative double constriction structure (sample number ND-20805b-T3-3). The experiment was done at a temperature of T=4.2 K and with a constant excitation voltage of V=450 μV. The four terminal resistance of the device is $\approx$48 kΩ.

As described above, during the magnetoresistance measurement the magnetic field is applied along the wire axis and swept from full positive to negative saturation of the magnetization and back. During both sweep directions, the outer wires reverse their magnetization first, inducing an antiparallel alignment of the island and the wires. Due to domain walls being present in the constrictions, the resistance increases from $\approx$ 48.7 kΩ to $\approx$ 49.2 kΩ. At higher magnetic fields, the island structure switches as well and the sample returns into the low resistance state.

The resulting magnetoresistance has a spin valve-like shape that is defined by sharp switching events. The spin valve feature is positive with a maximum amplitude of $\frac{R(B)-R(0)}{R(0)} \approx 1\%$. However, due to the sample geometry the measured resistance also contains a significant contribution coming from the island and part of the wires lying between the voltage probes.

By using the bulk sheet resistance of 4.5 kΩ/$\square$ and an assessment of the sample area between the voltage leads from SEM microscopy pictures, one arrives at a parasitic series resistance of roughly 40 kΩ. Thus, the parallel magnetization state resistance of each constriction is about 4400 Ω. The absolute height of the spin valve feature is about 500 Ω, measured between the resistance at zero magnetic field and the low field resistance of the peak. The height of this feature is a direct measurement of the resistance of the trapped domain wall. Thus, the ratio between the domain wall resistance to the "pure" constriction resistance is $\approx$ 6%.

Four probe I-V curves measured at various magnetic field positions on and off the resistance peaks show ohmic behavior up to V=5 mV, which corresponds to roughly 14 times the thermal energy. Consequently, nonlinear effects are not expected and are not observed in this low resistance sample for the mentioned bias range.

In order to investigate the influence of the sample geometry on the switching behavior of the (Ga,Mn)As, the locations of the switching events in Fig. 5.8 have to be compared with the bulk values extracted from the SQUID hysteresis measurement and the anisotropic magnetoresistance signature of the Hall bar shown in Figs. 5.3 and 5.4, respectively.

Both the bulk SQUID sample and the Hall bar switch at $\approx$ 10 mT, whereas in the double constriction sample the outer wires switch at a slightly higher field of 15 mT. This value which is close to but slightly higher than the bulk value is compatible with the wires switching due to domain wall injection from the large electrical contact pads. The switching of the 100 nm wide island structure occurs at even higher fields, as indicated by the sharp steps at $\approx$ +75 mT and $\approx$ −60 mT, respectively. This is evidence that the double constriction design successfully incorporates shape anisotropy and strong domain wall pinning in the constrictions.

Further evidence that the magnetization reversal of the island structure is determined by its
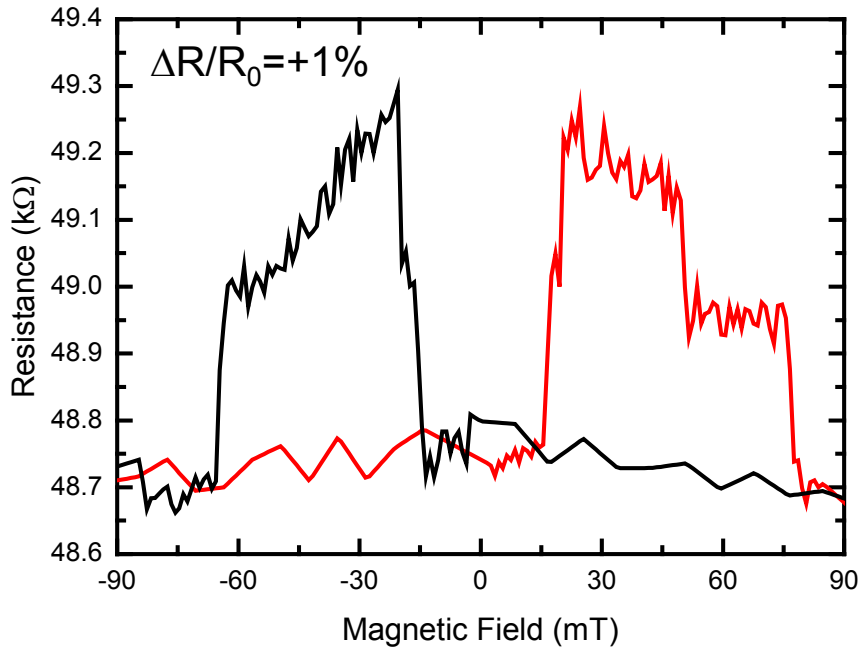
Figure 5.8: Magnetoresistance measurement of sample ND-20805b-T3-3 (as fabricated). The sample shows 1% positive magnetoresistance due to domain walls being trapped inside the constrictions.

shape is presented in Fig. 5.9. The blue data represents a SQUID hysteresis measurement on an as grown piece of wafer ND-20805b measured at $T = 4.2$ K and magnetic field along the [100] easy axis. The wider hysteresis loop was measured on an array of lithographically patterned mesas of width $w = 100$ nm and length $l = 500$ nm, made from the same material. The separation of neighboring mesas is 100 nm. The mesas have the same dimensions as the inner island in the transport structures. Their long axes lie along the [100] easy axis of the (Ga,Mn)As and the magnetic field is applied along the axes. Since the SQUID signal depends on the magnetic volume of the sample, the array has to consist of millions of wire elements to gain a sufficient signal to noise ratio. This inevitably leads to a statistical distribution of magnetic properties among the array elements which partly explains the elongated shape of the array hysteresis loop. Secondly, it can be assumed that neighboring elements couple magnetostatically to a small extent, which also broadens the shape of the curve. Nevertheless the array hysteresis loop is much wider than the bulk hysteresis loop and the observed high coercivity is consistent with the transport data. Thus the magnetic data corroborates the conclusion that indeed the island magnetization reversal is characterized by a strong shape anisotropy influence.

Besides the main switching features in the transport experiment shown in Fig. 5.8, a few other characteristics of the spin valve features deserve some attention. The locations of the final island switching fields are not hysteretically symmetric, as they are located at $\approx +75$ mT and ≈ -60 mT. Furthermore, there is an additional switching event at intermediate positive magnetic fields ($\approx +50$ mT) which is not there at negative fields. This indicates that the pinning and depinning process for domain walls in the constrictions is different for the different magnetic field sweep directions. A likely explanation for this is that the microscopic structure of
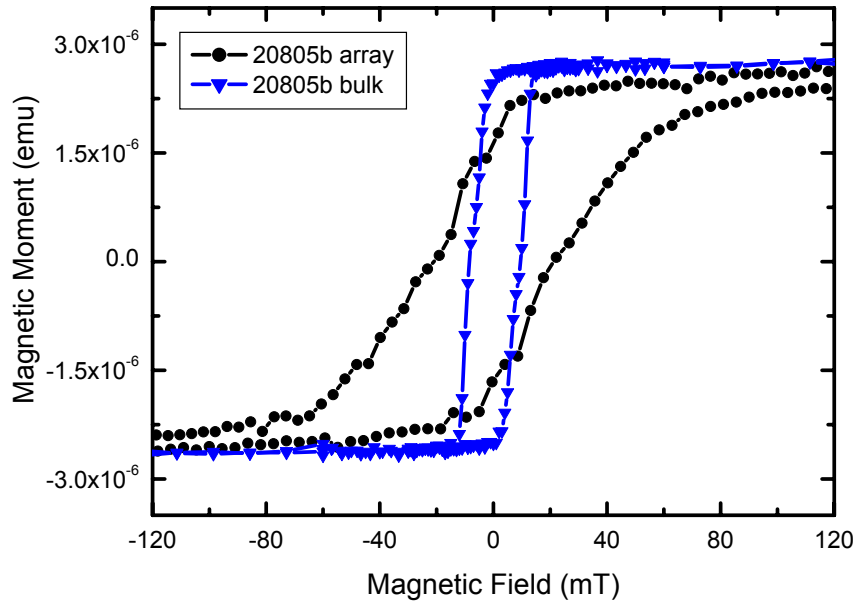
Figure 5.9: Comparison of two SQUID hysteresis measurements with field along the [100] crystal direction. The blue dots are data measured on an as grown piece of wafer ND-20805b and the black dots are measured on a lithographically patterned array of mesas of width $w = 100$ nm and length $l = 500$ nm, made from the same material. The mesa axes lie along the [100] crystal direction. It is clearly seen that the shape anisotropy induced by the patterning enhances the coercivity.

the transport sample is not completely symmetric. This is caused by the lithography process which inevitably creates a certain fine structure on top of the intended idealized design. Surface roughness on the scale of at least several Ångstroms is to be expected and can certainly influence domain wall dynamics.

Another interesting observation is that the top of the spin valve feature that is located at negative fields is of triangular shape. For both peaks, the maximum resistance occurs directly after the domain wall is trapped inside the constrictions. As the magnetic field amplitude is increased, the domain wall resistance decreases almost linearly. According to the qualitative considerations of domain wall resistance presented in sections 5.3ff. this can be explained by a gradual increase of the domain wall thickness in increasing magnetic fields. While the wall is still pinned, its increasing Zeeman energy causes it to stretch and the resistance goes down. While this is a continuous process in negative fields, it is more of a two-step process at positive fields: a small and continuous amount of stretching is followed by a rather abrupt widening at $\approx +50$ mT and finally a depinning of the domain wall at $\approx +75$ mT.

Sample ND-20805b-T3-3, Field Perpendicular to Plane

Figure 5.10 presents four probe magnetoresistance measurements done at T=4.2 K with magnetic fields up to 3 T applied perpendicular to the plane of double constriction sample ND-20805b-T3-3 (panel a) and a simple nanowire of width w=100 nm (panel b).
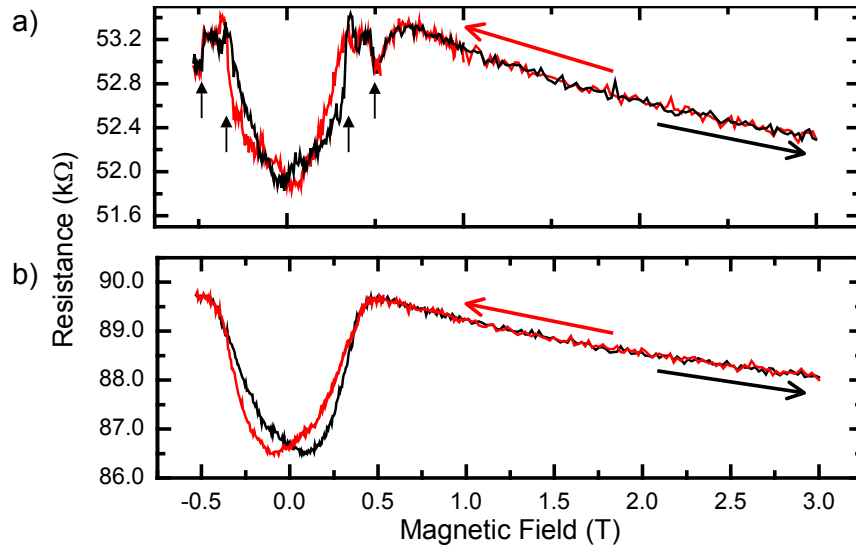
Figure 5.10: Magnetoresistance measurements with the magnetic field perpendicular to the plane of a) double constriction sample ND-20805b-T3-3 and b) a simple nanowire of width $w = 100$ nm.

Both samples initially show a $\approx 3\%$ increasing positive magnetoresistance that saturates around $|B| = 0.5$ T. The gradual resistance increase, the high saturation field and the lack of clear hysteretic openings in the magnetoresistance reveal that this is just a manifestation of the anisotropic magnetoresistance effect as the magnetization is slowly rotating out of plane. At fields higher than $|B| = 0.5$ T, the resistance gradually decreases almost linearly. Since at these fields the magnetization direction is already stable and pointing along the magnetic field, this clearly is the well known bulk negative magnetoresistance of (Ga,Mn)As .

Interestingly, the double constriction sample shows additional sharp resistance jumps of approximately ± 400 Ω at the positions indicated by the small vertical arrows in the figure. These features are completely absent in the measurement of the single magnetic wire and their absolute height is consistent with the domain wall resistance measured with field in the plane of the layer. This could indicate that also in this geometry domain walls can be trapped and measured inside the constrictions. However, the microscopic magnetization dynamics that are being caused when the field is applied perpendicular to the sample can be rather complicated. Thus, the exact interpretation of all the fine structure in Fig. 5.10 is unclear and has not been pursued any further.

Sample ND-20805b-T3-3 After Additional Etching Step

The results presented in the previous section are evidence that the constriction size of the sample was small enough to efficiently serve as a pinning center for the domain walls sweeping through the nanostructure. The domain wall resistance that was measured constitutes 1% of the whole device resistance and 6% of the constriction resistance alone. In this regime, no nonlinearities are found in the investigated bias range. Unfortunately, the exact dimensions of these particular constrictions is unknown.

The reason for this is that a SEM microscopy measurement of nanoscale semiconductor dimensions is very risky in terms of the electrical properties of the sample. Subjecting semiconductor structures in general and especially those located on insulating substrate materials to electron beam irradiation causes electrostatic charging of the structures. This charging is a potential threat for especially the smallest nanostructures, as the high electric fields that are involved can cause electrostatic discharge. Electrostatic discharge chiefly happens between pointed structures that are close together, e.g. the nanoconstrictions. To circumvent this problem, SEM pictures were only taken on test structures for lithography, not on the final set of samples.

Another reason not to take SEM pictures on the final samples is that exposure to an electron beam forms a conducting layer on the surface of the carbon containing negative photoresist. Although being of relatively high impedance, it can nevertheless be a considerable source of parasitic parallel conduction. The drawback of this policy is of course that working samples that exhibit different properties cannot directly be compared with each other in terms of their exact constriction dimensions.
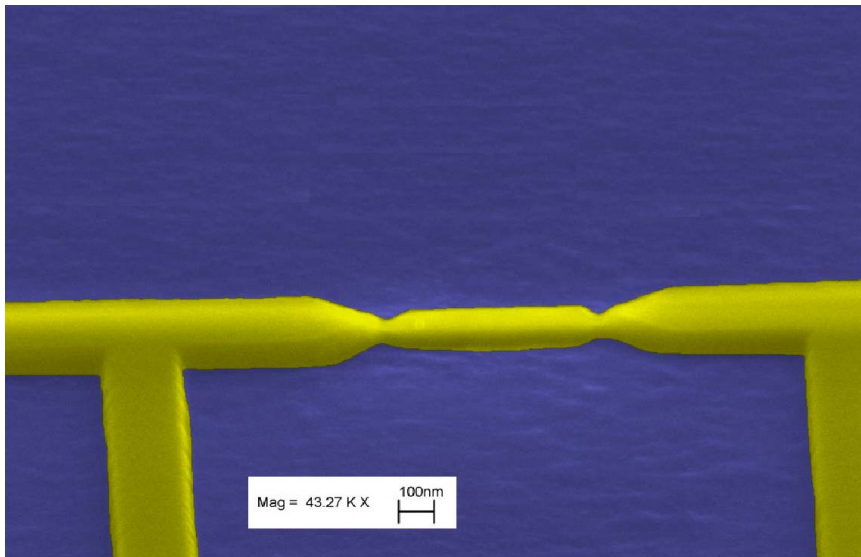

Figure 5.11: False-color SEM picture of a double constriction viewed from top and sideways. Shown are parts of the outer wires together with voltage leads left and right of the island. The slight material contrast seen in the picture on top of the wires shows that resist is still present on the wires.

However, the negative electron beam lithography process opens up a way to study the influence of the constriction size on the properties of trapped domain walls. Figure 5.11 shows an example of a double constriction viewed from top and sideways. The figure is a false-color image capturing the two constrictions along with parts of the outer wires and the voltage leads left and right of the island. A closer examination of the picture reveals a slightly differently colored layer on top of the whole transport structure. This is the negative electron beam resist that has been exposed to the electron beam during lithography. The fact that it remains on the sample is a natural by-product of the negative lithography technology. The photo resist over-

layer is in fact hardened in the course of the chemically assisted ion beam etching step. Thus, after finishing the electrical measurements on sample ND-20805b-T3-3 in its original state, the sample was subjected to a short additional etching step.

The photo resist overlayer acts as a protective capping layer and thus the etching process proceeds only at the side walls of the transport structure. The etch rate is independent of the geometry of the sample and of the crystal direction since chemically assisted ion beam etching is an isotropic process that produces little or no undercut. This means that the width of the nanostructure is reduced by roughly the same amount everywhere. Obviously, the only significant effect of this etching step is to be expected in the constriction area which has the smallest diameter. By keeping the duration of the etching step sufficiently short, the width of the constrictions is reduced while at the same time preserving their integrity and leaving the rest of the sample effectively unchanged.

Figure 5.12 is a magnetoresistance measurement of sample ND-20805b-T3-3 after it was subjected to a second etching step. The measurement was taken at a temperature of T=4.2 K and a four probe excitation voltage of V=300 μV. A comparison with Fig. 5.8 reveals the important changes due to etching changes.

The additional etching increased the sample resistance of the parallel magnetization state from $\approx$ 48 kΩ to $\approx$ 78 kΩ. Because of the etching mechanism described above, the additional resistance can be attributed almost entirely to a narrowing of the constrictions area. Subtracting 40 kΩ of series resistance, the constrictions now have a resistance of $\approx$ 20 kΩ compared to the previous 8.5 kΩ. Furthermore, the spin valve-like magnetoresistance feature is increased even more. The domain wall resistance is now 8% that of the parallel magnetization resistance. Repeated magnetoresistance measurements under identical conditions reveal that the details on top of the features can change. As described above, the sample in the as-fabricated state already shows some fine structure which was completely reproducible between successive experiments.

The fine structure on the 8% sample however does not completely reproduce between measurements, as seen in Fig. 5.12. There are a number of characteristic fields at which the sample jumps into one of a number of characteristic resistance states. However, the detailed shape of the feature varies from sweep to sweep.

This is again very likely caused by the existence of pinning sites in the constriction area. Due to the small dimensions realized here, impurities and side-wall roughness caused by the additional etching act as strong pinning centers. Compared to the as-fabricated sample, they can be expected to exist in higher numbers and have a stronger influence on the domain wall properties.

The exact microscopic nature of such pinning centers determines the de-pinning field. The different pinning sites yield different geometrical confinement of the domain wall which has a profound influence on its resistance. The microscopic distribution of the pinning center characteristics thus leads to the observed magnetoresistance fine structure.

Figure 5.13 displays the voltage dependence of the magnetoresistance at T=4.2K of sample ND-20805b-T3-3 in the re-etched state. During the measurement, the four probe voltage drop was adjusted between 0.3 and 9.0 mV. This range corresponds to energies ranging from just below the thermal energy up to 25 k_BT.

For each voltage, the sample magnetization was saturated using a large negative magnetic field and the spin valve signal was subsequently measured. Both the right hand side resistance on top of the peak as well as the resistance of the baseline decrease monotonically with increas-
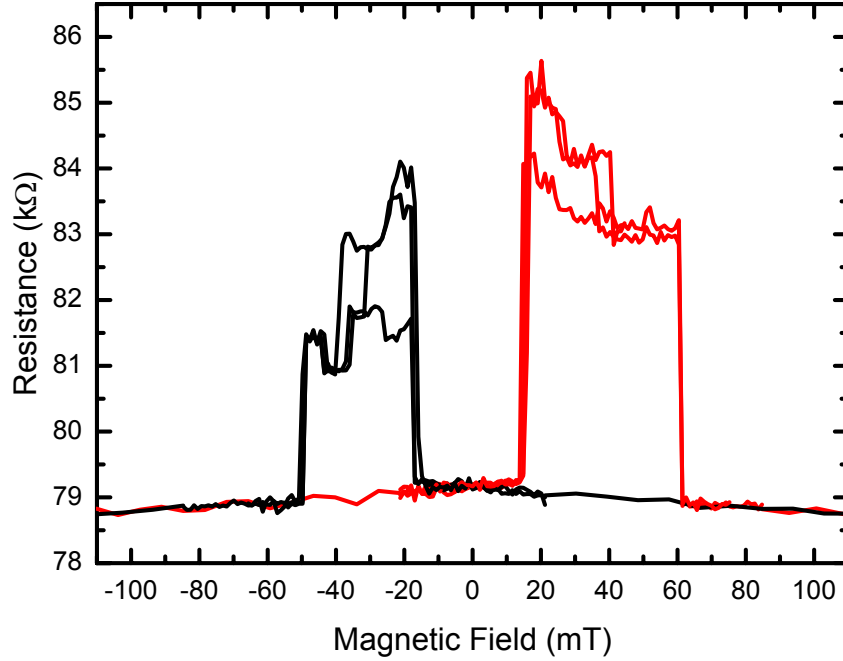
Figure 5.12: Magnetoresistance of sample ND-20805b-T3-3 after it was subjected to a second etching step. The measurement was taken at T=4.2 K and a four probe excitation voltage of V=300 μV.

ing bias. However, the peak resistance decreases even faster than the baseline resistance and so the overall magnetoresistance decreases as well. The nonlinearities are also demonstrated by Fig. 5.14 which contains three conductance spectra taken at various magnetic fields on and off the peak.

It can also be seen that the fine structure on the peak is not present above V=4.6 mV. This is perhaps an indication that higher current densities can influence the pinning dynamics of the domain wall.

Both field directions of the magnetoresistance show a similar bias dependence. However, for the sake of clarity only positive magnetic fields are shown in the picture.

The nonlinear behavior is not present in the as fabricated sample. It is thus a consequence of the second etching step, the narrowing of constrictions and the resulting properties of the constricted domain wall.

One result of the unipolar spin diode picture of domain walls (described in detail in section 5.4) is that domain walls are inherently nonlinear objects. This becomes clear when considering regular p-n diodes and is explicitly demonstrated by the current voltage characteristic of a domain wall in the unipolar spin diode picture (see Equ. 5.1). This corresponds to a nonlinear dependence of the domain wall resistance R_{dw} on voltage

$$R_{dw}(V) = \frac{V}{2qJ_0 sinh\left(\frac{qV}{kT}\right)}, \tag{5.7}$$
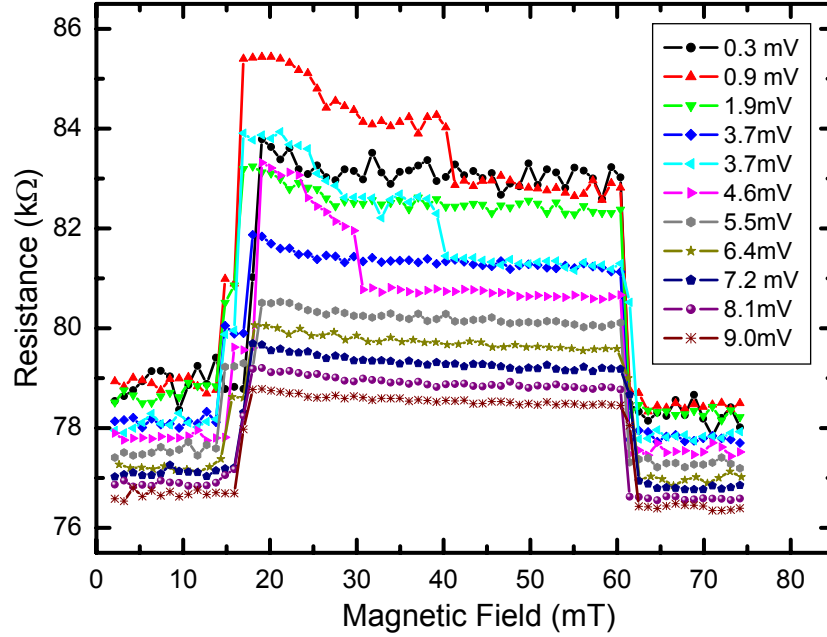
where all parameters have the same meaning as defined above.

Figure 5.13: Voltage dependence of the magnetoresistance at T=4.2K of sample 20805b-T3-3 after it was subjected to a second etching step. The four probe voltage drop was adjusted between 0.3 and 9.0 mV. This range corresponds to energies ranging from just below the thermal energy up to 25 k_BT.

In order to compare the experimental data shown in Fig. 5.13 with this model, some experimental details have to be carefully accounted for. The voltage given in the caption of Fig. 5.13 is the four probe voltage drop, i.e. the voltage drop over a small part of the outer wires, both constrictions and the inner island.

Because it is not possible to directly measure the voltage drop over the two domain walls alone, all existing series resistances must be included in a realistic model. The analysis is complicated even further by the unexpected fact that also the parallel state resistance exhibits nonlinearities which could be an indication of the onset of tunneling transport in the constrictions.

In order to model the voltage dependence of the spin valve peak, it is assumed that the four probe voltage drop V is distributed among an ohmic series resistance R_s and two identical domain walls R_{dw}. The total resistance R_t is thus

$$R_t(V) = R_s(V_s) + 2 \cdot R_{dw}(V_{dw}) = K_1 + \frac{V_{dw}}{K_2 \cdot sinh\left(\frac{V_{dw}}{2k_BT}\right)}, \qquad (5.8)$$

with the fitting parameters $K_1 = R_s$ and $K_2 = 2qJ_0A$, A being the cross section of the constriction. Because all resistances are connected in series the voltage drop is distributed according to $V = V_s + 2V_{dw}$, with V_{dw} being twice the voltage dropping over each of the identical domain walls. Another approach to modelling could have been to regard the difference in the peak to baseline resistance as the domain wall resistance and then to try and fit it with the nonlinear term alone.
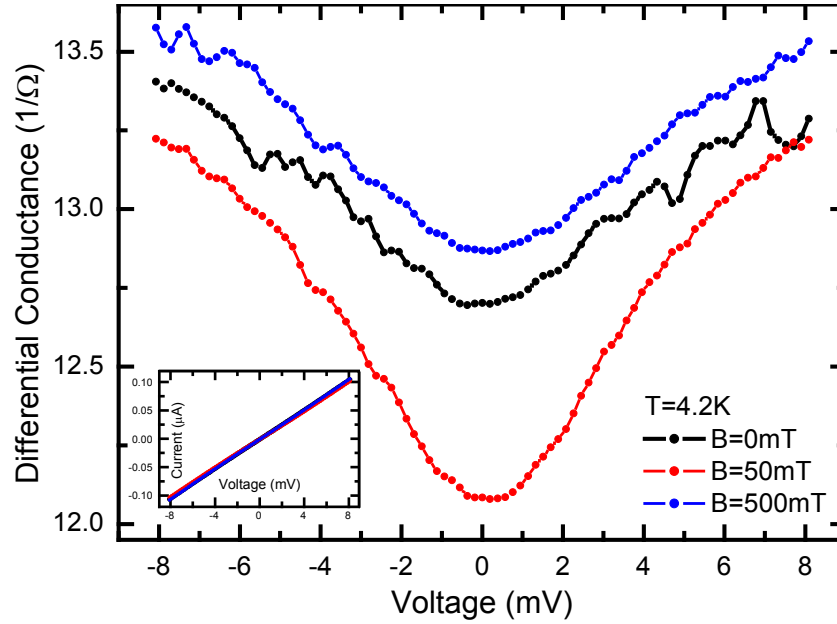
Figure 5.14: Conductance spectra of sample 20808b-T3-3 (re-etched) taken at T=4.2 K and various magnetic fields on and off the spin valve feature. The corresponding I-V data is shown in the inset.

However, the baseline resistance also exhibits a considerable nonlinearity, perhaps a sign of an onset of tunneling in some parts of the junction. This indicates that this resistance difference does not quantitatively account for the true domain wall resistance. Although the fit presented in Equ. 5.8 also not accounts for the baseline nonlinearity, it was chosen because there is better numerical agreement.

Figure 5.15 shows the result of the fit. Plotted on the y-axis is the resistance of the spin valve peak, extracted at magnetic fields just slightly lower than the switching field of the island. This avoids complications due to the fine structure present at lower magnetic fields. The experimental data (dots) and the fit to the above model (solid line) are plotted versus the voltage V_{dw} dropping over both domain walls.

The best fit has been achieved for the parameter values $K_1 \approx 68.4$ kΩ and $K_2 \approx 50.6$ nA. An analysis of the validity of the fit obviously has to rely on a check whether these values are reasonable. In the case of parameter

$$K_2 = 2qAD_p n_m / L_m \qquad (5.9)$$

this is rather difficult, because the values of hole diffusion constant D_p and minority spin diffusion length L_m are not well known in (Ga,Mn)As.

However, as will be shown later, a spin injection model for the 8% magnetoresistance in this sample is consistent with the experimental observations for a spin polarization of $\approx 30\%$ and a Fermi energy of $E_F = 90$ meV in the area of the constrictions. In a parabolic band model this value corresponds to a minority spin carrier concentration of $n_m \approx 4 \cdot 10^{19}$ cm^{-3}.
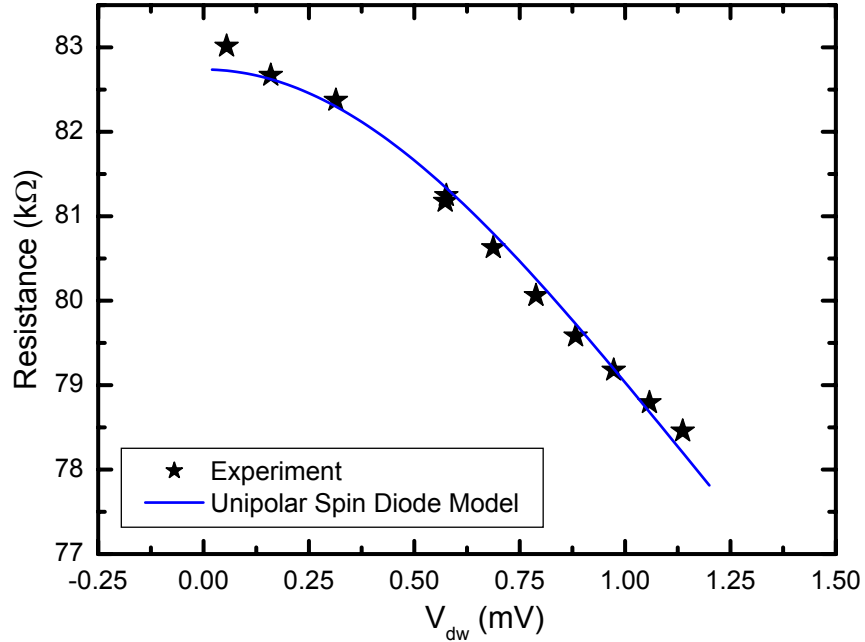
Figure 5.15: Fit of the nonlinear dependence of the size of the spin valve peak on the applied voltage. Dots: Resistance values of the spin valve peak at various voltages. Solid Line: Fit with the model described in the text.

The hole diffusion constant D_p is linked to the carrier mobility by the Einstein relation

$$D_p = \frac{kT}{e}\mu,\qquad(5.10)$$

where e is the electronic charge and μ the carrier mobility. In the Drude picture of the conductivity of a free electron gas $\mu = 1/(ep\rho)$, with the hole carrier concentration p and ρ the resistivity of the material. When assuming the measured bulk value for the sheet resistance of 4500 Ω, a Fermi energy of $E_F = 90$ meV and a parabolic band picture, one arrives at $p = 1.3 \cdot 10^{20}$ cm^{-3}, $\mu = 5.6$ cm^{2}V^{-1}s^{-1} and D_p(4.2 K)$=2.1 \cdot 10^{-3}$ cm^{2}s^{-1}.

It is instructive to compare the derived value for the mobility in (Ga,Mn)As with the well known properties of regular p-GaAs: The hole Hall mobility of p-type GaAs at $T = 300$ K decreases with increasing hole concentration while saturating at a value of $\mu_H \approx 50$ cm^{2}V^{-1}s^{-1} for $p \approx 5 \cdot 10^{19}$ cm^{-3} and above [Wil75]. The resistivity of wafer ND-20805b, which shows metallic transport behavior, is nearly constant between 4 K and 300 K and thus the mobility is nearly constant as well between these temperatures. In other words, low temperature values of the (Ga,Mn)As should not differ considerably from their room temperature values and we can compare with the data in [Wil75]. When doing so, it should be noted that due to the low temperature growth, (Ga,Mn)As has worse crystalline quality than bulk p-GaAs. Thus it is reasonable that its hole mobility is also considerably lower than for GaAs with comparable carrier concentration. The value of 5.6 cm^{2}V^{-1}s^{-1} thus seems very reasonable compared to 50 cm^{2}V^{-1}s^{-1}.

With the above values we can go back to the definition of parameter K_2 and substitute the approximate cross section of the constriction ($19 \cdot 10$ nm^2), the hole diffusion constant $D_p =$

$2.1 \cdot 10^{-3}$ cm^{2}s^{-1} and the minority spin carrier concentration of $n_m = 4 \cdot 10^{19}$ cm^{-3}. Solving for the minority spin diffusion length, this model yields a value of $L_m \approx 10$ nm. This is in very good agreement with the actual geometrical extent of the constrictions and thus also with the properties the pinned domain wall is expected to have.

Turning to the second fitting parameter, it is immediately clear that $K_1 = 68.4$ kΩ must account for all ohmic series resistances existing in the form of outer wires, inner island and also the ohmic contribution coming from the constrictions. A simple comparison with the experiment yields that in Fig. 5.15, for V=0.3 mV the calculated resistance of the two domain walls is ≈ 15 kΩ. In contrast, the height of the spin valve peak is only 4.7 kΩ which is a factor of three lower. However, as pointed out above, the latter quantity should be interpreted with caution. It is not clear that it quantitatively measures the domain wall resistance because of the existence of nonlinearities also in the baseline resistance.

In conclusion it becomes clear that although it shows good agreement with the data, the simple model presented above does not capture all occurring phenomena. This is partly due to the fact that in this geometry only a convolution of all simultaneous effects is measured. Any further refinement of the fitting model would inevitably lead to additional more or less freely adjustable parameters and is thus not promising in terms of getting a better grip on the physics involved in this measurement.

5.10.2   Magnetoresistance of Outer Wires Without Constrictions

In order to unambiguously demonstrate that domain wall related effects are the cause of the spin valve like magnetoresistance features presented above, control samples without constrictions have been fabricated and measured. The basic design is identical to what is shown in Fig. 5.5, except for the fact that constrictions and the island structure are replaced by a continuous piece of 400 nm wide wire. The resulting nanowire is then measured in the same way as the double constriction samples. The magnetic field is also applied in the plane of the thin film and points along the wire axis.

Figure 5.16a presents a typical magnetoresistance measurement on a 400 nm wide wire without constrictions patterned from wafer ND-20805b. For comparison, 5.16b displays the spin valve like magnetoresistance measurement on the double constriction sample ND-20805b-T3-3 (as fabricated). The wire magnetoresistance is flat except for a single 0.35% positive bulk-like AMR feature at ≈ 16 mT. The spin valve feature is not observed.

A comparison of Figs. 5.16a and b clearly shows that in both samples the switching of the wide wires coincides. A consistent explanation is that although the sample design is different, the switching of the 400 nm wide wire in both cases occurs due to the same mechanism, namely domain walls sweeping in from the electrical contact pads. Consequently this is evidence for the existence of an antiparallel magnetization alignment in the double constriction sample. Domain walls are indeed pinned in the constrictions and they are the cause of the observed spin valve feature.
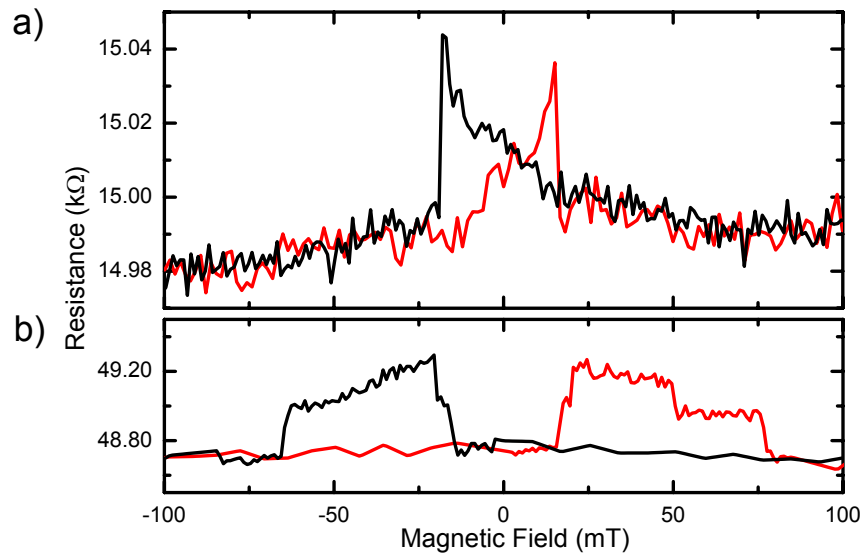
Figure 5.16: (a) Magnetoresistance measurement on a 400 *nm* wide wire patterned from wafer ND-20805b. (b) Magnetoresistance measurement on sample ND-20805b-T3-3 as fabricated. The wire shows a single switching feature due to AMR. It coincides with the first switching event in the constriction sample. This is evidence that in both cases the magnetization reversal is dominated by domain walls sweeping in from the electrical contact pads.

5.10.3 Domain Wall Resistance in the Tunneling Regime

20805b-T3-3 Re-etched Twice

When the constrictions are etched even further, a very strong increase in resistance and magnetoresistance is observed. Magnetoresistance curves of sample ND-20805b-T3-3 after a second re-etch are plotted in Fig. 5.17. The additional etching has increased the sample resistance dramatically.

Current voltage characteristics (inset) are strongly nonlinear, indicating the existence of tunnel barriers in the constrictions. The high resistance of the sample limits the range of meaningful measurements to excitation voltages above 100 mV.

Nevertheless, as shown in Fig. 5.17a and b, even at bias voltages that are two orders of magnitude higher than the thermal energy, the sample still exhibits a large spin valve-like magnetoresistance ($MR > 40\%$ for $V = 120$ mV). The switching fields are consistent with the previous results. This suggests a giant increase in the magnetoresistance of tunneling-type constrictions compared to samples that are in the regime of diffusive transport. The amplitude of the magnetoresistance increases with decreasing voltage. However, detailed studies of the voltage dependence were not attempted due to the large resistance and poor signal to noise ratio associated with the sample.

The existence of a giant magnetoresistance in tunneling samples is confirmed by the measurement of 2000% positive magnetoresistance displayed in Fig. 5.18. The measurement was obtained on the sample ND-20805b-T3-2 at $T = 4.2$ K using an excitation voltage of 0.4 mV. This sample is nominally identical to ND-20805b-T3-3. Its high field resistance correspond-
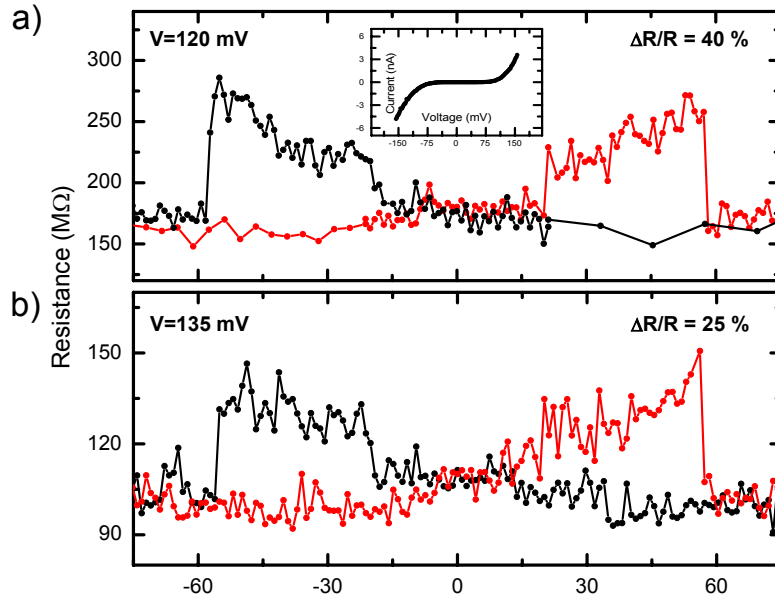
Figure 5.17: (a) 40% positive magnetoresistance of sample ND-20805b-T3-3 after a second re-etch, measured at $T = 4.2$ K, $V = 120$ mV. Inset: Strongly nonlinear current voltage characteristics. (b) 25% positive magnetoresistance $T = 4.2$ K, $V = 135$ mV.

ing to the parallel magnetization state is 4 MΩ. The resistance of the sample is completely dominated by the constrictions.

In addition the current voltage characteristics of the device are strongly nonlinear with a roughly quadratic dependence of the conductance on bias (inset of Fig. 5.18) that is consistent with tunneling transport [Bri70].

In contrast with the results in the diffusive transport regime and consistent with the tunneling results in Fig. 5.17, a hysteretic signal around zero magnetic field is now observed in addition to the spin valve feature. This observation is also consistent with the presence of tunnel barriers in that these cause a magnetic decoupling of the island and the wires.

The suggested explanation is that in Figs. 5.17 and 5.18 the magnetization of the island no longer switches by the introduction of a domain wall through a constriction but rather by magnetic rotation, which explains the magnetoresistance at low fields. It is not yet entirely clear whether in (Ga,Mn)As the real easy axis is exactly parallel to the [100] crystal direction. Thus it is possible that the transport structure is not perfectly aligned along a magnetic easy axis, even when neglecting small alignment errors coming from lithography.

Thus, at zero magnetic field, the wide wires will be magnetized along the crystalline magnetic easy axis, which is slightly off the geometric wire axis. The narrow island on the other hand, which is fully dominated by its higher shape anisotropy, will be magnetized along its geometric axis. Because of this the relative alignment is not fully parallel at zero field. The continuous relaxation of the magnetization of the outer wires towards the crystalline easy axis shows up as the continuous change in resistance at low fields. In wider constrictions the magnetic coupling prevents this effect and the continuous feature is missing.
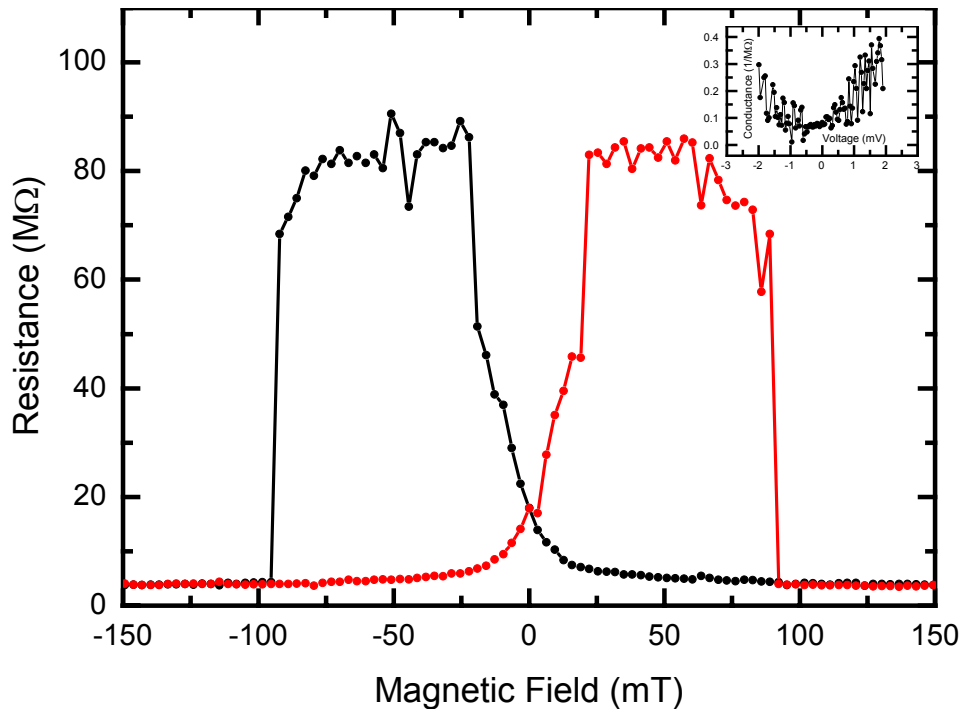
Figure 5.18: 2000% positive magnetoresistance in a sample with tunnel barriers at the constrictions. Inset: Nonlinear conductance spectrum of the sample.

5.11   Modelling of the Magnetoresistance

5.11.1   Low Resistance Regime

The above observations can be understood in a unified manner by assuming that etching causes a gradual depletion of the carrier density at the constrictions.

Dry etching is a process in which the semiconductor material is sputtered by collisions of particles. It is well known that due to the physical and chemical reactions taking place at the surface, a damaged layer is formed and the etched surface contains a large number of defects. These defects can be charged, and the large number of charged impurities induces sidewall depletion of the interior of the semiconductor. Because of a large surface to volume ratio, this mechanism will clearly be most effective at the narrowest parts of the structure, i.e. at the constrictions.

In the numerical estimates below it is assumed for simplicity that both constrictions have equal resistance. It should be noted that deviations from this assumption have only minor effects on the drawn conclusions.

As a first order approximation, it is assumed that the domain wall resistance is given by the expression of Valet and Fert for the spin-accumulation-induced resistance at an abrupt junction between two regions of opposite magnetization [Val93]. This model is described in some detail in section 2.4.3. It is the most widely used model for the analysis of the giant magnetoresistance effect in the current perpendicular to plane geometry.

The model takes into account spin accumulation and spin relaxation effects as the main

origin of magnetoresistance in this geometry. The physical interpretation is that a spin accumulation effect which extends over a length scale of the spin diffusion length on both sides of the interface increases the electric field, thus adding an additional resistance per unit area ΔR. In the simplest case, the interface between the magnetic domains itself is supposed to have zero resistance and no effect on the spin polarization of the incoming carriers. In our samples, the pinned domain wall plays the role of the interface and it must be sufficiently sharp to fulfill the above conditions.

If this is the case, the additional resistance per unit area due to the spin accumulation equals

$$\Delta R \approx 2\beta^2 \rho^* \ell, \tag{5.11}$$

where ρ^* is the bulk resistivity in the parallel magnetization state, ℓ is the length of the constriction and β is the spin polarization at the point of injection into the constriction/domain wall. This spin polarization of the current is readily determined by imagining the constriction as a point contact and expressing the incoming spin currents by means of the hole density of states at the Fermi energy $N_{\uparrow,\downarrow}(E_F)$ times the Fermi velocity $v_{F\uparrow,\downarrow}$, i.e.[2]

$$\beta = \frac{N_\uparrow(E_F)v_{F\uparrow} - N_\downarrow(E_F)v_{F\downarrow}}{N_\uparrow(E_F)v_{F\uparrow} + N_\downarrow(E_F)v_{F\downarrow}}. \tag{5.12}$$

In a parabolic band model, the three-dimensional density of states at the Fermi energy $N_{\uparrow,\downarrow}(E_F)$ and the Fermi velocities $v_{F\uparrow,\downarrow}$ are proportional to k_F (the arrows refer to the spin subbands). Thus we can write

$$\beta = \frac{E_{F\uparrow} - E_{F\downarrow}}{E_{F\uparrow} + E_{F\downarrow}}. \tag{5.13}$$

From Equ. 5.13 one can see the evolution of the resistance and magnetoresistance with etching. As pointed out above, etching depletes the (Ga,Mn)As, so that $E_{F\uparrow}$ and $E_{F\downarrow}$ are reduced, but the exchange splitting $\Delta E = E_{F\uparrow} - E_{F\downarrow}$ remains roughly unaffected.

Hence the numerator of Equ. 5.13 does not change, but the denominator gets smaller and the polarization increases. This expression for the polarization is now inserted into the Valet-Fert expression (Equ. 5.11) for the magnetoresistance.

As pointed out above, when inserting the resistance of the constrictions one has to keep in mind that ≈ 40 kΩ have to be subtracted from the four probe device resistance. A reasonable value for the exchange splitting is $\Delta E \approx 30$ meV [Szc99a], confirmed by unpublished results by G. Astakhov. With the above values, the magnetoresistance data in Fig. 5.8 is reproduced using the Fermi energy of 150 meV for the unetched sample, while the data in Fig. 5.12 implies that the etching reduced the Fermi energy to about 90 meV.

These values seem quite reasonable, but should, given the many uncertainties and approximations involved, only serve as a rough indication of what may be going on in the sample. Note that the spin polarization of some 20% obtained from these numbers is only a lower limit estimate of the bulk value: it is known that the transport mean free path l_t of the holes is shorter than the dimensions of the constriction, so it can be assumed that substantial spin relaxation is taking place.

---

[2]Equ. 5.12 assumes ballistic transport across the DW; in the diffusive regime one has $\beta = (E_{F\uparrow}v_{F\uparrow} - E_{F\downarrow}v_{F\downarrow})/(E_{F\uparrow}v_{F\uparrow} + E_{F\downarrow}v_{F\downarrow})$.

5.11.2   Tunneling Transport Regime

We now turn to the giant magnetoresistance data in Fig. 5.18, where the constrictions clearly are in the tunneling regime. It is tempting to try to model the observed MR in terms of Julliere's tunnel magnetoresistance model (TMR) model [Jul75]. Within this model the TMR ratio is given by

$$TMR = \frac{R_{AP} - R_P}{R_P} = \frac{2P_1 P_2}{1 - P_1 P_2}, \tag{5.14}$$

where P_1 and P_2 are the spin polarizations of the two ferromagnets. In order to explain a 2000% MR signal, the Julliere model requires a spin polarization of the contacts of ca. 95%, much larger than the values found above. This large discrepancy suggests that the model in [Jul75] is not applicable here and therefore a different approach to modelling the tunneling regime must be adopted.
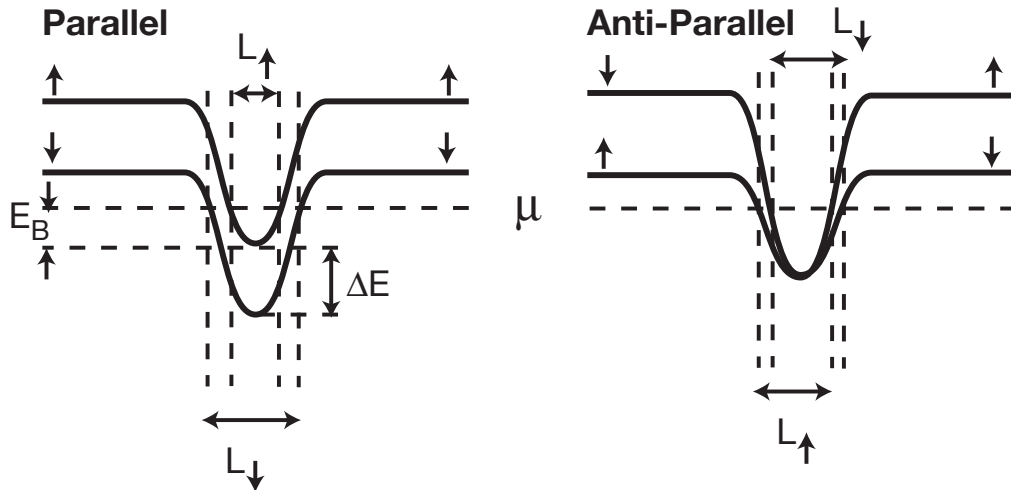

Figure 5.19: Tunneling model for the large magnetoresistance observed in the high resistance samples: Depletion due to dry etching causes the formation of parabolic barriers in the constriction region.

It is assumed that depletion due to dry etching causes the formation of shallow parabolic barriers in the constriction between the two (Ga,Mn)As regions. The resulting band alignment is sketched in Fig. 5.19. The barrier height for the majority-spin holes above the chemical potential μ is defined as E_B.

If the barrier is very thin, such that the hole wave functions can penetrate into the barrier region and continue to couple the Mn spins, then it is reasonable to assume that the spin splitting ΔE in the barrier region is the same as in the bulk. This assumption may seem a bit unrealistic and it is not clear whether carrier mediated ferromagnetism really exists all the way through the barrier, a region that is forbidden for carriers. However, the spin splitting will remain approximately the same at least up to the point where the spin-split valence band levels fall beneath the chemical potential, which is sufficiently long in order for the model to be applicable.

For parallel magnetization alignment this results in a barrier for minority-spin holes that is higher ($E_B + \Delta E$) than for majority-spin holes (E_B). As a consequence of the non-abrupt barrier,

the thickness of the barrier for minority-spin holes, $L_{P\downarrow}$, will be greater than that for majority spin holes, $L_{P\uparrow}$.

In the antiparallel situation depicted on the right, however, the barriers for the two spin channels are the same at approximately $E_B + \Delta E/2$, and their thicknesses are also the same, $L_A \approx (L_{P\uparrow} + L_{P\downarrow})/2$. The transmission probability $\mathscr{T}$ through a parabolic barrier is [Sze81]

$$\mathscr{T} = \exp\left(\frac{-\pi m^{*(1/2)}E_H^{(1/2)}L}{2^{(3/2)}\hbar}\right) \tag{5.15}$$

where E_H and L are the height and thickness of the barriers respectively, and $\hbar$ is the reduced Planck constant. With $m^* \approx 0.5 m_e$, we have $\mathscr{T} = \exp\left(-3.0 E_H^{(1/2)}L\right)$, where E_H is in eV and L in nm.

We now estimate the values of the parameters required to match the experiment. Assuming that the parabolic shape of the barrier is the same for all situations, there is a uniform relationship between L and E_H of the form $L = (\alpha E_H)^{(1/2)}$, where α is constant. This implies that $\mathscr{T} = \exp\left(-3.0\alpha^{(1/2)}E_H\right)$. From the experiment we have $\mathscr{T}_{P\uparrow}/\mathscr{T}_A = 20$, and so we choose α to satisfy this. With $\Delta E = 30$ meV, this yields $\alpha = 4400$ eV^{-2}, independently of the barrier height for majority spin holes E_B. We can estimate $E_B \approx 31$ meV from the resistance of the constrictions. Just as a gauge, the thicknesses of the barriers are then 11.7 nm for the parallel majority case, 14.3 nm for the antiparallel case, and 16.4 nm for the parallel minority case. These numbers all seem reasonable.

A key element of this analysis is that the minority and majority carriers deplete at different positions in the constriction. Depletion at the edge of a (Ga,Mn)As film differs considerably from depletion in the bulk, since Mn spins at the edge remain coupled through the remaining holes to Mn spins which lie effectively within the bulk. The presence of these nearby bulk-like oriented Mn spins produces, through the mediating holes, a large exchange field on the Mn spins at the edge. This in turn induces them to order at local hole concentrations which, in the bulk, would otherwise not lead to ferromagnetism. Hence we argue that magnetically ordered Mn spins, producing an exchange splitting for the holes similar to that in bulk, are present at the edges of the sample where the local hole concentrations is much lower than the bulk.

5.12   Summary

In this chapter, the magnetoresistance of nanosized double constrictions in (Ga,Mn)As has been investigated. The sample layout was carefully optimized to be able to unambiguously measure domain wall related effects. As a result, shape anisotropy controlled switching and trapping of domain walls inside the constrictions was clearly demonstrated. In the range of investigated samples, both the diffusive and the tunneling regime were observed. Samples in all cases show clear spin valve like magnetoresistance with up to 8% positive MR in the diffusive regime and 2000% positive MR in the tunneling magnetoresistance. An intuitive modelling was thus applied and consistently explains the observations in terms of spin injection and spin-dependent tunneling mechanisms.

Chapter 6

Tunneling Anisotropic Magnetoresistance (TAMR)

6.1 Introduction

Devices relying on spin manipulation are hoped to provide low-dissipative alternatives for microelectronics. Especially in the field of non-volatile information storage, attractive prospects are opened. One scheme that has received a lot of interest in this respect is the magnetic tunnel junction.

Conventional magnetic tunnel junctions are multilayers of two ferromagnetic metal layers separated by a thin insulating layer which acts as a tunnel barrier. A current is passed perpendicular to the layers of the magnetic tunnel junction sandwich and its resistance is measured. As described in section 2.5.1, the resistance of the multilayer is low when the magnetic layers are aligned parallel to one another, and it is high when antiparallel. This difference gives rise to the tunneling magnetoresistance (TMR) effect that was already discovered in the 1970s [Jul75]. The working principle relies on different magnetic coercivities in the layers to obtain parallel and anti-parallel alignment of the magnetic layers.

Although magnetic tunnel junctions have a history dating back more than 20 years (refer to section 2.5.1), only small MR effects were observed until well into the 1990s. Magnetic tunnel junctions showed little more than 10% TMR at room temperature [Moo95] in 1995, but since then, many academic and industry based research groups have been continually and dramatically improving this value as shown in Fig. 6.1a. Nowadays the highest achieved room temperature TMR ratios exceed 200% already [Par04, Yua04]. This performance is unsurpassed by any other source of magnetoresistance, thereby making magnetic tunnel junctions prime candidates for inclusion into next generation commercial field sensors and magnetic random access memory (MRAM). Prototypes of high capacity MRAM memory modules were already demonstrated by Infineon and have a good chance to enter mass production some time in the near future. They are based on the very simple information storage and large scale integration principles that are shown in Fig. 6.1b and c. MRAM has the potential to be as fast as conventional RAM while at the same time featuring non-volatility and extremely high durability. A successful commercial implementation would pave the way for the realization of instant on-and-off computers, a potential multi-billion dollar market.

The emerging field of semiconductor spintronics is hoped to provide magnetoresistive de-
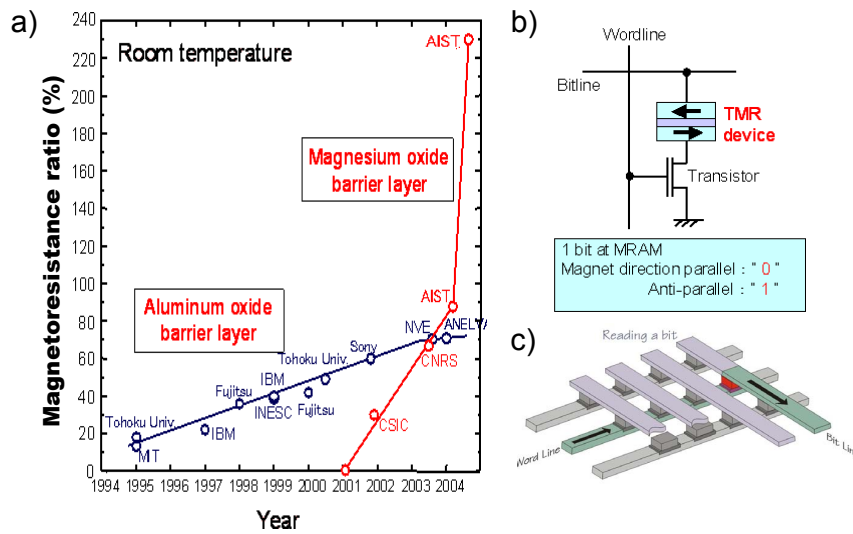
Figure 6.1: a) History of improvements of the MR ratio in TMR devices. b) Single bit storage principle of magnetic random access memory (MRAM) based on a magnetic tunnel junction. Pictures copyright National Institute of Advanced Industrial Science and Technology (AIST). c) Large scale integration scheme for MRAM. Picture copyright IBM and Infineon MRAM research alliance.

vices with similar behavior as current metal-based spin-valves, while at the same time providing novel features unattainable in metals. An oft proposed device scheme consists of a tunnel barrier between two ferromagnetic semiconductors. As such, (Ga,Mn)As/(Al,Ga)As/(Ga,Mn)As structures have previously been studied [Hig01, Chi04] with some promising results. However, realizing the full potential of these systems will require a full understanding of the physics of tunneling into (Ga,Mn)As. The experiments presented in this section will shed some light on this topic and thereby demonstrate that the dominant tunneling effects are rather different than previously thought.

Above everything else, this is exemplified by the surprising result that it is possible to measure a spin valve like effect using a single layer of ferromagnetic (Ga,Mn)As. The effect results from strong spin-orbit coupling within a single ferromagnetic layer rather than from injection and detection of a spin-polarized current by two coupled ferromagnets. This is a novel kind of behavior that establishes a whole new class of spintronics devices with unprecedented properties. The novel effect is named tunneling anisotropic magnetoresistance (TAMR). It is caused by the interplay of the anisotropic density of states in (Ga,Mn)As with respect to the magnetization direction, and a two-step domain wall induced magnetization reversal process in this material.

In the following section, the rich experimental observations on a Au/AlOx/GaMnAs tunnel junction will be comprehensively explained using TAMR. This involves first the separate understanding of the unique magnetic and tunneling transport anisotropies occurring in the ferromagnetic layer. The TAMR picture, based on a constructive interplay of these anisotropies within that layer, can explain practically all observed phenomena in an intuitive way.

The occurrence of TAMR, however, is not limited to structures containing a single magnetic

layer. This will be shown in chapter 7, where results on a GaMnAs/i-GaAs/GaMnAs tunnel junction are presented. It will be shown that also the behavior in this TMR-like geometry can be explained in the TAMR picture. In addition, the low temperature results (T=1.7 K) from this magnetic tunnel junction features an enormous amplification of the effect. Possible reasons for this amplification are discussed by invoking the importance of additional many-particle transport effects at these temperatures.

6.2 Sample Details

6.2.1 Bulk Material Properties

The magnetic layer in our sample is a 70 nm thick epitaxial (Ga,Mn)As film grown by low temperature (270 °C) molecular beam epitaxy onto a GaAs (001) substrate[1] and a special buffer layer. The buffer is a bilayer, with the first buffer layer consisting of $\approx$300 nm high temperature GaAs and the second layer being a very thin ($\approx$2 nm) film of low temperature GaAs. The material was grown by G. Schott, the wafer serial number is S20. High resolution x-ray diffraction showed that the sample had high crystalline quality comparable to that of the substrate. From the measured lattice constant and the calibration curves of [Sch03], the Mn concentration in the ferromagnetic layer is roughly 6%. Etch capacitance-voltage control measurements yielded a hole density estimate of $\approx 10^{21}$ cm^{-3}, corresponding to more than 70% of the incorporated Mn being electrically activated, i.e. contributing one hole carrier to the valence band. This high activation ratio shows that the as grown sample is of a very high quality, as in (Ga,Mn)As all important crystalline defects reduce this value [Yu02].

Figure 6.2a is a measurement of the remanent magnetic moment of the as grown layer after the sample was cooled in zero field from room temperature. The sample was magnetized at low temperatures along the [100] magnetic easy axis. The applied magnetic field was then brought back to zero and the magnetic moment was measured during heating. From this measurement one can see that the Curie temperature is about 70 K. No significant magnetic moment is present above the Curie transition temperature. This shows that there are no noticeable ferromagnetic inclusions present in the sample, a further characteristic of a high quality (Ga,Mn)As random alloy. Figure 6.2b shows a SQUID hysteresis measurement with the magnetic field along the [100] crystal direction. The hysteresis loop is almost perfectly square, indicating that the [100] direction is a magnetic easy axis of the layer. A similar measurement shows that [010] is also magnetically easy. Note that although thermal annealing of (Ga,Mn)As can improve the magnetic and electrical properties of a layer, samples intended for transport measurements are intentionally used in an as grown condition in order to improve reproducibility and avoid potential problems coming from outdiffused Mn compounds on the surface (see section 3.4).

6.2.2 Sample Layout and Fabrication

After growth, the sample surface was Ar sputtered to remove any potential oxides. A 1.4 nm thick polycrystalline Al layer was then deposited at a rate of 0.4 Å/sec and a base pressure of 2×10^{-6} mbar using Ar sputtering. The Al layer was oxidized in-situ using 100 mbar of pure

---

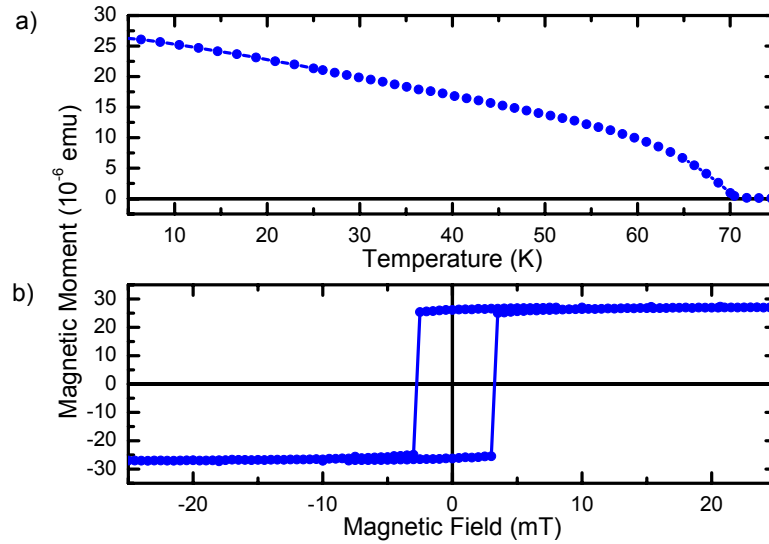[1]For a discussion of (Ga,Mn)As growth, see, e.g. [She97, Cam03].

Figure 6.2: Bulk magnetic properties of wafer S20. a) Measurement of the Curie temperature. $T_c \approx 70K$, indicating high quality bulk material. b) Square hysteresis with the magnetic field along the [100] crystal direction confirms this direction to be a magnetic easy axis of the thin film.

oxygen for 8 hours, producing a closed AlOx layer and thereby forming a tunnel barrier. An electrical contact was then fashioned onto the structure by evaporating 5 nm of Ti as a sticking layer followed by 300 nm of Au. The resulting layer stack is shown in Fig. 6.3a.

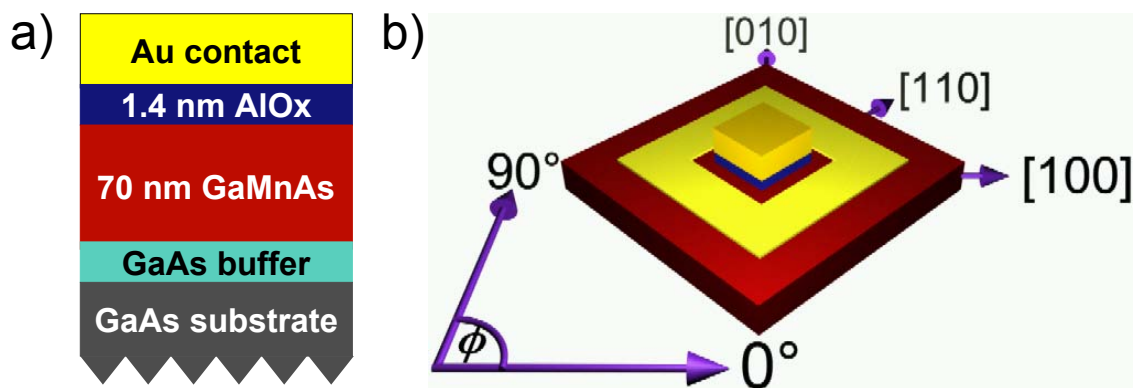Figure 6.3: a) Layer stack used to fabricate Au/AlOx/GaMnAs tunnel junctions. b) Sample layout of a Au/AlOx/GaMnAs tunnel junction. The angle ϕ of applied in-plane magnetic fields is related to the crystal directions in the thin film.

Standard optical lithography and chemically assisted ion beam etching (CAIBE) were then used to pattern the device as shown in Fig. 6.3b. In the first step, material is etched away, leaving

only the central 100 x 100 μm^2 square pillar consisting of the metal contact on a tunnel barrier. The surrounding W sticking layer and Au contact are then deposited onto the (Ga,Mn)As surface, providing a back contact. The resulting sample is then fixed inside a nonmagnetic chip carrier and each of the two electrodes is ultrasonically bonded to the chip carrier with two gold wires. This allows for quasi four probe electrical measurements of the sample, excluding the cryostat wiring. The resulting device allows electrical transport measurements with the probing current running vertically through the whole layer stack.

6.3 Measurement Details

The sample was inserted into a magnetocryostat allowing for the application of magnetic fields of up to 300 mT in any direction[2]. Magnetic fields in the plane of the layer are denoted by the angle ϕ with respect to the [100] crystal direction, as indicated in Fig. 6.3b. Two different types of **H** scans will be presented: MR-scans, which consist of saturating the sample magnetization in a negative magnetic field along a given direction and then measuring the resistance of the device as $|\mathbf{H}|$ is swept to positive saturation and back again; and ϕ-scans, where the resistance is measured for constant $|\mathbf{H}|$ while sweeping ϕ.

6.4 Magnetoresistance Properties

6.4.1 Properties at T=4.2 K

Figure 6.4 presents three magnetoresistance curves measured on a sample with the serial number Au/AlOx/GaMnAs-1, in the following also named "single sided spin valve". The data was acquired at 4.2 K with 1 mV bias by sweeping the magnetic field along the 0°, 50°, and 55° directions. For each curve, the magnetic field was swept from negative to positive saturation of the magnetization and back. However, the plot focuses on the interesting low field region between -30 mT and +30 mT. In all cases the magnetoresistance shows spin valve-like behavior with an amplitude of $\approx$3%. The feature is delimited by two sharp switching events, labeled H_{c1} and H_{c2} in the figure, between which the resistance of the sample is different from its value outside these events. In all three measurements, the sample only has two distinct resistance states: a low one of $\approx$2920 Ω and a high one of $\approx$3000 Ω. Outside the low field region, there are no additional sharp switching events, only a continuous change of resistance consistent with a Stoner-Wohlfahrt-like rotation of the magnetization direction.

The (Ga,Mn)As resistivity is $1.1 \cdot 10^{-3}$ Ωcm, typical for high quality material [Edm02], and corresponding to a resistance of $\approx$10 Ω between the central pillar and the backside contact. This was confirmed by measuring the resistance through similar pillars without a tunnel barrier. This resistance is over two orders of magnitude lower than that of the total device, rendering any bulk magnetoresistance of the (Ga,Mn)As negligible and indicating that the observed magnetoresistance effects are indeed due to the existence of the tunnel barrier. Furthermore, test structures without a tunnel barrier do not show any features in MR. Additionally, as demonstrated in Fig. 6.5, the I-V characteristics of the sample are clearly nonlinear and consistent

---

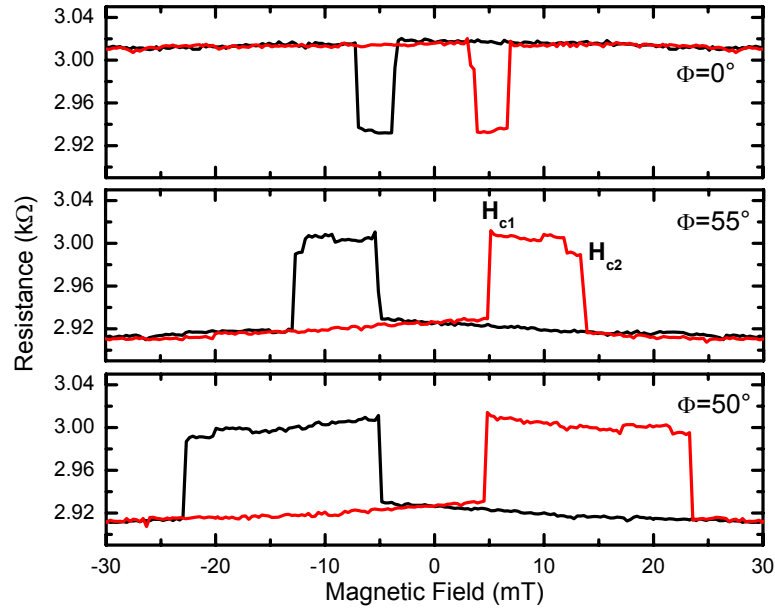[2]The details of this cryostat and magnet system are given in chapter 4.

Figure 6.4: Hysteretic magnetoresistance curves acquired at 4.2 K with 1 mV bias by sweeping the magnetic field along the 0°, 50°, and 55° directions. Spin valve like features of varying widths and signs are clearly visible, delimited by two switching events labeled H_{c1} and H_{c2}. The magnetoresistance is independent of bias direction.

with tunneling transport.

The three magnetoresistance curves in Fig. 6.4 were specifically chosen because they clearly demonstrate that the width of the TAMR feature and, perhaps even more importantly, its sign depends on the magnetic field angle ϕ. In order to analyze the exact angular dependence of the spin valve-like feature it is useful to plot the magnetoresistance data in the form of a so-called waterfall plot, as in Fig. 6.6. The graph contains 4.2 K magnetoresistance curves with the magnetic field angle ϕ ranging from 0° to 170° in steps of 10°. For better clarity, the curves are offset vertically and only sweeps towards the negative field direction are shown. The part of the data that is not shown in the graph (180° to 350°) does not contain any additional information, as it is hysteretically symmetric.

The waterfall plot reveals that the width and also the sign of the spin valve-like feature follow a very regular pattern with respect to the magnetic field angle ϕ. At 0°, which is close to the [100] crystal direction, the feature is narrow and negative. Its width increases with increasing angle until $\phi = 45°$. At this angle the sign of the feature changes from negative to positive and its width starts decreasing. In an angular interval around 90°, which corresponds to the [010] crystal direction, no spin valve signal is visible. The feature reappears in the 110° curve and its width subsequently increases until the feature changes sign again at 135°.

Yet another way to plot the magnetoresistance data is displayed in Fig. 6.7. This polar plot gives an even more comprehensive overview than the waterfall plot. It was compiled using data from all available magnetoresistance curves at 4.2 K. The dots indicate the switching events H_{c1} (red) and H_{c2} (black) that are extracted from individual magnetoresistance curves. Their distance from the origin corresponds to the field position of the switching event and they are
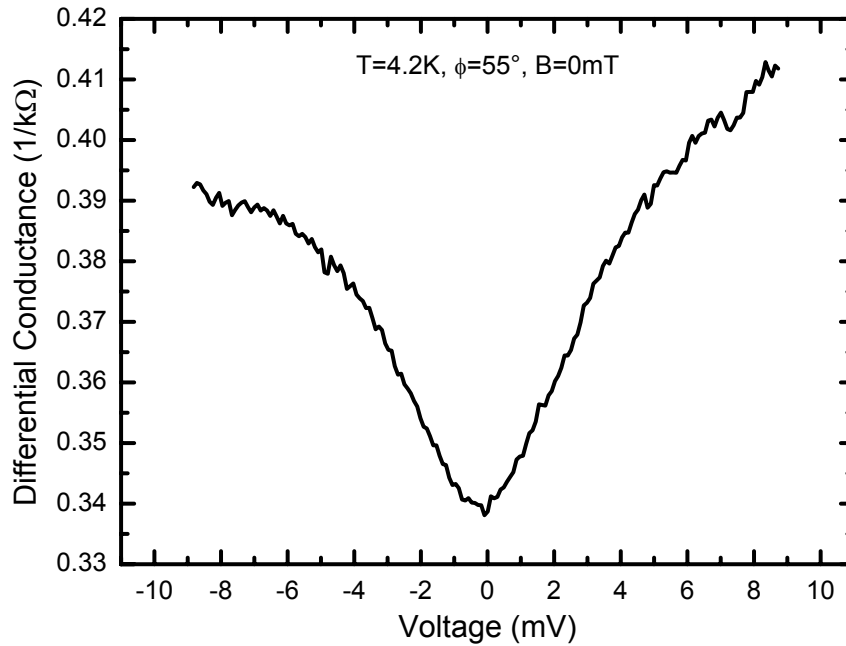
Figure 6.5: Measurement of the differential conductance of the single sided spin valve. The nonlinear behavior is consistent with tunneling transport.

plotted at the angle of the corresponding magnetoresistance measurement. The angular dependence of both H_{c1} and H_{c2} is highly symmetric. Magnetoresistance measurements correspond to radial lines starting in the center of this graph. Although the resistance data is not given by the graph, the occurrence of the two resistance states is also given in the picture: the shaded areas are regions where the sample is in a high resistance state. From this one can see the change of sign of the spin valve signal as a function of angle.

From Fig. 6.7 it becomes clear that the sample behavior changes every 90°: Two switching events are present in the transport data when the magnetic field is applied around the [100] (or [[$\bar{1}$00]]) direction, none are visible in transport when the field is applied around the [010] (or [[0$\bar{1}$0]]) axis. In a ≈90° wide interval around the [010]/[[0$\bar{1}$0]] axis, the spin valve feature is positive. In a similarly sized interval around the [100]/[[$\bar{1}$00]] axis, there is an inverted spin valve signal. Consequently, both the magnetic as well as the electric sample properties are anisotropic with respect to the direction of the sample magnetization.

6.4.2 Temperature Dependence of the Magnetoresistance

The temperature dependence of the magnetoresistance is displayed in Fig. 6.8 using data taken at ϕ=30°. The curves are offset vertically for better clarity. The size of the TAMR feature decreases with increasing temperature from about 6% at T=1.6 K to about 0.6% at 20 K. For higher temperature it becomes increasingly difficult to clearly identify the switching events at all angles and the TAMR signal disappears altogether by ≈30 K.

In addition to the decreasing amplitude of the TAMR feature with increasing temperature, there is also a change of sign between 15 K and 20 K. Although the angle of the measurement
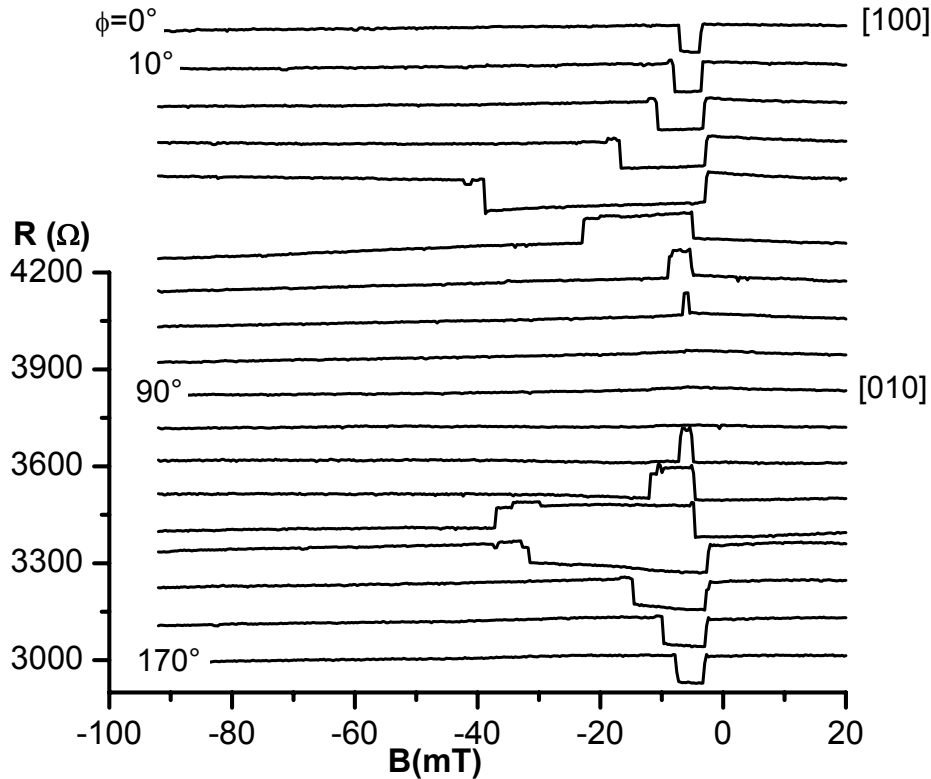
Figure 6.6: Magnetoresistance curves at various magnetic field angles. The width and the sign of the spin valve-like feature follow a regular pattern with respect to the magnetic field angle ϕ. For better clarity, the curves are offset vertically and only half-hysteresis loops are shown.

remains constant, the feature turns from negative to positive. This behavior is not unique to the $\phi = 30°$ curve shown in the figure, but in fact is observed at all angles. At T=20 K the whole polar plot has changed signs, i.e. the shaded areas in 6.7 correspond to the sample being in the low resistance state. The underlying symmetry of the polar plot, however, remains unaffected by a change of temperature.

6.5   Resistance Anisotropy at 0 mT

As pointed out above, it is known from SQUID measurements that [100] and [010] are magnetic easy axes in that at zero external magnetic field, the magnetization prefers to lie along either one of these directions. This knowledge of the magnetic anisotropy is very useful in order to relate the resistance of the sample with the orientation of the magnetization. It is also known from SQUID measurements that at high in plane magnetic fields ($\approx$300 mT) along any angle ϕ the magnetization points along the external field. When the magnetic field is subsequently lowered down to zero, the magnetization gradually rotates away from the field direction and settles along the closest magnetic easy axis. Thus, after this experimental procedure, the magnetic state of the sample is well known.

This knowledge enables us to conduct the experiment shown in Fig. 6.9. The data plotted is
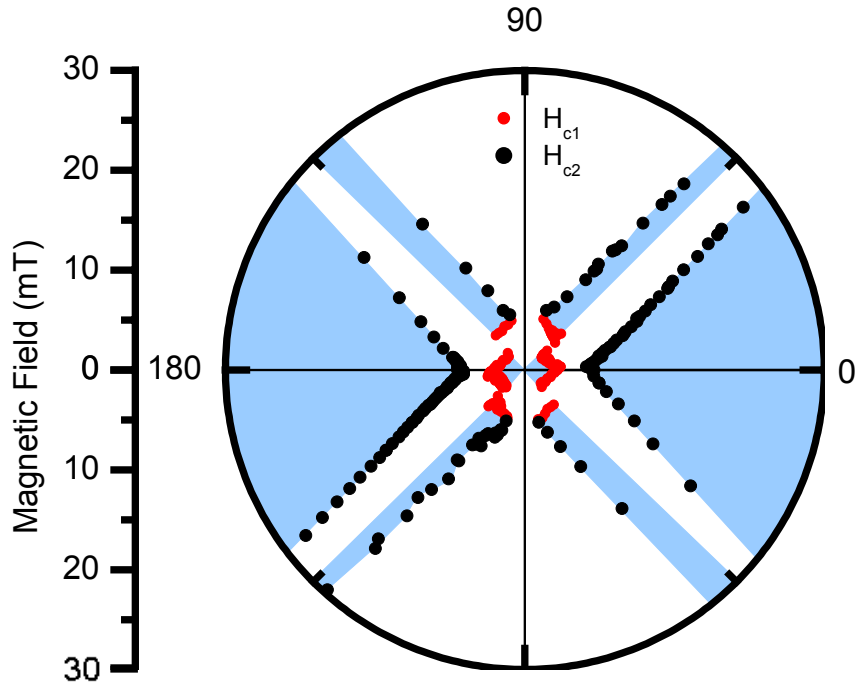
Figure 6.7: Polar plot compiled from individual magnetoresistance curves. The dots indicate the switching events H_{c1} (red) and H_{c2} (black) from individual magnetoresistance curves. The shaded areas are regions where the sample is in a high resistance state.

the sample resistance at H=0 mT measured after saturating **M** along an angle ϕ. Thus, at zero field **M** always lies along one of the fourfold easy axes. The figure unambiguously shows that **M** along [010] or [0$\bar{1}$0] corresponds to the low resistance state (2920 Ω) and **M** along [100] or [$\bar{1}$00] corresponds to the high resistance state (3000 Ω) of the sample. The resistance of the sample is anisotropic with respect to the direction of the magnetization.

6.6   Double Step Switching

With the results of the previous section we are one step closer to explaining the origin of the spin valve-like features in the magnetoresistance data. The spin valve feature must be due to a switching of the magnetization between the biaxial easy axes [100] and [010]. For example, for a positive feature the magnetization reversal could take place via the two subsequent 90° steps [010]→[100]→[0$\bar{1}$0] (Fig. 6.10a), whereas for an inverted feature an appropriate sequence would be [100]→[010]→[$\bar{1}$00]. The same line of thought can be applied to curves without a spin valve feature, where the sample remains in the low resistance state all the time. In this case the explanation is that the magnetization remains parallel to the [010] or [0$\bar{1}$0] axis all the time, the switching happening via a single 180° step (Fig. 6.10b).

   The assumption of the double step switching is confirmed by a direct observation of the magnetization reversal in SQUID. The SQUID data shown in Fig. 6.11 was measured on a piece of epilayer S20 covered with AlOx and Au overlayers. The layer structure of this sample
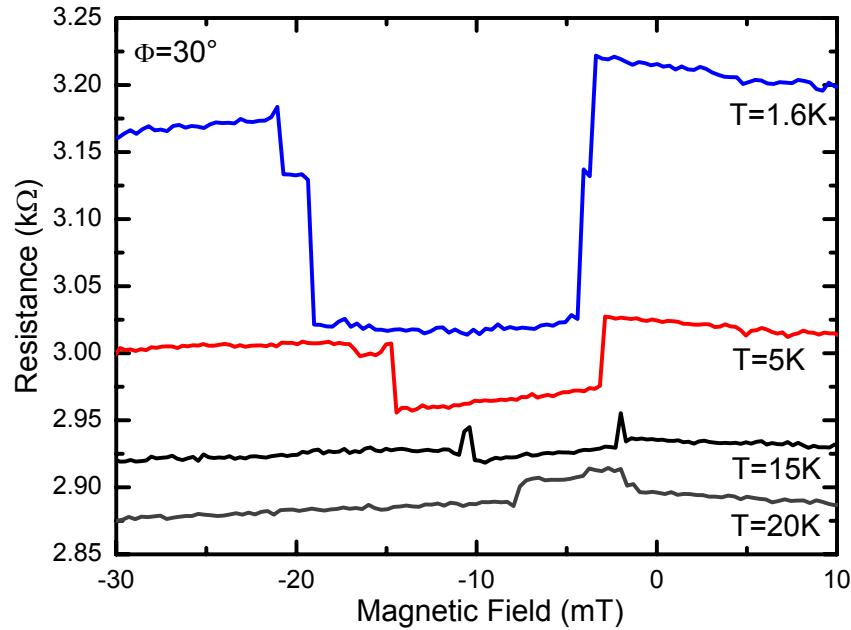
Figure 6.8: TAMR along $\phi = 30°$ for temperatures ranging from 1.6 to 20 K showing a change of sign of the spin valve-like feature. The curves are vertically offset for clarity.

is nominally identical to the single sided spin valve sample which showed the TAMR features presented above. For an understanding of the following analysis it should be kept in mind that the SQUID magnetometer only measures a projection of the magnetization and not its absolute value. For the magnetometer which is used here, the direction of sensitivity is parallel to the direction of applied magnetic fields. If the total magnetization equals a value M_t and lies at an angle θ with respect to the SQUID measurement axis, then the measured value is simply $M_m = M_t \cdot \cos(\theta)$.

Figure 6.11a contains a measurement with the magnetic field along the [110] hard axis of the layer and another one with the magnetic field along the [010] easy axis. From the magnitudes of the measured magnetic moments one easily concludes that the total magnetic moment of the layer is $1.01 \cdot 10^{-5}$ emu. This is extracted from the measurement of the [110] axis, because an alignment along an edge of the sample is much more accurate than an alignment along an easy axis which is 45° rotated with respect to the edges (the SQUID measurement reveals 4° of misalignment[3]).

For the data presented in Fig. 6.11b the sample was aligned with its [110] edge 15° off the SQUID measurement axis in the counter clockwise direction. The remanent magnetization is $8.56 \cdot 10^{-6}$ emu, which is just the projection of the total magnetic moment that lies on an easy axis 31.2° off the magnetic field direction. This fits nicely to the nominal 30° alignment that was intended. The large step in the hysteresis loop is associated with a 90° switching of the magnetization from [100] to [0$\bar{1}$0]. Consequently the subsequent small step is another 90° switching and the SQUID magnetization reversal is consistent with the transport results. Finally it should be noted that the magnetization reversal during measurement along the [110] axis also

---

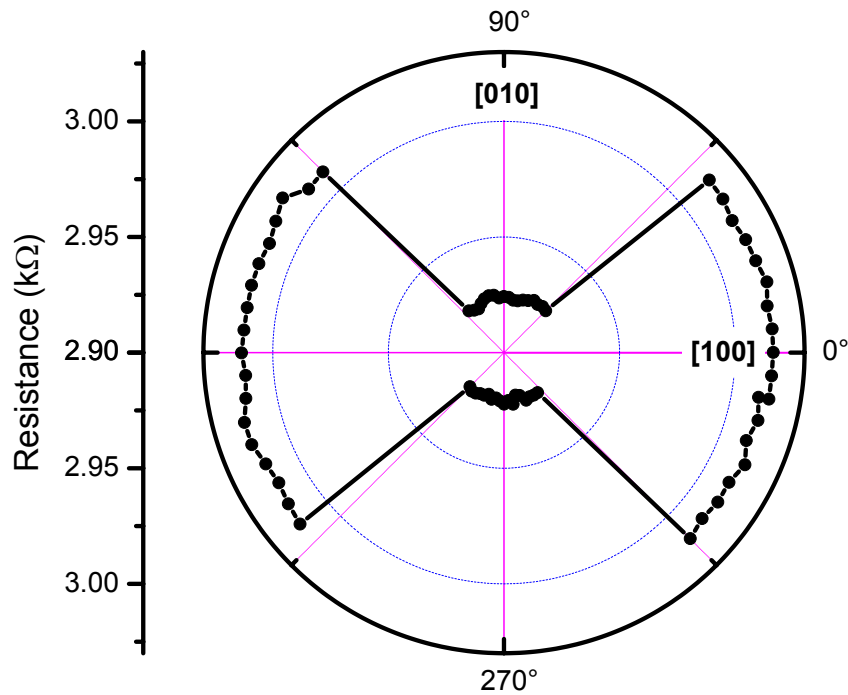[3]Due to the nature of the SQUID sample holder carrier this is within experimental error.

Figure 6.9: Resistance of the single sided spin valve at T=4.2 K measured at 0 mT after the magnetic state has been prepared by saturating the magnetization with an in-plane magnetic field along an angle ϕ. The data clearly shows that the resistance is anisotropic with respect to the magnetization direction.

happens via two 90° steps. The second step however, is invisible in SQUID because although the direction of the magnetization changes, the projection onto the SQUID measurement direction remains the same.

6.7 TAMR Modelling

In the previous section it was shown that the observed TAMR features occur due to the simultaneous existence of and interplay between (i) the anisotropy of the tunneling resistance of (Ga,Mn)As with respect to the orientation of the (Ga,Mn)As magnetization and (ii) the presence of a specific magnetic anisotropy promoting double step magnetization reversal. Consequently the modelling of TAMR must consist of a separate treatment of resistance and magnetic anisotropy.

6.7.1 Double Step Magnetization Reversal

The distribution of switching events presented in the form of the polar plot of Fig. 6.7 displays a striking resemblance to the switching behavior previously observed in magneto-optical studies of epitaxial Fe films [Cow95] and (Ga,Mn)As [Moo03], and to a lesser degree in transport studies on (Ga,Mn)As in the in-plane Hall geometry [Tan03]. It is associated with materials
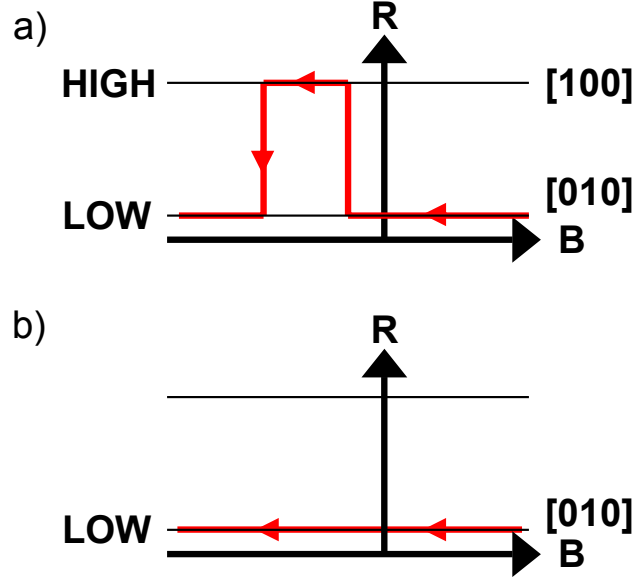
Figure 6.10: (a) Sketch of spin valve feature associated with double step magnetization reversal sequence: [010]→[100]→[0$\bar{1}$0] (b) No feature is observed in the magnetoresistance when the layer undergoes single step switching, e.g. [010]→[0$\bar{1}$0].

that reverse their magnetization in two steps by the nucleation and propagation of 90° domain walls.

General Model

A simple phenomenological model of magnetization reversal that fits very well to the above presented data is developed in [Cow95] and outlined below. Sample alignment and coordinate system are assumed to be as sketched in Fig. 6.3b. This coordinate system is different than that used in [Cow95] and thus the following derivation is altered respectively. The starting point is to write down the total magnetic energy E of an arbitrary single magnetization orientation. In order to describe the experiment the following energy terms have to be included: a fourfold in plane anisotropy along the [100] and [010] axes, a small uniaxial anisotropy along the [010] axis and the Zeeman energy of the domain in the external magnetic field. Thus for the energy of the domain we get the expression

$$E = K_u \cos^2(\theta) + \frac{K_1}{4} \sin^2(2\theta) - MH\cos(\theta - \phi), \tag{6.1}$$

where K_u is the in-plane uniaxial anisotropy constant, K_1 is the in-plane biaxial anisotropy constant, θ is the domain orientation, M is the magnitude of the magnetization, H is the applied field magnitude and ϕ is the external field direction. θ and ϕ are defined as being zero along the [100] axis, which lies at 90° with respect to the uniaxial easy axis.

In the Stoner-Wohlfarth picture of coherent rotation [Sto48], the spin orientation θ is such that the magnetization resides in a local energy minimum. In the TAMR sample, Stoner-Wohlfarth coherent rotation is the pertinent mechanism at every magnetic field except at the
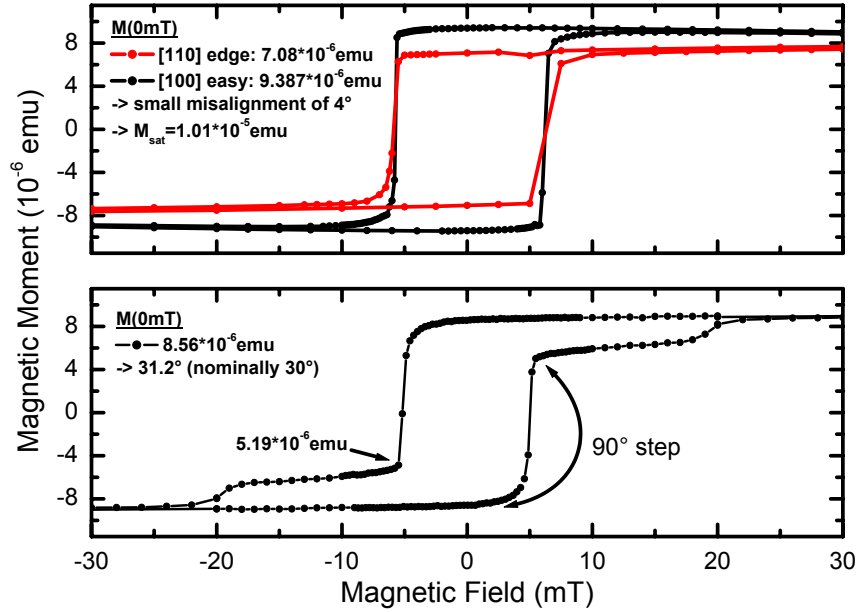
Figure 6.11: SQUID measurements on a Au/AlOx/GaMnAs sample nominally identical to the single sided TAMR layer. The measurements along the different angles show the validity of the employed magnetization reversal / magnetic anisotropy model. (a) Measurements with the magnetic field along the [100] easy and the [110] hard axis. (b) The measurement is conducted with the magnetic field oriented 15° off the [110] edge of the sample.

sharp switching events. It is clear that these switchings cannot be explained by coherent rotation because they happen at fields that are too low to account for the high energy cost of coherent rotation. The central idea is instead that one has to depart from the Stoner-Wohlfarth picture by allowing the spin orientation to transition from one local energy minimum of the energy landscape to another by the propagation of a magnetic domain wall.

The mechanism is illustrated schematically in Fig. 6.12. The single domain energy according to Equ. 6.1 is plotted on the y-axis as a function of the domain orientation θ. In the upper half of the figure at zero magnetic field, the magnetization remains in a local energy minimum at 90°. Subsequently a magnetic field is applied along 180°. The higher the magnetic field amplitude is, the more favorable this orientation becomes. As soon as the energy gain from a 90° switch becomes larger than the domain wall energy "cost" $\varepsilon_{90°}$, the sample transitions to 180° via domain walls sweeping across the sample.

The correct interpretation of $\varepsilon_{90°}$ is most likely that it is a depinning energy rather than a nucleation energy because it is conceivable that a small number of microscopic domain walls are simply always present, nucleating due to sample inhomogeneities. Note however, that the lack of fine structure in the transport behavior suggests that the sample is not impaired in any way by the existence of these domain walls and that the single domain approximation is largely valid. For the interpretation of the energetics of the switching behavior, however, the above distinction is irrelevant.

As an example, let the magnetic field be applied at an angle between $\phi=0$ and 45° and the magnetization lies along the $[0\bar{1}0]$ axis. The energy gain of a transition between the relevant
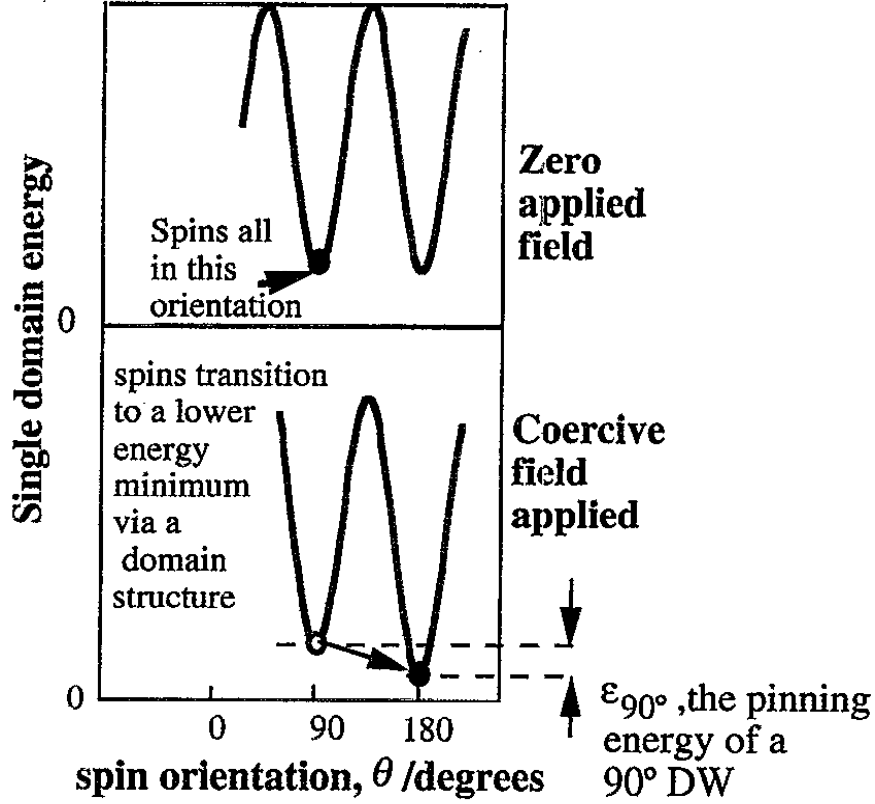
Figure 6.12: Schematic presenting the model for a 90° magnetization reversal via the propagation of a domain wall. Picture taken from [Cow95].

local minima would be, for a single step 180° switching

$$\Delta E = E_{[0\bar{1}0]} - E_{[010]} = 2MH \sin(\phi) \tag{6.2}$$

and for a double step- (two successive 90°-) switching processes

$$\Delta E_1 = E_{[0\bar{1}0]} - E_{[100]} = 2MH(\cos(\phi) + \sin(\phi)) - K_u, \tag{6.3}$$

$$\Delta E_2 = E_{[100]} - E_{[010]} = 2MH(\sin(\phi) - \cos(\phi)) + K_u. \tag{6.4}$$

The condition for domain wall assisted switching is that at the coercive field

$$\Delta E > \varepsilon, \tag{6.5}$$

i.e. the energy gain ΔE is infinitesimally bigger than the domain wall propagation energy ε. This energy can certainly be different depending on whether we deal with a 180° or 90° domain wall ($\varepsilon_{90°} \neq \varepsilon_{180°}$). Since, as pointed out above, the single step switching is not visible in the TAMR transport data, the rest of the analysis will focus on the double step switching. What we want to know from the above derivation is the switching field of our sample. The switching

Table 6.1: Proper signs υ_1, υ_2 as a function of magnetic field angle ϕ, to be used in conjunction with formula 6.6.

ϕ/deg	υ_1	υ_2
0-45	1	-1
45-135	-1	1
135-225	1	-1
225-315	-1	1
315-360	1	-1

condition given by Equ. 6.5 yields analytical expressions for the coercive fields H_{c1} and H_{c2} that are associated with the double step switchings, i.e.

$$H_{c1} = \frac{\varepsilon_{90°} + \upsilon_1 \cdot K_u}{M|\cos(\phi)| + |\sin(\phi)|},$$

$$H_{c2} = \frac{\varepsilon_{90°} + \upsilon_2 \cdot K_u}{M||\cos(\phi)| - |\sin(\phi)||}, \tag{6.6}$$

where υ_1 and υ_1 are simply sign factors of ± 1. The dependence of the signs on the angle ϕ is given in table 6.1.

Fit to Experimental Data

The analytical result given above enables us to go back to the experimental data presented in Fig 6.7 and fit the observed switching fields with the analytical expressions of Equ. 6.6. Adjustable parameters are the domain wall pinning energy $\varepsilon_{90°}/M$ and the strength of the uniaxial anisotropy K_u/M, both normalized by the sample magnetization. The result of the fit is presented in Fig. 6.13. The circles indicate the experimentally observed switching events H_{c1} and H_{c2} and the solid line is the fit data. Note that only double step switching is visible in the TAMR data and thus there is no experimental data available around the [010]/90° axis. It can be seen that the agreement between theory and experiment is excellent. The fit yields values of 450 erg/cm^3 for K_u and 1550 erg/cm^3 for $\varepsilon_{90°}$.

The good agreement between magnetic switching theory and experiment shows that we have a quantitative understanding of the magnetization reversal in this (Ga,Mn)As sample. There are similarities between this ferromagnetic semiconductor and the magnetization reversal in epitaxial magnetic metallic thin films [Cow95], despite the fact that there exist many differences with respect to the electronic properties. It seems that the material fits well to the theoretical assumption of a single domain, which means that the magnetized state is quite homogeneous on the length scale of ≈ 100 μm. In contrast, the microscopic origin of uniaxial anisotropy and double step switching is not understood, despite it being observed by other groups as well [Moo95].

Microscopic Origin of Double Step Switching

One possible explanation could be that the symmetry of the underlying high temperature GaAs buffer layer which during growth has a surface reconstruction of 2×4 in RHEED is responsible
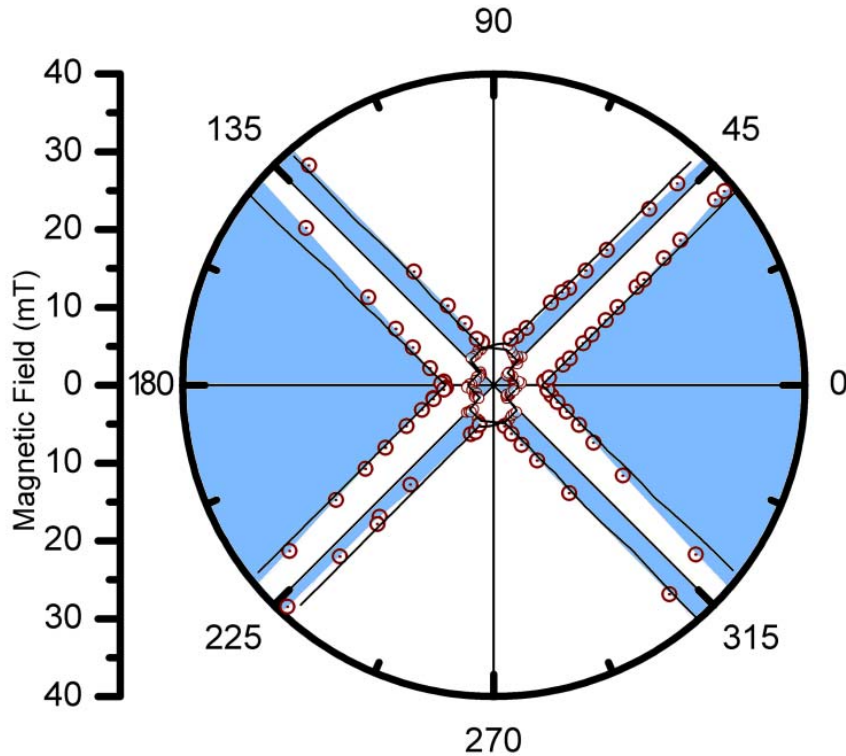
Figure 6.13: Polar plot containing a fit of the double step magnetization reversal behavior observed in the Au/AlOx/GaMnAs tunnel junction. The circles indicate the experimentally observed switching events H_{c1} and H_{c2}. The solid line is a fit with the model described in the text (Equ. 6.6).

for the uniaxial anisotropy. The subsequently grown low temperature GaAs buffer has a surface reconstruction of 1×1 but is intentionally kept very thin (1 nm). Hence it is conceivable that the (Ga,Mn)As layer is still affected by the properties of the high temperature GaAs. In addition the coverage by an overlayer possibly decreases domain wall nucleation and propagation energies. To clarify whether the above conditions favor double step switching, a number of SQUID hysteresis measurements were conducted on samples taken from wafer S20. The list of samples consisted of S20 as grown, S20 covered with a thin (2 nm) AlOx overlayer, S20 covered with a Au overlayer and a sample that is nominally identical with the above presented transport structure. The hysteresis measurements were conducted at 4.2 K with the magnetic field at an angle ($\approx 15°$) with respect to the [110] edge which ensures a near optimum visibility of the double step signature in SQUID. As can be seen in Fig 6.14, the as grown sample shows a square hysteresis loop but all investigated samples with an overlayer show clear double step switching behavior. This indicates that indeed an overlayer can substantially modify the magnetic anisotropy and/or switching behavior of (Ga,Mn)As in a way that promotes double step magnetization reversal.

A second speculation is that step edges on the surface of the GaAs wafers are responsible for the observed magnetic anisotropy. Step edges always occur when semiconductor wafers are miscut, i.e. when the surface of the substrate is tilted. The typical error of the orientation of a commercial GaAs substrate is about $\pm 0.1\%$. In order to investigate the effects of miscut,
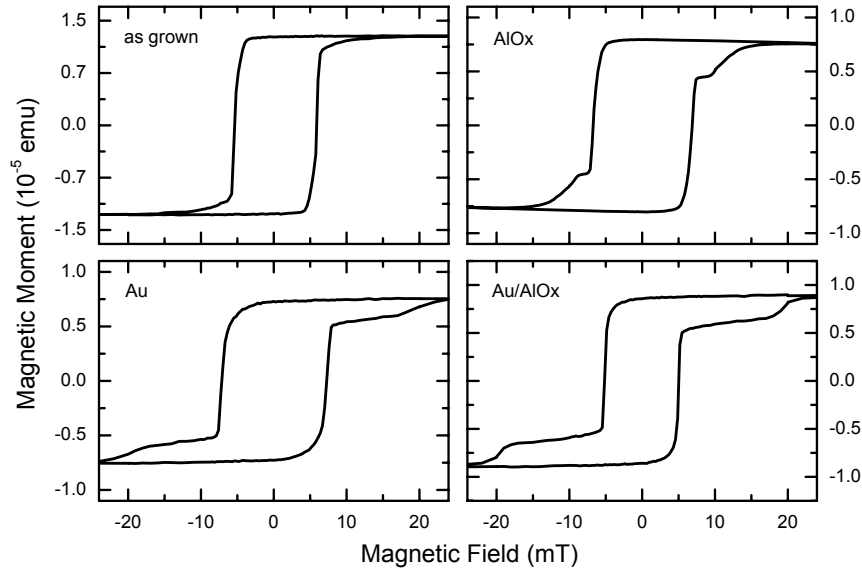
Figure 6.14: SQUID hysteresis measurements on samples cleaved from wafer S20 with various overlayers.

(Ga,Mn)As thin films nominally identical to S20 were simultaneously grown on a number of undoped GaAs wafers with an intentional miscut of 5° into various crystal directions plus one substrate without miscut. The corresponding SQUID hysteresis measurements are shown in Fig. 6.15. Out of this set, the sample without miscut showed comparatively small yet noticeable hints of double step switching and all samples with miscut showed clear double step or even more complicated switching patterns. No correlation was found between the orientation of the miscut and the strength of change in anisotropy / double step switching.

In summary it can be said that although the magnetic anisotropy and switching dynamics are quantitatively very well understood, the microscopic origin of this behavior is not well understood. Possible explanations could involve factors like a symmetry breaking due to the underlying high temperature GaAs buffer and domain wall nucleation facilitated by overlayers and/or step edges due to vicinally cut substrates.

6.7.2 Resistance Anisotropy

The above analysis allows a comprehensive prediction of the magnetization dynamics during a magnetoresistance measurement. However, one additional ingredient is missing to explain why the spin valve-like features are observed in transport, i.e. why the resistance of the sample depends on the direction of the magnetization. To explain this anisotropy of the tunneling resistance, one must turn to an analysis of the electronic density of states in the valence band of (Ga,Mn)As. Why this is true is fairly obvious: tunneling transport between two electrodes is determined by the details of the tunnel barrier and by the density of states of the electrodes as described in section 2.5.

The following theoretical analysis is a consideration of whether anisotropies in the (Ga,Mn)As density of states with respect to the magnetization orientation are large enough to explain the
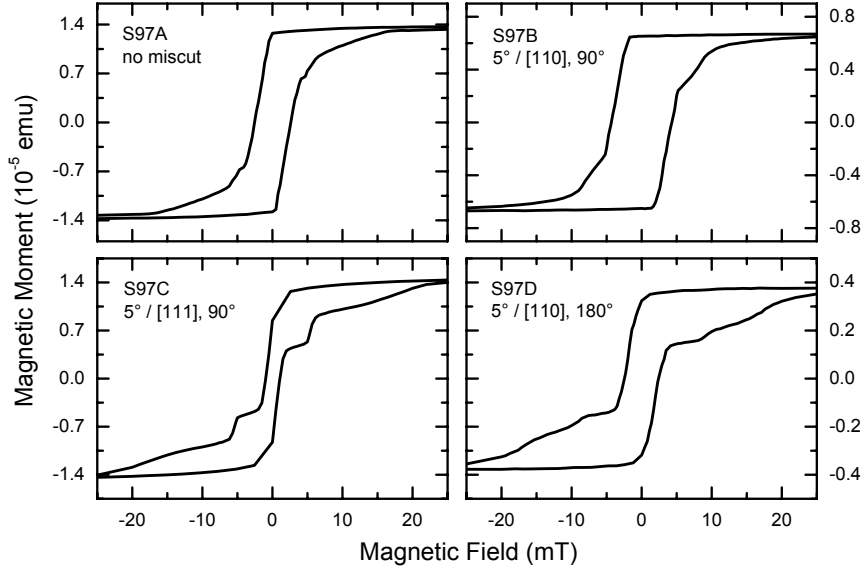
Figure 6.15: SQUID hysteresis measurements of (Ga,Mn)As thin films nominally identical to sample S20 but grown on a number of GaAs substrates with and without intentional miscut.

observation of a TAMR effect on the order of a few percent. An overview of the valence band structure of (Ga,Mn)As and carrier-induced ferromagnetism can be found above in section 3.3. Technical details about the underlying model and the full (Ga,Mn)As valence band structure are given in [Abo01].

The analysis is based on a calculation of the electronic structure of (Ga,Mn)As by T. Jungwirth which uses a $\vec{k} \cdot \vec{p}$ envelope function description of the GaAs host valence bands. The magnetic interactions are accounted for by the inclusion of an effective exchange field, $\vec{h} = J_{pd}\vec{S}_{Mn}$, produced by the polarized Mn local moments with spin density $\vec{S}_{Mn}$ [Abo01].

The above mentioned model includes biaxial in-plane strain and hence has in-plane symmetry of the [100] and [010] directions. It is thus not yet sufficient. In order to account for the experimentally observed inequivalence of the magnetic easy axes, an in-plane uniaxial strain term of order 0.1% was introduced into the band structure calculations. An analysis of the resulting density of states shows that due to a very strong spin-orbit interaction in the valence band such a small strain leads to values of K_u comparable to the one estimated above, as well as to sizable DOS anisotropies. It should be noted that although the strain term correctly describes the experimental observations, at this point only speculations exist about the true microscopic origin of the anisotropies[4]. Its inclusion should be viewed only as a phenomenological description of the observed symmetry breaking.

The experimental Curie temperature of 70 K is reproduced theoretically assuming the hole density $3 \cdot 10^{20}$ nm^{-3} and 4% of the cation sites occupied by Mn, which is reasonably consistent with the experimental estimates.

The z-axis is taken to be the growth direction. Defining the partial DOS as the DOS at a given k$_z$ and for a given band, Fig. 6.16 shows the relative partial DOS anisotropy ($\Delta\text{DOS}_{\text{partial}} \equiv$

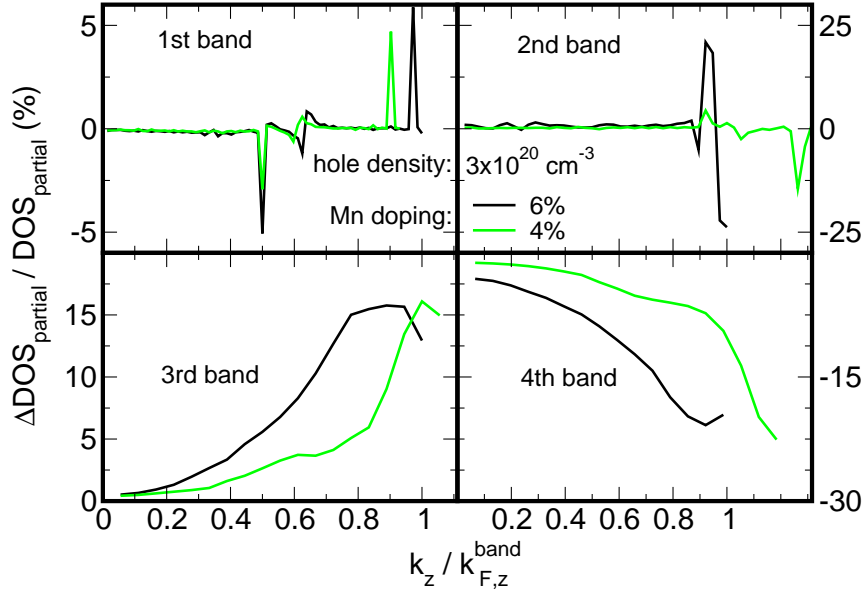[4]Please refer to the discussion at the end of section 6.7.1.

Figure 6.16: The relative difference between partial DOS at the Fermi energy for *M* along [010] and [100] directions is plotted separately for each of the four occupied valence bands. Note that in the ferromagnetic state, even the near k=0, states cannot properly be called light and heavy holes due to the p-d exchange interaction. Green lines correspond to Mn_{Ga} concentration of 4%; black lines corresponding to 6% Mn doping are shown for comparison.

$DOS_{partial}(M\|[010]) - DOS_{partial}(M\|[100]))$ at the Fermi energy E_F calculated as a function of the out-of-plane wavevector k_z for each of the four occupied bands that derive from the GaAs heavy- and light-hole states which are spin-split due the presence of the Mn-moment induced exchange field [Abo01]. $k_{F,z}^{band}$ is the Fermi wavevector in the given band for Mn_{Ga} concentration of 6%.

The total DOS (DOS_{total}) is obtained by integrating over all k_z up to the Fermi wavevector $k_{F,z}$ and summing over all bands. DOS_{total} has an anisotropy at E_F of less than 1% with respect to the magnetization orientation. This is much smaller than the observed magnitude of the TAMR effect. The tunnel conductance is, however, proportional to the DOS_{total} only if in-plane momentum is not conserved during the tunneling. For cleaner barriers and interfaces, in-plane momentum is at least partially conserved. In general a tunneling current is dominated by carriers with momentum vectors normal to the barrier, because the tunneling probability decreases rapidly when the momentum deviates from the barrier-normal direction. In other words this mechanism results in a higher probability of tunneling for states with higher band and k_z indices. Hence it makes sense to assume that only a subset of the DOS at the Fermi energy with k_z larger than a certain minimum wave vector plays a role in a real sample. Such a subset DOS_{int} is determined by choosing an appropriate minimum wave vector $k_{z,min}$, integrating the partial DOS up to $k_{F,z}$ and summing over all four bands.

As demonstrated in Fig. 6.16, the $DOS_{partial}$ in some of the bands can change by tens of percents upon magnetization reorientation. This is especially true for states with high k_z. Furthermore it is obvious that the density of states anisotropy varies dramatically with k_z, the barrier-

normal wave vector, and the Mn doping level. All experimental parameters influencing these variables will strongly influence the amplitude of the observed TAMR effect. The magnitude and even the sign of the overall tunnel magnetoresistance effect is dependent on parameters of the (Ga,Mn)As film, such as the density of local spins on substitutional Mn impurities, or on the barrier and interface character which may select different ranges of band and k_z states that dominate the tunneling current.
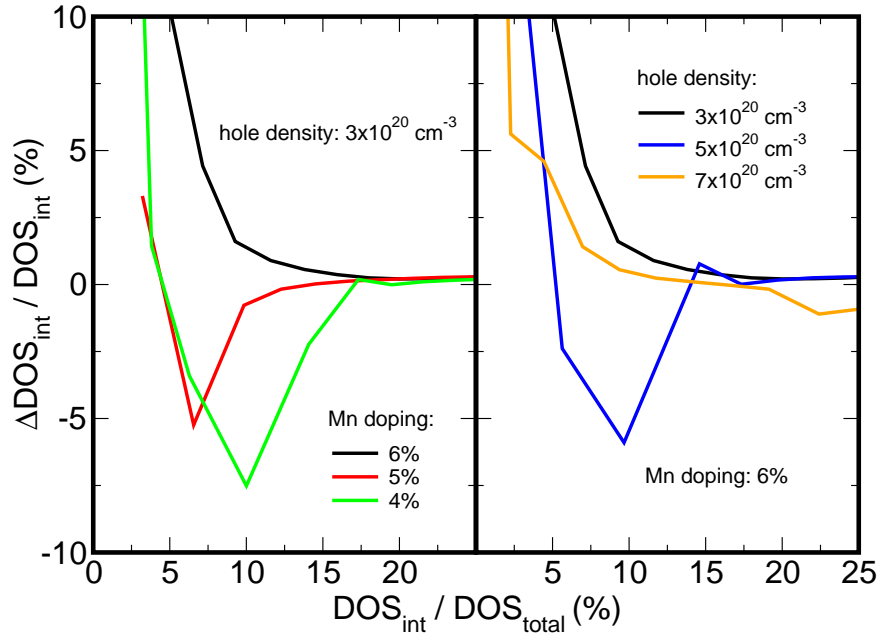

Figure 6.17: The relative integrated DOS anisotropy is plotted for different Mn (left panel) and hole (right panel) concentrations. The x-axis represents the fraction of the DOS at the Fermi energy that is assumed to contribute to tunneling, relative to the total DOS at the Fermi energy. Moving from left to right corresponds to gradually relaxing the momentum conservation condition.

It is obvious that the local values of these quantities are very hard if not impossible to assess experimentally. Therefore the in-plane momentum conservation condition, respectively DOS_{int} as defined above, is treated as a parameter. To estimate the overall size of the magnetoresistance effect produced by the (Ga,Mn)As $DOS_{partial}$ anisotropy we start with the assumption that for clean barriers (perfect in-plane momentum conservation) the tunneling is dominated by states in the (Ga,Mn)As with k_z close to k_F in each band and that the tunneling probability of these states is independent of the band index. This corresponds to low DOS_{int} values in Fig. 6.17. We then gradually relax the momentum conservation condition by adding states at E_F with decreasing k_z.

In Fig. 6.17 the relative difference between this integrated DOS_{int} for the two magnetization orientations is plotted. All curves have in common that for "dirtier" barriers (values of $DOS_{int}/DOS_{total} > 15\%$) the theoretically predicted magnetoresistance effect is very small. Depending on the exact values of hole density and Mn doping, the effect can increase for lower DOS_{int} but it may even change signs for some values. From this model it can be expected

that cleaner, e.g. epitaxial tunnel barriers have the potential to yield larger magnetoresistance values. Looking at the 6% Mn and p=7·10^{20} cm^{-3} curve, whose values fit very well with our experiment, it can be seen that for ≈10% of the total DOS at E_F participating in the tunneling process, the theoretical DOS$_{int}$ anisotropy is consistent with the experimentally observed TAMR of order several percent.

The theoretical approach chosen here also allows to qualitatively assess what can happen to the TAMR effect as a function of temperature. The curves in the left panel of Fig. 6.17 are labelled by different Mn doping concentrations and illustrate the general dependence of the magnetoresistance effect on the Mn local spin density. In mean-field theory, the (Ga,Mn)As electronic structure depends only on the overall value of the effective exchange field $\vec{h} = J_{pd}\vec{S}_{Mn}$. It makes no difference whether the spin-density magnitude $|S_{Mn}|$ changes through varying the number of Mn impurities at a fixed temperature or through the temperature-dependent average spin polarization of an individual Mn local moment at a fixed doping level. A modelled change in Mn concentration is thus equivalent to a change of temperature in the experiment. Consequently the data in the left panel of Fig. 6.17 suggest that the sign of the tunnel magnetoresistance effect can change with temperature. This is consistent with the experimental observations shown above in Fig. 6.8. Note that the theoretical change of sign occurs solely as a function of temperature. The uniaxial anisotropy energy, i.e. the phenomenological uniaxial strain term and the magnetic anisotropy remain unchanged.

6.8   Summary

The TAMR studied here shows a rich phenomenology that opens new directions in spintronics research. TAMR is caused by the interplay of the anisotropic density of states in (Ga,Mn)As with respect to the magnetization direction and the two-step magnetization reversal process in the material. Both aspects are well understood theoretically and our modelling is consistent with the experiment.

Avoiding the second ferromagnetic layer may have fundamental consequences for the operation at high temperatures as it illuminates the need for a buried ferromagnetic layer which cannot be effectively treated by post-growth annealing. The data also demonstrate that the sign of the spin-valve like signal, i.e., whether a high- or low-resistance state is realized at saturation, can change with the angle at which an external magnetic field is applied, with temperature, or structural parameters of the (Ga,Mn)As layer, interfaces, and the tunnel barrier.

Last but not least, these experiments provide a new perspective on tunnel magnetoresistance in structures with two ferromagnetic contacts. The need for caution in analyzing spin-valve experiments is demonstrated, especially in materials where strong spin-orbit coupling is present. As shown above, the existence of a spin-valve like signal does not automatically imply the injection and detection of a spin-polarized current in the tunneling structure. In the next chapter it will be shown that even the characteristics of tunnel junctions containing two ferromagnets can be dominated by TAMR.

Chapter 7

Very Large TAMR of a (Ga,Mn)As/GaAs/(Ga,Mn)As Stack

7.1 Introduction

In the previous chapter it was demonstrated that it is possible to measure a spin valve-like signal using a magnetic tunnel junction with a single ferromagnetic layer only. This behavior was explained using the novel tunneling anisotropic magnetoresistance (TAMR) effect. TAMR is expected to be very sensitive to the magnetic anisotropy of the used (Ga,Mn)As layer, the details of its band structure and the quality of the tunnel barrier. The results show that TAMR can mimic the functionality of metal tunnel magnetoresistance (TMR) devices while at the same time featuring additional spintronics features not attainable with the conventional device approach. The single sided spin valve described above constitutes the first experimental realization of this effect and quite naturally opens up a multitude of follow-up questions.

One of these is whether TAMR can also play a role when two or more (Ga,Mn)As layers are combined in a magnetic tunnel junction. Such devices have already been studied in the past by a number of groups [Hig01, Chi04] with some promising results. The interpretation however was more closely related to traditional metal TMR which implies the injection and detection of a spin-polarized current in the tunneling structure. Nevertheless it is possible that these results have to be re-evaluated in the light of TAMR.

Since magnetic tunnel junctions have great potential for applications in magnetic field sensors, their performance is linked to the magnitude of the measured magnetoresistance effects. Therefore, from an application point of view, the peak to valley ratio of the spin valve-like feature should be maximized. When considering the modelling of the tunneling resistance anisotropy presented in section 6.7.2, two possibilities immediately emerge. Firstly, larger magnetoresistance is predicted for a better momentum conservation during tunneling. One way to realize this is to use a cleaner, epitaxial tunnel barrier instead of the polycrystalline AlOx that was used previously. Secondly, it is reasonable that the magnetoresistance can be enhanced by replacing the previously used top gold electrode with a second (Ga,Mn)As layer that also has an anisotropic density of states. Hence the investigation of a fully epitaxial (Ga,Mn)As/GaAs/(Ga,Mn)As stack which is presented in this chapter is a natural follow-up experiment that helps to answer some of the above questions.

7.2 Sample Details

All measurements presented in this chapter were conducted on samples based on wafer number S31. The full layer structure of this epilayer is shown in Fig. 7.1a. It consists of a $Ga_{0.94}Mn_{0.06}As$ (10 nm)/GaAs (2 nm)/$Ga_{0.94}Mn_{0.06}As$ (100 nm) trilayer grown by G. Schott using low temperature molecular beam epitaxy (LT-MBE) on a semi-insulating GaAs substrate and an undoped GaAs buffer layer. The (Ga,Mn)As layers are intrinsically highly p-type due to the Mn and have metallic transport character. The undoped LT-GaAs layer on the other hand is insulating and forms an epitaxial tunnel barrier between the two ferromagnetic layers. The Curie temperature of the (Ga,Mn)As is about 65 K, as determined from a SQUID measurement of the remanent magnetization. This value is consistent with the expected as grown Curie temperature for a high quality (Ga,Mn)As layer with 6% Mn content.
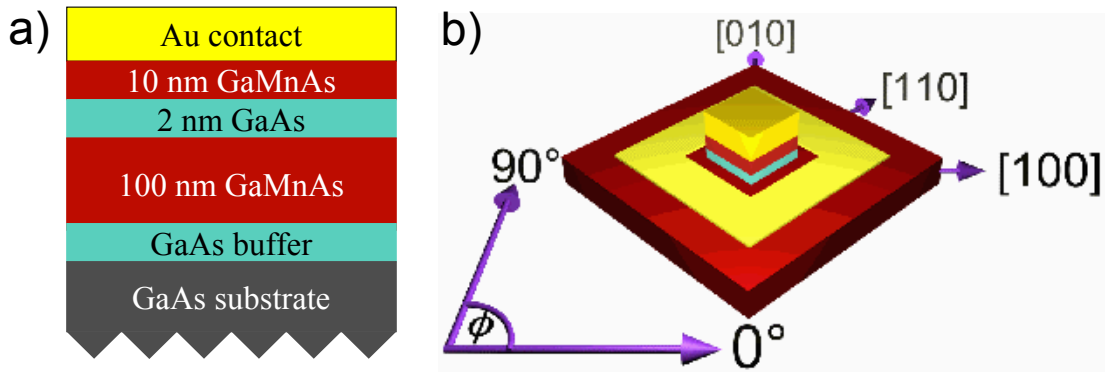

Figure 7.1: a) Layer stack used to fabricate (Ga,Mn)As/AlOx/(Ga,Mn)As tunnel junctions. b) Sample layout of a (Ga,Mn)As/AlOx/(Ga,Mn)As tunnel junction. The angle ϕ of the applied in plane magnetic field is related to the crystal directions in the thin film.

A schematic of the final transport device is shown in Fig. 7.1b. Using optical lithography with positive photoresist followed by metal evaporation and lift-off, the heterostructure was patterned into an inner square contact mesa with sides of 100 μm and a surrounding electrical back contact. The top of the square mesa is formed by an in-situ Ti/Au multilayered contact to the upper 10 nm thick (Ga,Mn)As layer. The back contact is formed by depositing W/Au onto the lower 100 nm thick (Ga,Mn)As layer. This sample structure makes it possible to perform two-probe magnetoresistance measurements vertically through both ferromagnetic layers and the GaAs tunnel barrier. The effectiveness of the tunnel barrier is confirmed by tunneling-type nonlinear I-V characteristics, some typical results of which are shown in Fig. 7.2. It is important to note that the resistance of the device is fully dominated by the vertical tunneling process through the tunnel barrier: identically patterned control samples without a tunnel barrier have a resistance of the order of 10 Ω which is consistent with the bulk resistivity of the (Ga,Mn)As ($\approx 10^{-3}$ Ωcm). In contrast, the sample described below to exhibit the tunneling anisotropic magnetoresistance effect has a resistance of approximately 500 kΩ in its lowest resistance state at T=4.2 K. This renders any contributions coming from the bulk magnetoresis-
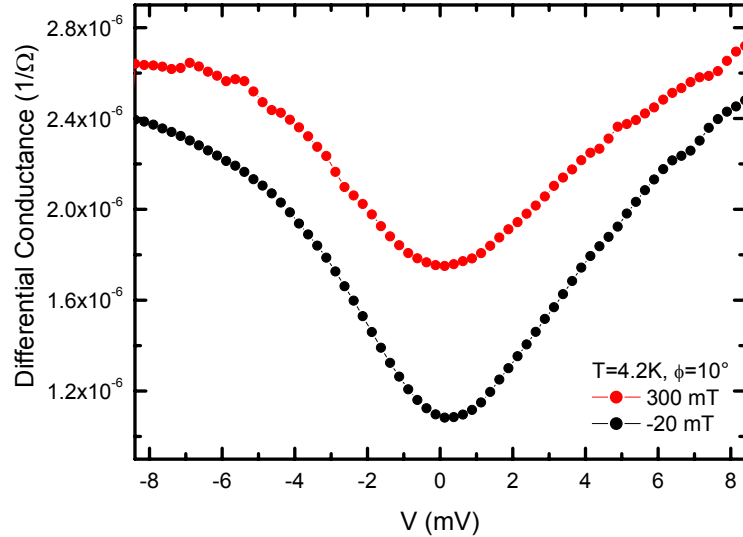
tance of (Ga,Mn)As fully negligible.

Figure 7.2: Typical differential conductance curves measured at T=4.2 K. The nonlinearity and overall high resistance confirms the effectiveness of the tunnel barrier.

As before, transport measurements were carried out in a magnetocryostat fitted with a variable temperature insert and a set of three mutually orthogonal magnet coils. They allow for the application of magnetic fields of up to 300 mT in any direction. Fields applied in the plane of the multilayer are denoted by the angle ϕ with respect to the [100] crystal direction, as indicated in Fig. 7.1b. Two different types of experiments were carried out on the sample. Firstly, the measurement of the magnetoresistance is performed by saturating the sample magnetization at an angle ϕ_0 and then measuring the resistance of the device as the magnetic field magnitude H is swept up or down at constant angle ϕ_0. The second type of experiment is a ϕ-scan and consists of measuring the resistance while sweeping the magnetic field angle ϕ at a constant magnitude H_0.

7.3 Magnetoresistance Properties at 4.2 K

Figure 7.3 shows magnetoresistance scans taken with a bias voltage $V_B = 10$ mV at a temperature T = 4.2 K along $\phi = 10°$ (red) and $100°$ (black), near the two in plane magnetic easy axes in the (Ga,Mn)As. For both directions and in fields bigger than 30 mT, the resistance of the device exhibits only gradual changes caused by a rotation of the magnetization of the two layers between the applied field and the respective easy axes. However, at low $|\mathbf{H}|$, after crossing zero in either sweep directions, $\mathbf{M}$ abruptly reverses its direction. This manifests itself in transport as a discontinuous change in resistance leading to a 40% spin-valve signal. The measurement along $100°$ appears similar to previous observations [Hig01], and could easily be mistaken for traditional TMR. The measurement along $10°$ however yields an inverted spin valve signal. The remarkable sign change and the fact that both curves exhibit switching between a high and a low resistance level lying at ≈ 700 kΩ and ≈ 500 kΩ respectively, point to a different origin

of the effect. This behavior strongly suggests an interpretation in line with the observations of TAMR in single-ferromagnet devices presented above.
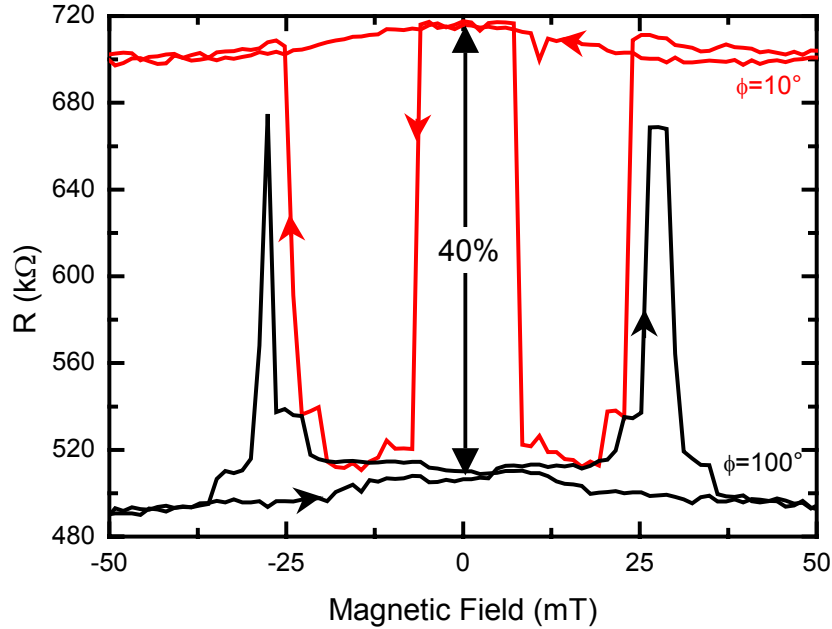

Figure 7.3: Magnetoresistance measurements taken with a bias voltage $V_B = 10$ mV at a temperature T = 4.2 K along $\phi = 10°$ (red) and $100°$ (black), near the two in plane magnetic easy axes in the (Ga,Mn)As.

Figure 7.4 displays the angular dependence of the magnetoresistance of the same sample at V=-10 mV and T=4.2 K. The curves are offset vertically for better clarity. Only measurements with the magnetic field along angles ranging from 0° to 170° are shown since the complementary scans are simply hysteretically symmetric. Neglecting some fine structure on top of the main features, it can be seen that the magnetoresistance curves closer to the 0°/[100] (or equivalent) easy axes exhibit inverted spin valve features and the curves closer to the 90°/[010] (or equivalent) easy axes exhibit positive spin valve features. As in the single ferromagnet tunnel junctions, the amplitude of the effect remains constant, whereas the position and sign of the sharp switching events displays a strong angular dependence. Minima of the coercive field occur around 0° and 90°. Due to a richness of features and the relatively wide spacing in the data there is an error of about ±5% in the identification of the magnetic easy axes from the transport data. However, for convenience the location of the [100] and [010] axes are in the following assumed to lie exactly along 0° and 90°. Note that this experimental error of a few degrees does not change the validity of the following analysis at all.

For fields farther away from the easy axes, the transport features become broader. The maximum coercive fields are present at ≈45° and ≈135°, close to the directions along the edges of the sample. These are also the directions exhibiting the strongest continuous variation of the sample resistance. In contrast, along the easy axes, the magnetoresistance is comparably flat outside the switching events. This is consistent with a high-field magnetization reversal by Stoner Wohlfarth-like coherent rotation of the magnetic layers.

All of the above mentioned major features of the data are clearly consistent with the corresponding angular dependence displayed in Fig. 6.6 for the single ferromagnet TAMR sample. By analogy, the data thus allows the conclusion that for both ferromagnetic layers the [010] crystal direction is a direction that is energetically favorable due to the additive effect of a uniaxial plus a fourfold magnetic anisotropy term whereas the [100] crystal direction is slightly less "easy" because it is uniaxial "hard". Once again there exists an anisotropy of the sample resistance with respect to the magnetization direction: M∥[010] corresponds to a low sample resistance state and M∥[100] corresponds to a high sample resistance. The main spin valve features can thus again be explained in a natural way using the picture of domain wall assisted switching between the two easy axes which is described in detail in section 6.7.1. None of the measured curves contain any significant contributions from TMR in the Julliere picture.
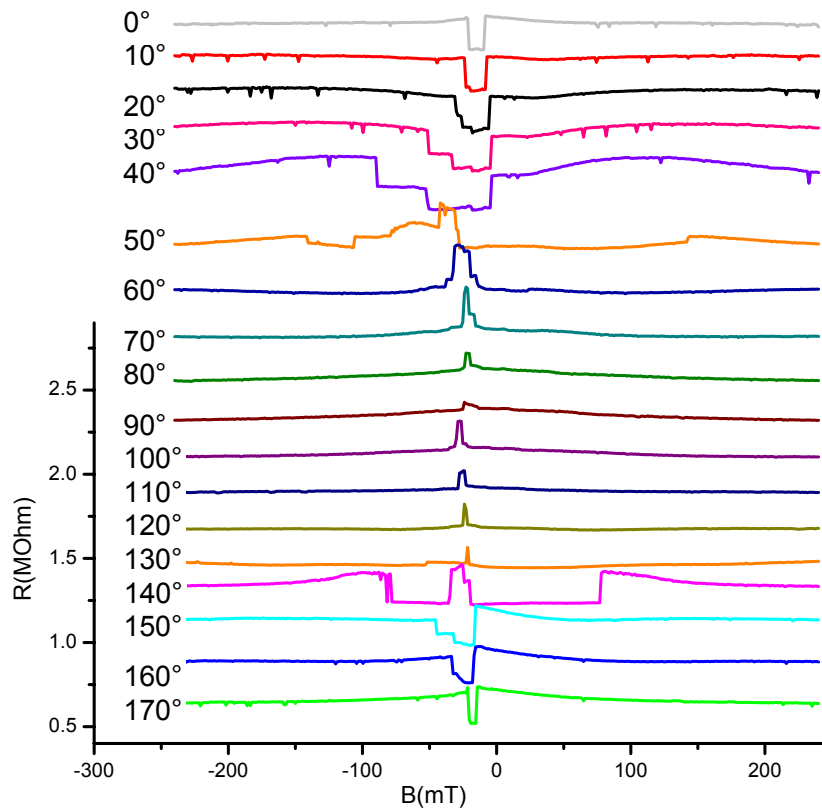
Figure 7.4: Angular dependence of the magnetoresistance. The curves are offset vertically for clarity.

Minor Loops as a Tool to Probe the Magnetic Anisotropy

As pointed out above, the numerous similarities in the magnetoresistance data lead to the assumption that the magnetic anisotropy of each magnetic layer in the sample closely resembles that of the single sided spin valve presented in the previous chapter. The main assertion is that easy axes lie along 0°/[100] and 90°/[010] directions. By measuring appropriate minor loops

of the magnetoresistance it can be shown that both layers have their uniaxial easy axis close to $\phi=90°$, and that the second and slightly less easy axis is along $\phi=90°$. One example of a minor loop measurement is shown in Fig. 7.5. The dotted black curve was taken first while sweeping down from positive to negative saturation along $\phi=30°$. The closest easy axis is thus the one at $0°$. The assumption is that at zero field, the magnetization has settled onto this $0°$ easy axis, and the sample is thus in its high resistance state ($\approx$750 kΩ). Then for small negative fields (-13 mT), a large resistance jump into the low resistance state of the sample ($\approx$500 kΩ) is observed. Interpreted in terms of the TAMR picture, this should correspond to the magnetization switching into the $270°$ direction, which is the global easy axis. Ignoring the fine structure on the peak, the next clear switching event happens at $\approx$-50 mT, bringing the sample back into the high resistance state. From the symmetry of the easy axes and the applied magnetic field one sees that this has to be the $180°$ direction. For clarity, the corresponding geometry is sketched in the inset of Fig. 7.5.
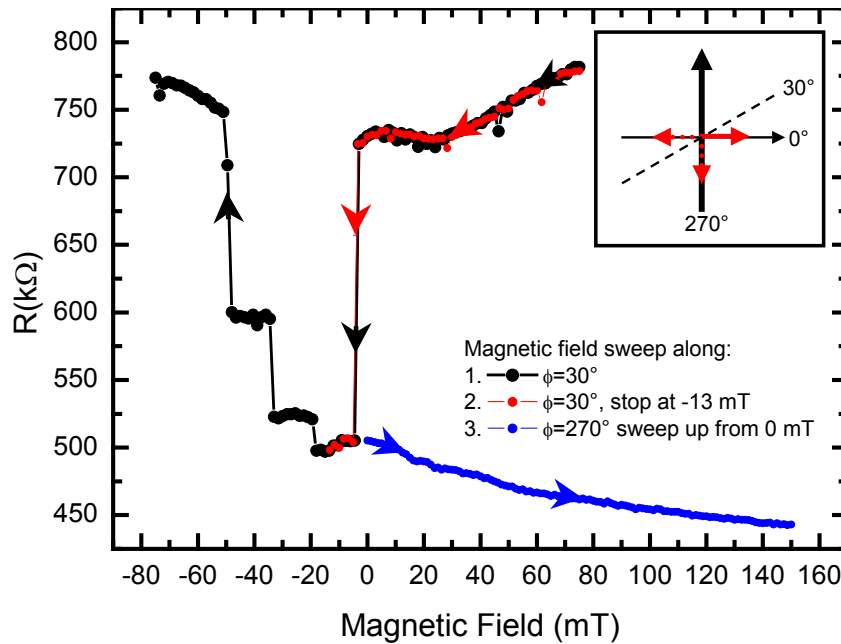
Figure 7.5: Minor loop of the magnetoresistance which is used as a tool to determine the magnetic anisotropy of the device. Black dots: Regular magnetoresistance curve with the magnetic field along $\phi=30°$. Red and blue dots: Minor magnetoresistance loop establishing that $\phi=270°$ corresponds to the global easy axis of both ferromagnetic layers.

The red dotted line is a measurement which initially repeats the regular full $30°$ magnetoresistance scan, except that it was stopped at $\approx$-20 mT. Then the magnetic field was carefully brought back to zero also along $30°$ (not shown). The blue dotted data is the magnetoresistance of the sample while the magnetic field was subsequently increased along the $270°$ degree direction. The fact that no switching event is present in the blue data is consistent with the initial assumptions that in this state, both layer magnetizations already lie along this direction. Hence this direction corresponds to an easy axis of the sample. A careful set of additional minor loops was measured for the easy axis along $0°$, confirming our magnetic model. Further evidence for

this is found below in section 7.4 which reports on the properties of the sample subjected to rotating magnetic fields.

However, despite all the similarities, a further comparison with the single sided spin valve shows that the magnetoresistance of the sample with two magnetic layers is considerably more complex. Besides the obvious fine structure present on top of all spin valve-like features, there no longer exists an angular range where no features at all are observed. This could partly be caused by the fact that the present sample contains two ferromagnetic layers instead of only one. It is very likely that the coercive behavior of the two magnetic layers in the sample differs slightly due to a different thickness and the different conditions at growth start. This would explain a maximum of four switching events per magnetoresistance curve. Additional switching events could come from the presence of multiple domains in either of the layers. It is therefore presently impossible to unambiguously explain each individual switching event by specific and well known switching processes in the two ferromagnets.

7.3.1 Bias Dependence of the Magnetoresistance

The size of the spin valve like signal of the tunnel junction exhibits a very strong voltage dependence, which is displayed in Fig. 7.6. The various curves are magnetoresistance measurements taken along $\phi=60°$ at a temperature of 4.2 K. The excitation voltage ranges from 500 μV up to 10 mV. The low resistance state exhibits a relatively small variation, increasing from 500 kΩ to about 750 kΩ with decreasing bias. In contrast, the high resistance value increases by more than 350% in the same voltage range. The overall peak to valley ratio hence increases with decreasing bias, saturating at a maximum magnetoresistance of 300% for voltages V$\leq$500 μV. It should also be noted that the complexity of the observed features, i.e. the amount of fine structure on top of the main spin valve features increases with decreasing bias. All of the above observations also apply to other directions of the magnetic field, e.g. where an inverted spin valve signal is observed.

7.3.2 Magnetoresistance in Perpendicular Magnetic Fields

Another observation distinguishing the effects observed in the sample from regular Julliere TMR is a strong magnetoresistance signal observed when **H** is applied perpendicular to the plane of the sample, i.e., along the magnetic hard axis. Fig. 7.7 shows such a magnetoresistance scan at T = 4.2 K and V_B = 5 mV. The TAMR in Fig. 7.7 is $\approx$ 400%, much larger than for **H** in plane under similar conditions. As explained later, this is attributed to a significant growth direction strain in the (Ga,Mn)As layers that induces a large anisotropy between the [001] and [100] (or [010]) directions. This out of plane anisotropy is larger than the comparably weak in-plane uniaxial anisotropy distinguishing the [100] and [010] directions. Note also that the perpendicular TAMR is no longer hysteretic, but occurs on both sides of **H**=0, confirming that it must be related to the absolute rather than the relative orientations of the ferromagnetic layers.
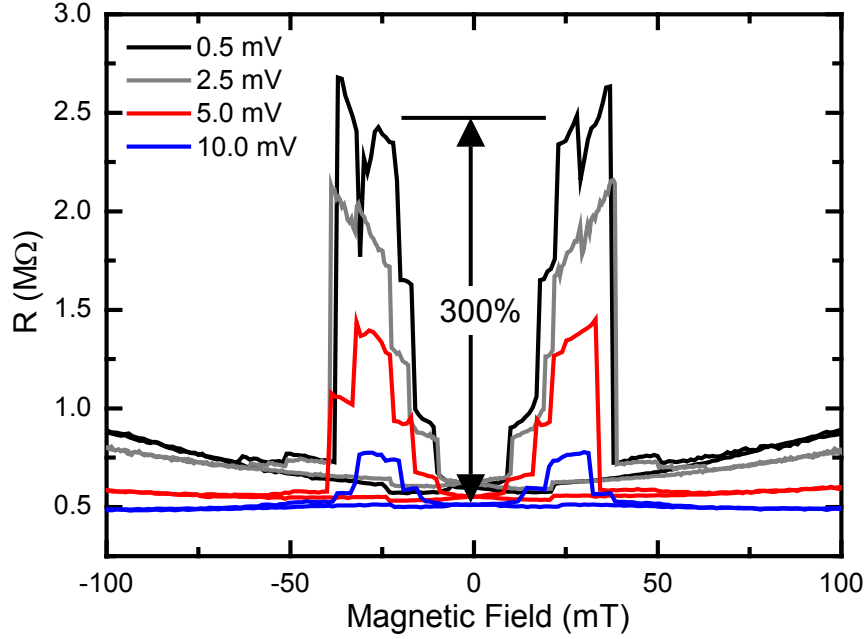
Figure 7.6: Bias dependence of the spin valve like magnetoresistance signal measured at T=4.2 K and ϕ=60°. The sample shows a maximum magnetoresistance of 300%.

7.4 ϕ-Scan Properties at T=4.2 K

A particularly insightful approach to understanding the various transport and magnetic characteristics of the sample is given by the experimental method of measuring ϕ-scans, i.e. by setting a desired magnetic field amplitude and then measuring the resistance while the magnetic field angle is swept. Different characteristics of the sample can be examined by using different magnitudes of the magnetic field.

Here, high magnetic fields can be used to further distinguish the TAMR observed in the sample from regular TMR. Figure 7.8 contains a ϕ-scan measured at T=4.2 K in a magnetic field of $|\mathbf{H}|$ = 300 mT. This field is sufficiently high to saturate the sample magnetization, i.e. the magnetization vectors of both ferromagnetic layers always follow the direction of the external magnetic field ($\mathbf{M} \parallel \mathbf{H}$). Subjected to this kind of experiment, a conventional TMR magnetic tunnel junction would exhibit a constant resistance as a function of ϕ, because it is only sensitive to the relative orientation of layer magnetizations. This is different in TAMR, however, as can already be seen in Fig. 7.3. The resistance at saturation is dependent on the direction of magnetization, roughly varying from 500 to 700 kΩ as the magnetization $\mathbf{M}$ of *both* changes from along [010] to [100]. This sensitivity to the absolute direction of $\mathbf{M}$ is even more obvious from the direct measurement of the ϕ-scan (see Fig. 7.8). Two measurements are shown, recorded at 5 and 10 mV respectively. Because the magnetization is saturated along the external field, the curves are identical for clockwise or counter clockwise ϕ sweeps as $|\mathbf{H}|$ is sufficiently large to saturate $\mathbf{M}$ such that $\mathbf{M} \parallel \mathbf{H}$. In the lower bias curve, the resistance changes by more than 250% between its minimum at 90° and its maximum at 165°. The fact that the maximum resistance does not lie along the main crystal and anisotropy axes will be addressed below. A
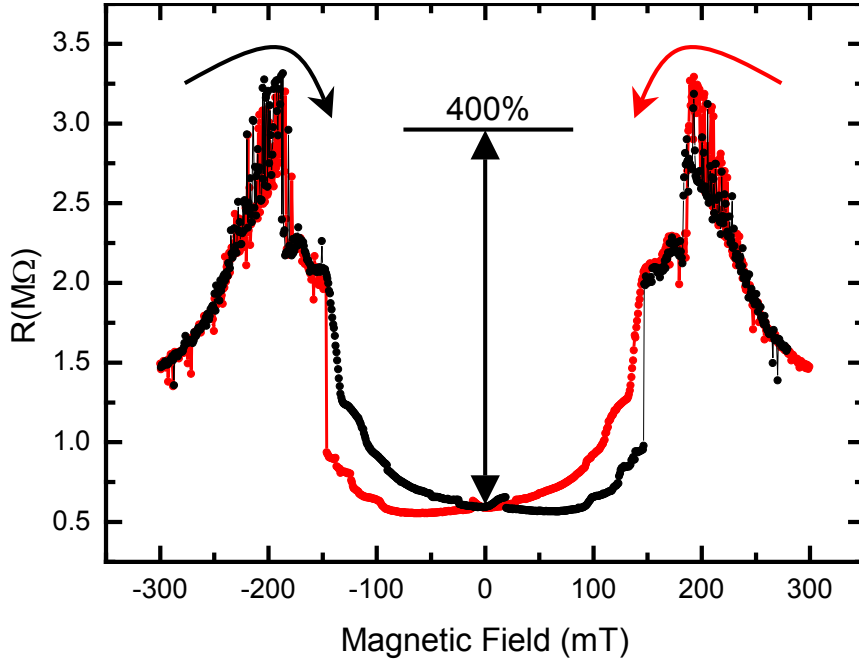
Figure 7.7: Magnetoresistance measurement at T = 4.2 K and V_B = 5 mV measured with the magnetic field applied perpendicular to the plane of the sample. The TAMR in the data is ≈ 400%, much larger than for **H** in plane under similar conditions.

comparison with the 10 mV curve confirms the observation made from the bias dependence of the magnetoresistance along a fixed direction, namely that the high resistance state is strongly affected by bias changes whereas the low resistance state hardly changed.

The shape of the φ-scan changes rather dramatically with |**H**|, especially when fields far below the saturation value are used. This case is shown in Fig. 7.9. Here |**H**|=25 mT was chosen as a field which is just slightly above the highest coercive field observed in the sample. Before the start of the φ-scan, the sample magnetization was prepared in a known state by saturating **M** along the uniaxial easy axis (90°). Subsequently |**H**| was lowered to 25 mT and φ was swept in the clockwise (black curve) or counter clockwise (red) direction.

The main features of the data are ≈ 40% jumps in the resistance between the 500 and 700 kΩ levels. These can be understood rather simply by noting again that at φ = 90° the sample is in a low resistance state associated with **M** being along the [010] easy axis. As φ is swept nearer to the [100] easy axis, **M** will eventually switch to this direction, corresponding to a high resistance state due to the additional uniaxial field that breaks the in-plane fourfold symmetry in the (Ga,Mn)As layers. The curves must be different for the two sweep directions and should have approximate mirror symmetry about the easy axis. The deviations from this symmetry may be attributed to non-uniform strain distributions.

A closer inspection reveals that a few additional resistance levels are seen on the edges of the large switching events, e.g. around φ=25°. These intermediate states can be explained in a straightforward way. By design, the magnetic anisotropies of the two layers are not identical as different strain conditions and thicknesses create different coercive fields. As **H** is rotated,
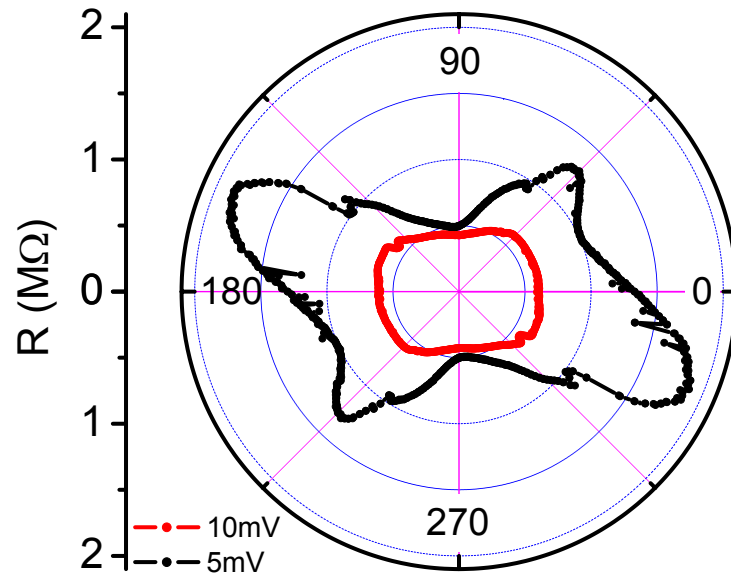
Figure 7.8: ϕ-scans measured at voltages of 5 and 10 mV at T=4.2 K in a rotating saturation magnetic field $|\mathbf{H}|$ = 300 mT. The sample is sensitive to the absolute direction of its magnetization $\mathbf{M}$.
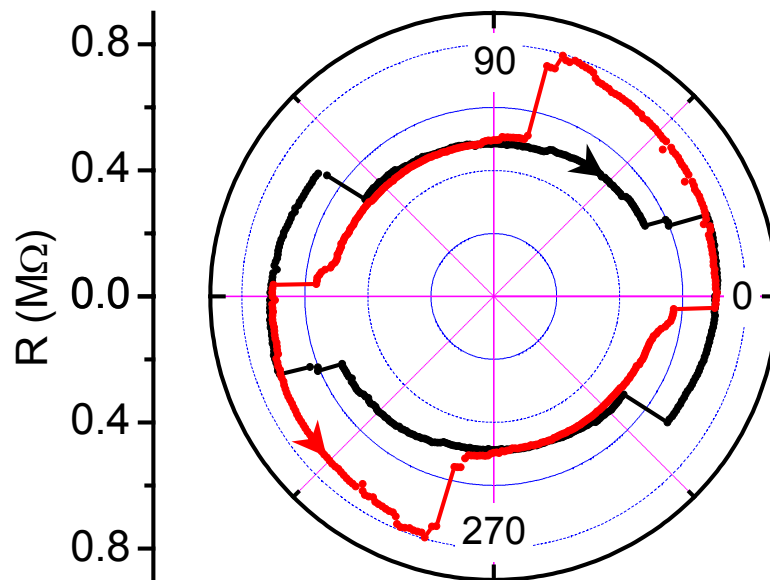
Figure 7.9: ϕ-scans at T=4.2 K in a saturation magnetic field $|\mathbf{H}|$ = 25 mT.

the softer layer switches earlier. This creates configurations where the magnetizations of the two layers are not collinear, but perpendicular to each other. Since the sample is sensitive to the absolute orientation of the ferromagnets, different configurations can correspond to different

resistance states. As a control experiment for the above interpretation, a similar ϕ-scan at $|\mathbf{H}| = 15$ mT was done, and as expected, since 15 mT is below the smallest coercive field in the structure, no switching occurred, and the resistance of the sample remained constant at its lowest value.
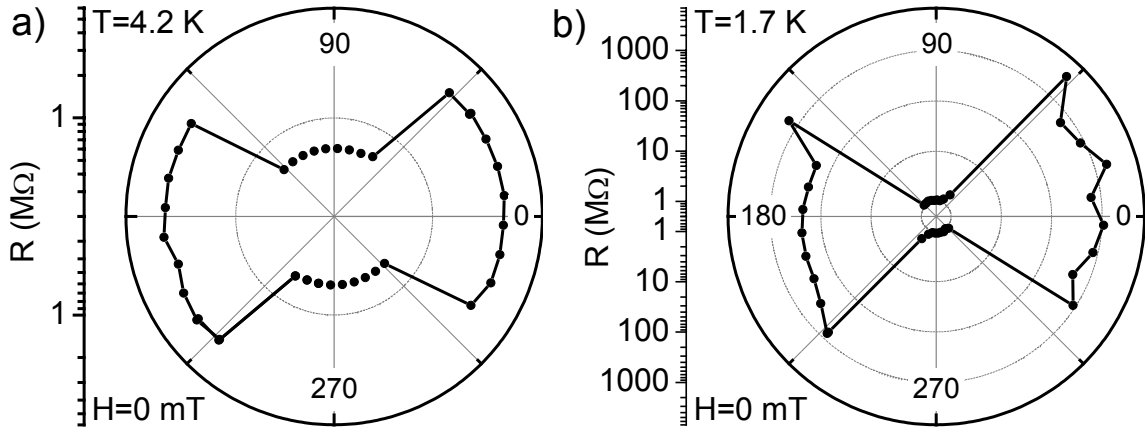
Figure 7.10: Sample resistance at V=1 mV measured at 0 mT after the magnetic state has been prepared by saturating the magnetization with an in plane magnetic field along an angle ϕ. Measurements taken at T=4.2 K (a) and T=1.7K (b). At low temperatures the underlying symmetry is the same as at 4.2K, but there is a giant amplification of the high resistance state. This data directly demonstrates the resistance anisotropy present in the sample.

As a last approach to probing the resistance and magnetic anisotropies of the sample, consider the data presented in Fig. 7.10a, a measurement of the sample resistance at T=4.2 K and V=1 mV. In order to record this data, the magnetic state is first prepared by saturating with a large magnetic field along an angle ϕ. Subsequently the magnetic field is lowered down to zero which causes the magnetization to gradually rotate away from the field direction and to settle along the most energetically favorable magnetic easy axis. The data clearly shows the two level resistance anisotropy associated with the [100] and [010] crystal directions and is thus a direct demonstration of TAMR governing the sample behavior. A comparison of Figs. 7.10a and 6.9 again demonstrates the remarkable similarity between the physical mechanisms governing both the single sided and the double sided TAMR tunnel junctions[1].

7.5   Low Temperature Properties

It was shown above that the sample exhibits a strong bias voltage dependence at T=4.2 K. The magnetoresistance along $\phi = 65°$ exhibits a sixfold increase in magnetoresistance upon a decrease of the voltage by a factor of twenty. The magnetoresistance is however even more sensitive to a reduction of temperature, as demonstrated by the data in Fig. 7.11.

---

[1]Note that the asymmetry with respect to the [010] direction in Fig. 7.10 is not real but an artefact of the large spacing between data points.
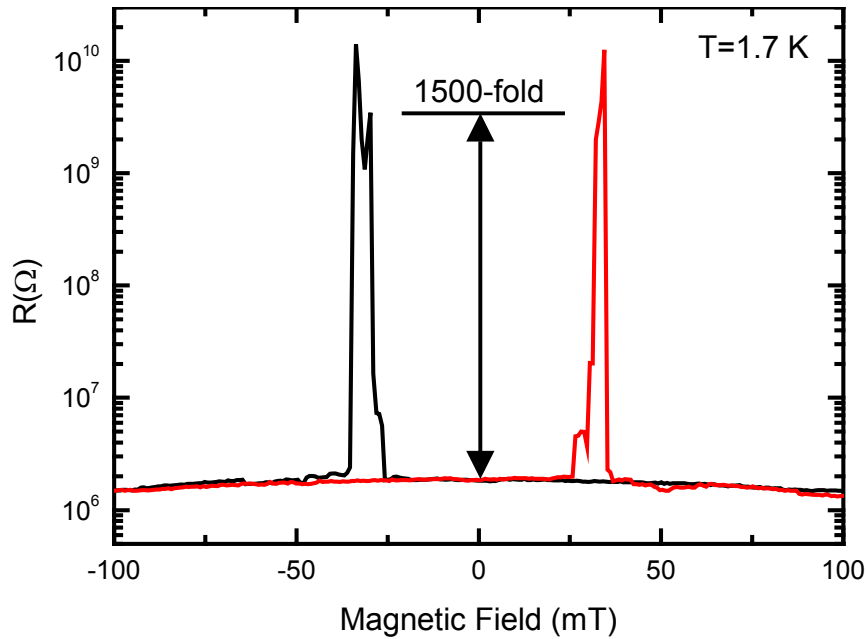
Figure 7.11: The magnetoresistance at low temperature and bias is characterized by a giant amplification of the TAMR effect. The spin valve feature observed along $\phi=60°$ at T=1.7 K and V=1 mV exhibits a magnetoresistance of 150 000%.

Here a V=1 mV magnetoresistance curve at 1.7 K is shown, with the magnetic field applied along $\phi=60°$. Quite remarkably, the reduction of temperature from 4.2 to 1.7 K causes a super giant TAMR signal with a magnetoresistance ratio of 150 000%. Indeed, this is merely a lower limit for the observed magnetoresistance. The amplifier that is used to measure the current through the sample operates at its detection limit in the high resistance state of the sample ($\approx 2 \cdot 10^9$ Ω), which corresponds to a current of only 0.5 pA. Note that this also means that any fine structure that is visible in the high resistance state is likely a measurement artefact.

Although the amplitude of the effect increases dramatically at low V_B and T, the general symmetry remains unchanged. This can be seen from Fig. 7.10b showing a measurement of the sample resistance at T=1.7 K and zero magnetic field. It is clear that M∥[100] and M∥[010] still correspond to the high and low resistance states of the sample, respectively. Aside from the noise present in the high resistance state, this data can be understood as an amplified version of the 4.2 K measurement.

Figures 7.12a to c demonstrate another important characteristic of the tunneling device at low temperatures. Both the ϕ-scans measured at various excitation voltages and in magnetic saturation (B=300 mT) as well as the magnetoresistance with field perpendicular to the plane of the sample exhibit a large number of features. Such fine structure is already present in measurements done at higher temperatures, however it is also vastly amplified at lower temperatures. As will be shown later, both the giant amplification of the magnetoresistance at low temperatures and the abundance of fine structure in the data are most likely caused by additional physical mechanisms influencing the (Ga,Mn)As valence band DOS anisotropy. A likely cause is the opening of a Coulomb gap in the density of states. Due to the different effective masses, the

hole sub-bands be affected differently by the formation of this gap. Since a TAMR device acts as a detector for the anisotropies in the DOS of these hole bands, such a mechanism would be a natural explanation for the giant amplification and fine structure.
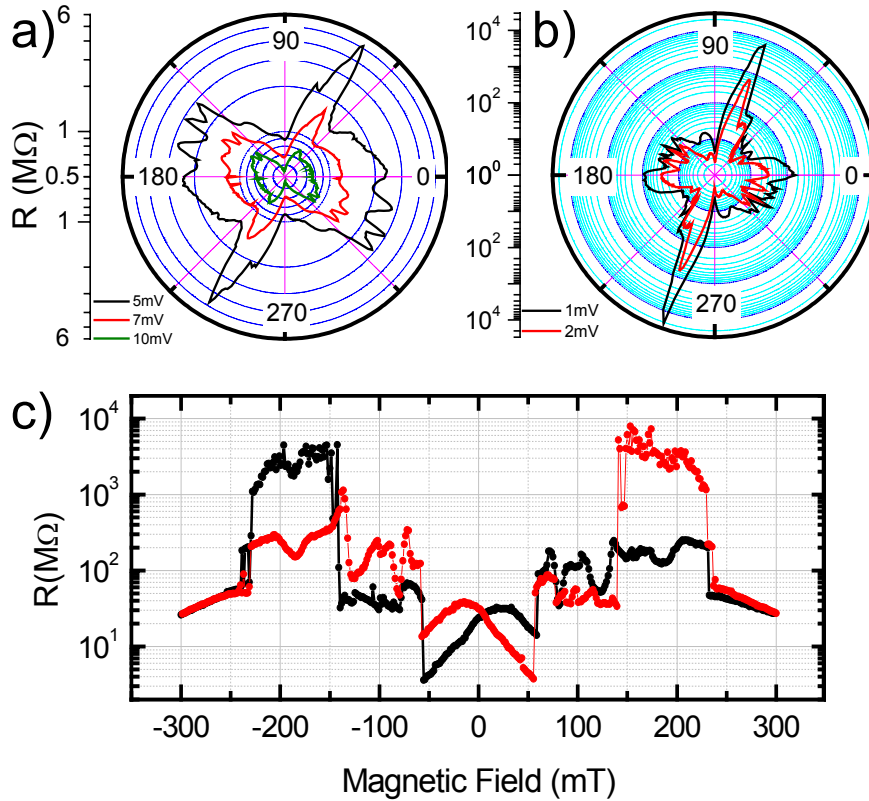
Figure 7.12: (a), (b) ϕ-scans at various excitation voltages at T=1.7 K and B=300 mT. The measurement mirrors the anisotropic density of states of the (Ga,Mn)As. (c) Field perpendicular plane magnetoresistance at T=1.7 K.

7.6 Theoretical Modelling

The data presented above, particularly the sample characteristics displayed in Figs. 7.3 and 7.10 establish unambiguously the TAMR nature of the measured effect. TAMR is caused by anisotropies in the (Ga,Mn)As density of states with respect to **M**. They result from the strong spin-orbit coupling in the ferromagnetic semiconductor valence band, and were shown in the previous chapter to explain the 3% magnetoresistance observed in a single ferromagnet device with a polycrystalline tunnel barrier. Furthermore these DOS anisotropy calculations, which are based on the kinetic-exchange model coupling of valence band holes and polarized Mn local moments, have explained the change of the sign of the TAMR spin-valve like signal with field angle and temperature which were observed in this sample. The model outlined in section 6.7.2 predicts that a strong enhancement of the TAMR effect (of up to a few 100%) can take place in

epitaxial tunnel junctions characterized by a larger degree of in-plane momentum conservation.

The high temperature (4.2 K) experimental evidence collected on the double layer sample is consistent with this prediction. Furthermore it will be shown below that the higher magnitude of the effect at 4.2 K as well as some of the new experimental features of the (Ga,Mn)As/GaAs/(Ga,Mn)As TAMR can be understood based on DOS anisotropies in (Ga,Mn)As. All of the required numerical simulations were conducted by T. Jungwirth and J. Sinova on the basis of the model of carrier mediated ferromagnetism in (Ga,Mn)As presented in [Abo01]. The modelling follows a similar line of reasoning as before, however special attention was paid to correctly model the details of the low-temperature GaAs tunnel barrier.

The theoretical anisotropies in the density of states for a single (Ga,Mn)As layer are displayed in Fig. 7.13 for several in-plane magnetization orientations. The quantity $\Delta DOS_{int}/DOS_{int}$ which is plotted on the y-axis, is the relative change of the integrated density of states upon a switch of the magnetization direction from the $\phi=270°$ uniaxial easy axis to one of the angles specified in panel (a) of the figure. DOS_{total} denotes the total DOS at E_F and the integrated density of states DOS_{int} is obtained by integrating over an assumed range of momenta k_z along the tunneling direction and subsequently summing over all occupied spin-split valence bands. The x-axis represents the integrated DOS at the Fermi energy that is assumed to contribute to tunneling, relative to the total DOS at the Fermi energy. Note that the states at the Fermi energy with the largest k_z are expected to have the largest tunneling probability when in-plane momentum is conserved. Therefore, increasing the range of k_z contributing to the tunneling DOS corresponds to relaxing the in-plane momentum conservation condition, or increasing the tunnel barrier transparency.

The second parameter which is varied in the calculation of the DOS anisotropies is the carrier concentration at the interface with the tunnel barrier. The carrier concentration has a profound effect on the transport and magnetic characteristics of the (Ga,Mn)As electrodes and therefore ultimately on the overall device performance. The importance of the hole density comes from the fact that in carrier mediated ferromagnetism the level of occupation of the valence bands determines the anisotropy of the Fermi surface and ultimately also the magnetic anisotropy of the (Ga,Mn)As [Abo01]. We expect that although the bulk hole densities in the (Ga,Mn)As layers are of order 10^{20} cm^{-3}, the carrier concentration near the tunnel barrier interface is lower. The reason for this lies within the electrical properties of the barrier material, which is a low temperature grown GaAs (LT-GaAs) layer. LT-GaAs is known to contain a large number of As$_{Ga}$ antisite defects that create a band of donor states near the middle of the GaAs gap [Fee93]. The midgap states have two important consequences. Firstly the Fermi energy in the GaAs is pinned in the middle of the gap, making it a good barrier material in combination with (Ga,Mn)As. Secondly, the donor states can partially deplete the surrounding (Ga,Mn)As, thereby changing the effective carrier concentration. We expect the depletion at the interface to be significant, with hole concentrations close to those in panels 7.13a or b. The substitutional Mn$_{Ga}$ concentration of 4% considered in the calculations is consistent with the nominal total Mn doping in the (Ga,Mn)As layers. A uniaxial strain along [010] was again introduced to model the broken in-plane fourfold symmetry in the (Ga,Mn)As.

The results of the simulations shown in Fig. 7.13 demonstrate that the magnitude of the DOS_{int} anisotropy as well as the magnetization orientations corresponding to extremal tunneling DOS have a complex dependence on the magnetic tunnel junction parameters. Data in panel (a), e.g., show DOS_{int} anisotropies exceeding 100% for $DOS_{int}/DOS_{total} \sim 10\%$. Here
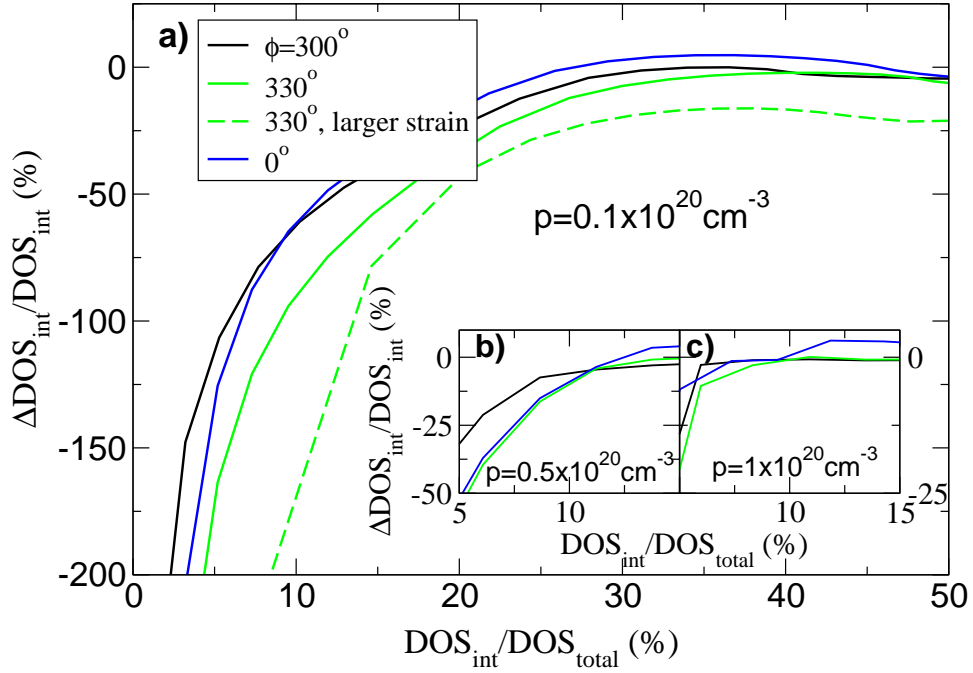
Figure 7.13: Theoretical diagrams obtained for hole densities 0.1 (a), 0.5 (b), and $1 \cdot 10^{20}$ cm^{-3} (c) showing the relative difference between the integrated DOS at the Fermi energy for **M** along $\phi = 270°$) and three different angles ϕ. The x-axis represents the integrated DOS at the Fermi energy that is assumed to contribute to tunneling, relative to the total DOS at the Fermi energy. Solid (dashed) lines were obtained for a uniaxial strain along [010] direction of 0.2% (0.4%).

the minimum DOS$_{int}$ is for **M** at $\phi = 270°$ while the maximum DOS$_{int}$ is at $\phi = 330°$, i.e., off the main crystal and magnetic anisotropy axis. The result provides an explanation for the distorted fourfold symmetry observed in Fig. 7.8a. The enhanced DOS anisotropy shown by the dashed line in the main panel, which was obtained for larger strain value (larger magnetic anisotropy), is consistent with the experimentally observed enhancement of the TAMR when magnetization is switched between the uniaxial easy and hard-axis. It should be emphasized, however, that the theoretical data in Fig. 7.13 are only illustrative; a more quantitative comparison between the experiment and theory requires a detailed characterization of the experimental tunnel junction and a systematic theoretical analysis of the TAMR and TMR contributions to the hole transmission coefficients. The main point of the calculations, however, remains valid: the pure DOS anisotropies which are presented are large enough to explain the order of magnitude of the effects observed at 4.2K.

Another result of these calculations is consequently that in order to explain the giant amplification of the effect to 150 000% that is observed at 1.7K, additional physical mechanisms have to be considered. This aspect of the behavior of the sample is not well understood. However, it is possible that the large amplification of TAMR can be understood as a manifestation of a well-known zero bias anomaly [Lee99] in tunneling from a dirty metal which appears due to the opening of an Efros-Shklovskii gap [Efr75] at the Fermi energy of (Ga,Mn)As when it locally crosses the metal-insulator transition.
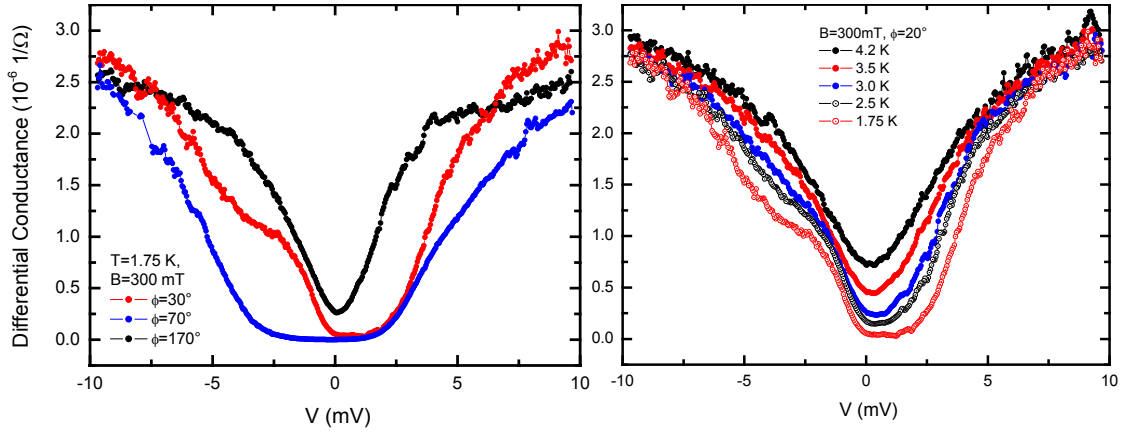
Figure 7.14: Examples of low temperature (T=1.75 K) conductance spectra at different angles exhibiting several qualitatively different shapes (left); Temperature dependence of a conductance spectrum at $\phi=20°$ (right);

A few representative low temperature conductance spectra of the sample are displayed in Fig. 7.14. The right panel shows a temperature dependent measurement in which strong features are developed with decreasing temperature while the zero bias resistance increases by three orders of magnitude. A multitude of features is observed at these low temperatures. Perhaps most surprising is that the current-voltage characteristics of the sample can even be symmetric as well as asymmetric, depending on the direction of the magnetization. Despite this richness of observations, two main patterns are commonly observed and given by the black and the blue curve in the left panel. They bear some resemblance with conductance spectra measured on Si:B samples that are doped at various concentrations above and below the metal-insulator transition [Lee99]. The authors explain the power laws governing the Si:B conductance spectra by a model assuming a Coulomb gap in the density of states on the insulating side.

Indeed, such an effect is conceivable in the sample, given the short (Ga,Mn)As mean free path of a few Å which limits the effective injector region to a very thin layer near the barrier. Depletion near the barrier can therefore cause a lower carrier density in the injector region than in the bulk of the (Ga,Mn)As slab. We take the injector as the point where depletion causes the valence band edge to drop beneath the Fermi level. Hence the injector will be much closer to the metal-insulator transition than a typical (Ga,Mn)As layer. Moreover, it is known that the DOS changes with **M**. Therefore, when experiments are performed at low V_B and T, the effective DOS participating in the tunneling can be brought through the metal-insulator transition with reorientation of **M**, which could in turn lead to a large amplification of the TAMR effect.

A further indication that the Efros-Shklovskii gap is the dominant enhancing mechanism is that the amplification of the effect, as T changes from 4.2 to 1.7 K, is strong for low bias voltage (1 mV) but disappears at higher voltages (10 mV). This is also seen from the convergence of the curves in the left panel of Fig. 7.14 and consistent with the experimental results of [Lee99]. Other possible mechanisms for the enhancement of the TAMR, such as disorder and impurity mediated tunneling, may also play a role and should not be summarily dismissed. Further study is clearly needed before the amplification mechanism can be claimed to be fully understood.

7.7 Device Applications

A number of potential applications exist for TAMR based devices. In some of these applications TAMR is in direct competition with devices based on other magnetoresistive mechanisms such as GMR or TMR. However it has the potential advantage that a spin valve feature is already obtained with only one ferromagnetic layer instead of two. Actual devices based on GMR or TMR are operated with one layer acting as a "polarizer" and the other one as a "detector" for spin carriers. Thus the necessity arises to artificially pin the polarizer magnetization along a desired direction using antiferromagnetic coupling to an additional magnetic multilayer. In comparison, TAMR based devices could be produced at smaller cost, as they would neither need the second ferromagnetic layer nor the associated artificial antiferromagnet. In addition, TAMR features novel spintronics functionalities from which potential benefits for many fields of applications arise.

Magnetic Field Sensor

The most basic application of a TAMR tunnel junction is a magnetic field sensor. In TAMR there is a direct correlation between the absolute orientation of the magnetization of each ferromagnetic layer in the sample and its resistance. Thus, unlike in TMR there exists a sensitivity to the absolute direction of an external magnetic field. This functionality, demonstrated in Fig. 7.8, is for example useful for angular velocity sensors commonly employed in the automotive industry.

Current Switch

Decreasing the off-state current of integrated circuits is currently one of the most important design objectives in the field of battery-powered mobile computing and communication devices. From Fig. 7.11 it can be seen why TAMR could have possible advantages over existing technologies. The displayed magnetoresistance ratio exceeds 150 000%, and, since the corresponding measurement was conducted in constant voltage mode, the current flowing during the measurement decreases by more than three orders of magnitude between the on and the off state. In fact it is not clear how large the off state current really is. The upper limit I=0.5 pA is given by the limitations of the measurement equipment and therefore it seems possible that optimized TAMR devices can act as a very efficient ON/OFF switches for electric currents.

Magnetic Read Head

As a magnetic field sensor with a large magnetoresistance ratio a TAMR junction is a promising candidate for the inclusion into next-generation read heads of magnetic hard disk drives. Currently available read heads are based on GMR multilayers. Their comparably low magnetoresistance ratios ultimately limit the achievable information storage density. This problem could be overcome by employing TAMR tunnel junctions instead.

Multiple Bit Memory Cell

TAMR can be readily integrated into the presently existing data storage schemes for magnetic random access memory (MRAM) (see Fig. 6.1). In the simplest possible case, binary information can be encoded into the two intrinsic resistance levels of a single sided spin valve, i.e. "HIGH R=1" and "LOW R=0". Higher integration densities are possible when more than one ferromagnetic layer is used, as is demonstrated in Fig. 7.15. The graph shows a high angular resolution ϕ-scan (B=0 mT) measured in the transition region between the high and the low resistance state of a TAMR junction containing two (Ga,Mn)As layers. The measurement shows the existence of an intermediate resistance state that corresponds to a relative angle of $90°$ between the two magnetizations. All three states are stable in zero external field and thus appropriate for nonvolatile information storage. This would allow for the design of multiple bit memory cells that can not be realized using regular TMR junctions.
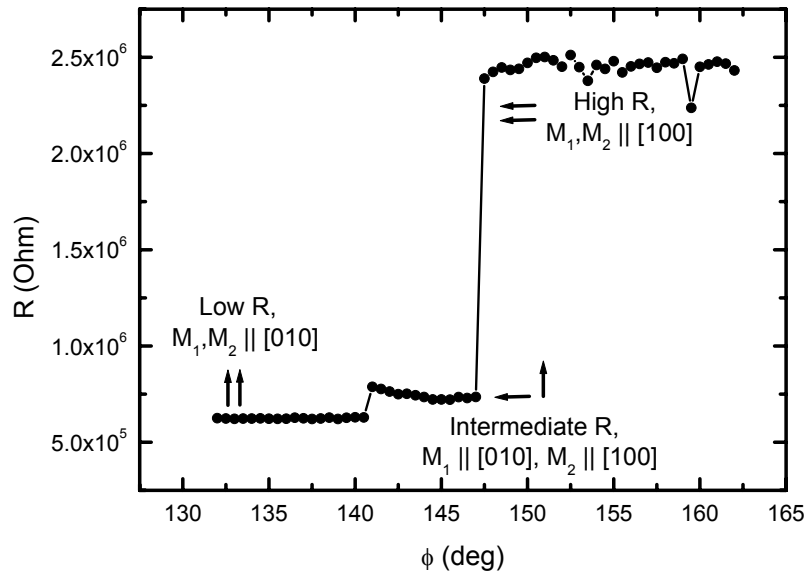
Figure 7.15: High angular resolution ϕ-scan (B=0 mT) measured in the transition region between the high and the low resistance state of the TAMR junction with two ferromagnetic (Ga,Mn)As layers. The measurement demonstrates the existence of an intermediate resistance state that corresponds to a relative angle of $90°$ between the two magnetizations.

Remaining Challenges

It should however be noted that using (Ga,Mn)As, all of the above mentioned applications are presently only possible in a low temperature, i.e. laboratory environment. Of course, the ultimate prerequisite that needs to be fulfilled for the realization of commercial applications is room-temperature ferromagnetism in (Ga,Mn)As. However, given that the effect depends on characteristics of the band structure, it is reasonable to assume that other material possibilities exist. Promising candidates are room-temperature ferromagnets which exhibit strong spin-orbit coupling.

7.8 Summary

In summary, a super-giant TAMR effect was observed in a (Ga,Mn)As/GaAs/(Ga,Mn)As tunnel structure which can be of order of a few hundred percent at 4K, and can be amplified to 150 000% at lower temperatures. The behavior of the structure not only mimics normal TMR when the field is applied along the [010] direction, but also exhibits new functionalities such as a sensitivity to not only the amplitude, but also to the direction of an applied magnetic field. While many of the experimental features of this novel effect can be understood through the one-particle tunneling DOS anisotropies with respect to the magnetization orientation, the dramatic amplification at low biases and temperatures poses new challenging questions for the theory of tunneling transport in disordered interacting electronic systems with strong spin-orbit interaction.

Chapter 8

Summary

Modern magnetic high density data storage devices are based on magnetic field sensors involving metallic micro-fabricated ferromagnetic thin films. State of the art in hard disk drives is the usage of the giant magnetoresistance (GMR) [Bai88, Bin89, Bar90] effect in read heads. In GMR devices, ferromagnetic metal thin films are separated by nonmagnetic metallic spacers. Future generations might utilize the tunneling magnetoresistance (TMR) [Jul75] effect in order to obtain even higher densities of information integration. TMR devices consist of ferromagnetic metal layers as well, however the metallic spacer is replaced by a tunnel barrier. In addition to this already existing multi-billion dollar market, intensive academic and industrial research is devoted to the development of nonvolatile, low access time, high durability magnetic random access memory (MRAM). MRAM would allow the synthesis of nonvolatile data storage and data processing in a single device. Fuelled by this considerable commercial and also a large scientific interest, the development of heterostructures based on ferromagnetic metals has been very rapid. Despite this, some fundamental limitations remain. Magnetic properties of metals are not tunable and integration into semiconductor devices is difficult.

The novel field of spintronics tries to circumvent some of these problems by developing materials and devices that have ferromagnetic as well as semiconducting properties. In this respect, several successes have been achieved so far. Among the most promising and well understood materials is (Ga,Mn)As, a random alloy of the transition metal Mn with the III-V semiconductor GaAs [Ohn98]. Carrier mediated ferromagnetism in (Ga,Mn)As is well understood [Abo01, Die01b] and the pd-interaction between the hole carriers and the localized Mn magnetic moments is responsible for a strong interplay of magnetic and transport properties. As a strongly spin-orbit coupled material (Ga,Mn)As holds the potential to exhibit novel spintronics effects not obtainable in ferromagnetic metal systems.

This work is a study of spin valve-like magnetoresistance effects in lateral and vertical (Ga,Mn)As based ferromagnetic semiconductor junctions. The lateral geometry was used to investigate the electrical resistivity of domain walls in (Ga,Mn)As. For this purpose, we have fabricated (Ga,Mn)As nanostructures with constrictions. Controlled by shape anisotropy and strong pinning of domain walls, we can switch the regions on either side of the constriction to either parallel or antiparallel magnetization. In the antiparallel case, domain walls are present in the constrictions, enabling us to measure their resistivity. In order to be able to unambiguously eliminate bulk contributions to the magnetoresistance, a key objective was to find a way to maximize the domain wall resistivity. Here, special attention was paid to the model of the

unipolar spin diode proposed by M. E. Flatté and coworkers [Fla01, Vig02]. The proposed spin diode consists of two adjacent layers with antiparallel majority carrier spin polarization. One possible experimental realization of this device is consequently a magnetic DW between regions of opposite magnetization. One of Flatté's results is that in order to maximize the domain wall resistivity, the domain wall should be thin enough that the spin of a passing carrier is not able to precess significantly. In order to minimize the domain wall thickness, we pin the domain walls by sub-10 nm constrictions. In accordance with a model proposed by Bruno [Bru99] we find that in this case the length of the constricted domain walls is determined by the details of the constriction geometry and not by the intrinsic anisotropies of the host ferromagnet. Such a constricted wall constitutes a novel class of domain walls, whose properties are quite different from those of conventional Bloch or Néel walls.

In the range of investigated constriction samples, both the diffusive and the tunneling transport regime were observed in the constrictions. Samples in all cases show clear spin valve like magnetoresistance with up to 8 % positive MR in the diffusive regime and 2000 % positive MR in the tunneling magnetoresistance. In the diffusive regime we find that we can explain the order of magnitude of the domain wall resistance with the expression of Valet and Fert [Val93] for the spin-accumulation-induced resistance at an abrupt junction between two regions of opposite magnetization. In the tunneling case we identify depletion due to dry etching as the cause for the formation of shallow parabolic barriers in the narrow constrictions between the two (Ga,Mn)As regions. Mathematically, our tunneling model is based on the expression for the transmission coefficient through parabolic tunnel barriers, which depends on the barrier width in an exponential fashion. A key element of this analysis is that the minority and majority carriers deplete at different positions in the constriction. Using material parameters that fit well with the bulk material properties and a value for the spin polarization in the material obtained from the diffusive regime we reproduce the observed 2000% magnetoresistance.

The remaining part of this work is an investigation of vertical tunneling heterojunctions of (Ga,Mn)As. A new class of spintronics device is introduced in the form of a Au/AlOx/ (Ga,Mn)As tunnel junction. Based on evidence coming from detailed magnetotransport studies with the magnetic field being applied along various angles ϕ in the plane of the ferromagnetic thin film, we report the surprising result that a spin valve-like magnetoresistance is found using a single ferromagnetic (Ga,Mn)As thin film. This novel magnetoresistive effect is called tunneling anisotropic magnetoresistance (TAMR). A comparison of magnetoresistance measurements with field at different angles reveals that the width and also the sign of the observed spin valve-like feature follow a very regular pattern with respect to the magnetic field angle ϕ. The magnitude of the effect remains constant at $\approx 3\%$ irrespective of whether positive or inverted spin valve-like features are observed. We identify that the spin valve feature is a product of the interplay of the anisotropic density of states in (Ga,Mn)As with respect to the magnetization direction and the two step magnetization reversal in the material. A key characteristic of the TAMR effect is that the sample resistance depends on the absolute direction of the magnetization vector **M**. For example, **M** parallel to the [010] magnetic easy axis corresponds to a low sample resistance state and **M** parallel to the [100] axis, which is slightly less easy, corresponds to a high sample resistance. A spin valve-like feature arises when the magnetization switches between the two easy axes during a magnetoresistance sweep.

We explain our results on the basis of a separate modelling of the magnetic and resistance anisotropies existing in the sample. The magnetic anisotropy has a fourfold contribution along

the [100] and [010] directions. Superposed is a small uniaxial contribution favoring the [010] direction. We are able to quantitatively fit the location of the coercive fields in the sample using a simple phenomenological model of domain wall assisted switching.

To explain the anisotropy of the tunneling resistance, we turn to an analysis of the electronic density of states in the valence band of (Ga,Mn)As. The analysis is based on a calculation of the electronic structure of (Ga,Mn)As by T. Jungwirth. The model includes biaxial in-plane strain and an additional phenomenological in-plane uniaxial strain term of order 0.1% to break symmetry between the [100] and [010] directions. This strain is responsible for sizable anisotropies in the density of states (DOS) of the (Ga,Mn)As that contribute to the tunneling current. Here the size of the effect is predicted to depend very sensitively on material parameters like carrier concentration and strain as well as the quality of the tunnel barrier. The effect of the tunnel barrier is to select a specific anisotropic subset of the DOS which dominates the tunneling current. The mechanism through which this happens is in-plane momentum conservation of the hole carriers: In general a tunneling current is dominated by carriers with momentum vectors near-normal to the barrier, because the tunneling probability decreases rapidly when the momentum deviates from the barrier-normal direction. In other words this mechanism results in a higher probability of tunneling for states with higher band and barrier-normal momentum indices. The calculations indicate that larger effects are expected for cleaner or respectively epitaxial tunnel barriers.

This prediction is tested and confirmed in the final part of the thesis dealing with TAMR in a fully epitaxial (Ga,Mn)As/GaAs/(Ga,Mn)As vertical tunnel junction. Again, both normal and inverted spin valve-like signals are observed in magnetoresistance, with a maximum magnitude of 300% at T=4.2 K and low bias. The symmetry of in-plane measurements closely resembles the one observed in the single sided spin valve with **M** parallel to the [010] magnetic easy axis corresponding to a low sample resistance and **M** parallel to the [100] axis corresponding to a high sample resistance. This is strong evidence of TAMR being the dominant magnetoresistive mechanism. Additionally, applying a rotating in-plane magnetic field that is sufficiently large to saturate both layer magnetizations, also generates a magnetoresistance on the order of a few 100%. This is direct evidence that Julliere-like tunneling magnetoresistance is not observed in our magnetic tunnel junction since in a conventional TMR tunnel junction the resistance would remain constant at all times during this experiment. The total absence of any signatures of regular TMR also suggests that previously published spin valve results in (Ga,Mn)As [Hig01] possibly have to be re-evaluated in the light of TAMR. In addition to the large effect present in the sample at 4.2 K, a giant amplification to 150 000% is observed in measurements done at lower temperatures (1.7 K). Here a detailed investigation shows that the underlying symmetry of the effect is unchanged by the lower temperature and therefore suggests that the TAMR effect is amplified by an additional mechanism at low temperatures. A calculation of the (Ga,Mn)As density of states in the valence band confirms that the intrinsic anisotropies are large enough to explain a magnetoresistance on the order of a few 100%. Modelling for the large amplification observed at low temperatures is still ongoing with the most likely cause being the opening of an Efros-Shklovskii gap [Efr75] at the Fermi energy of the (Ga,Mn)As.

Using the TAMR effect it is not only possible to mimic normal TMR, but TAMR also exhibits new functionalities such as a high sensitivity not only to the amplitude, but also to the direction of an applied magnetic field. Consequently a number of potential device applications,

e.g. in the fields of magnetic sensing and data storage exist for TAMR based devices. Using (Ga,Mn)As however, all of the proposed devices can presently only work at low temperatures. Drawing conclusions from the origin of TAMR in (Ga,Mn)As, the search for suitable materials should start with strongly anisotropic room-temperature ferromagnets where carriers experience strong spin-orbit interaction.

Chapter 9

Zusammenfassung

Um eine hohe Informationsdichte zu erreichen, werden in der aktuellen Generation magnetischer Datenspeicher Magnetfeldsensoren verwendet, die aus dünnen Schichten metallischer Ferromagneten aufgebaut sind. Der Stand der Technik bei Leseköpfen in Festplattenspeichern ist die Verwendung des Giant Magnetoresistance (GMR) Effekts [Bai88, Bin89, Bar90]. GMR-Bauteile bestehen aus zwei oder mehr ferromagnetischen Schichten, die durch nichtmagnetische, leitende Schichten voneinander getrennt sind. Zukünftige Generationen von Bauteilen könnten eventuell auf den Tunnel Magnetoresistance (TMR) Effekt [Jul75] zurückgreifen, um noch höhere Speicherdichten zu erreichen. TMR Bauteile enthalten ebenfalls ferromagnetische Schichten, jedoch sind diese durch nichtmagnetische Tunnelbarrieren voneinander getrennt. Sowohl akademische als auch industrielle Forschungsgruppen arbeiten derzeit an der Entwicklung von Magnetic Random Access Memory (MRAM), einer schnellen, nichtflüchtigen und langlebigen Speicherart, die Absatzmärkte in Milliardenhöhe erschließen könnte. MRAM würde das gleichzeitige Speichern und Verarbeiten von Informationen in einer einzigen Baugruppe erlauben. Vorangetrieben von diesem immensen kommerziellen und auch wissenschaftlichen Interesse hat sich die Technologie der auf ferromagnetischen Metallen basierenden Heterostrukturen rapide fortentwickelt. Trotzdem weist diese Technologie eine Reihe fundamentaler Beschränkungen auf: die magnetischen Eigenschaften von Metallen sind nur schlecht beeinflußbar und der Einbau in Halbleiterbauelemente ist schwierig.

Das neuartige Forschungsgebiet der Spintronik versucht einige dieser Probleme durch die Entwicklung von ferromagnetischen Halbleiter-Materialien zu umgehen. Erste Erfolge wurden hierbei unter anderem durch die Verwendung von (Ga,Mn)As erzielt [Ohn98]. (Ga,Mn)As ist eine Verbindung des III-V Halbleiters GaAs mit dem ferromagnetischen Übergangsmetall Mn. Der in diesem Material auftretende ladungsträgervermittelte Ferromagnetismus ist mittlerweile gut verstanden [Abo01, Die01b] und die pd-Austauschwechselwirkung zwischen den Loch-Ladungsträgern und den lokalisierten magnetischen Momenten des Mn sorgt für ein komplexes Wechselspiel der magnetischen und elektrischen Eigenschaften. Die starke Spin-Orbit Kopplung der Ladungsträger ermöglicht das Auftreten neuartiger spintronischer Effekte, die mit ferromagnetischen Metallen nicht oder nur bedingt reproduzierbar sind.

In dieser Arbeit werden Untersuchungen von spinventilartigen Magnetowiderstandseffekten präsentiert, die an lateralen und vertikalen ferromagnetischen Halbleiter-Heterostrukturen durchgeführt wurden. In allen Fällen wurde (Ga,Mn)As als magnetisches Material verwendet. In der lateralen Geometrie wurde der elektrische Widerstand von Domänenwänden in

(Ga,Mn)As untersucht. Zu diesem Zwecke wurden (Ga,Mn)As Nanostrukturen mit Einschnürungen hergestellt. Es wird demonstriert, dass die Bereiche links und rechts der Einschnürungen sowohl parallel als auch antiparallel ausgerichtet werden können. Dies wird erreicht durch das Zusammenwirken von magnetischer Formanisotropie und durch Einfangen von Domänenwänden in den Einschnürungen. Im antiparallelen Zustand befinden sich Domänenwände in den Einschnürungen. Dies ermöglicht die Messung des elektrischen Domänenwandwiderstandes. Es ist hierbei unbedingt nötig, den Domänenwandwiderstand zu maximieren, weil es dann möglich ist, unerwünschte Magnetowiderstandseffekte wie den anisotropen Magnetowiderstand in (Ga,Mn)As zu eliminieren. Zu diesem Zweck wurde das Modell der unipolaren Spindiode von M.E. Flatté et al. besonders berücksichtigt [Fla01, Vig02]. Die hier vorgeschlagene Spindiode besteht aus zwei benachbarten Schichten mit unterschiedlicher Spinpolarisation der Majoritätsladungsträger. Eine mögliche experimentelle Realisierung ist hierbei eine magnetische Domänenwand zwischen zwei Regionen antiparalleler Magnetisierung. Ein wichtiges Resultat dieser Theorie ist, dass dünnere Domänenwände einen höheren Widerstand aufweisen. Die Wand muss hierbei so dünn sein, dass ein die Wand ballistisch durchfliegender Spin keine signifikante Präzession erfährt. Um die Größe der Wand zu beeinflussen, werden die Domänenwände beim Durchlaufen der Transportstruktur in den unter 10 nm großen Einschnürungen festgehalten. In Übereinstimmung mit einem Modell von Bruno [Bru99] wird in diesem Falle beobachtet, dass die Länge der eingeschnürten Domänenwände von der Geometrie der Transportstruktur bestimmt wird und nicht von den magnetischen Eigenschaften des (Ga,Mn)As. Eingeschnürte Domänenwände stellen eine völlig neue Klasse von Domänenwänden dar. Ihre Eigenschaften unterscheiden sich deutlich von denen konventioneller Bloch oder Néel Wände.

Die Serie der untersuchten Proben enthielt sowohl Proben mit diffusivem als auch solche mit Tunneltransport in den Einschnürungen. Alle diese Proben weisen einen klar spinventilartigen, rechteckigen Verlauf des Magnetowiderstandes auf. Der maximal beobachtete positive Magnetowiderstand beläuft sich auf 8% im diffusiven Transportregime und auf 2000% im Falle von Tunneltransport. Die Größenordnung des Effektes im diffusiven Regime wird mit einem Modell von Valet und Fert [Val93] erklärt, welches die Erhöhung des Widerstandes auf eine Spinakkumulation an der Grenzschicht zweier antiparalleler Domänen zurückführt. Die theoretische Modellierung des Tunnelfalls zeigt, dass die Ladungsträgerverarmung durch das verwendete Trockenätzverfahren zur Bildung flacher, parabelförmiger Tunnelbarrieren in den Einschnürungen führt. Die mathematische Formulierung dieses Modells basiert auf dem Ausdruck für den Transmissionskoeffizienten durch parabelförmige Barrieren. Dieser hängt exponentiell von der Barrierendicke ab. Ein wichtiger Aspekt der Argumentation ist weiterhin dass Minoritäts und Majoritätsladungsträger bei paralleler und antiparalleler Ausrichtung der Magnetisierung unterschiedliche effektive Barrierendicken erfahren. Unter Verwendung einer Anzahl von Materialparametern, die gut mit den tatsächlichen Materialeigenschaften des verwendeten (Ga,Mn)As übereinstimmen, sowie einem Wert für die Spinpolarisierung der aus der Modellierung des diffusiven Transportregimes übernommen wurde, wird in diesem Modell der Magnetowiderstand von 2000% reproduziert.

Der übrige Teil der Arbeit beschäftigt sich mit der Untersuchung vertikaler Heterostrukturen von (Ga,Mn)As. Die hier untersuchte Au/AlOx/(Ga,Mn)As Tunnelstruktur stellt hierbei einen Vertreter einer neuartigen Klasse spintronischer Bauteile dar. Detaillierte Studien des Magnetowiderstandes bei denen das Magnetfeld unter verschiedenen Winkeln in der Probenebene angelegt wird zeigen dass es möglich ist, spinventilartige Effekte mit nur einer einzigen magneti-

schen (Ga,Mn)As Schicht zu erzielen. Dieser neuartige Magnetowiderstandseffekt wird Tunneling Anisotropic Magnetoresistance (TAMR) genannt. Ein Vergleich von Magnetowiderstandskurven unter verschiedenen Winkeln des Magnetfeldes enthüllt die für den Effekt charakteristische Winkelabhängigkeit der Breite und des Vorzeichens des spinventilartigen Rechtecksignals. Die Größe des Effektes beläuft sich auf konstant 3%, jedoch treten wie bereits erwähnt, sowohl positive als auch negative Signale auf. Es wird einwandfrei festgestellt dass das charakteristische Rechtecksignal zurückzuführen ist auf eine zweistufige Umkehr der Probenmagnetisierung in Verbindung mit einer in Bezug auf die Magnetisierungsrichtung anisotropen Zustandsdichte von (Ga,Mn)As. Durch die anisotrope Zustandsdichte hängt der Tunnelwiderstand von der Richtung des Magnetisierungsvektors **M** ab. Weiche Richtungen für die Magnetisierung in der Probe sind die [010]-Richtung und, etwas weniger ausgeprägt, die [100]-Kristallrichtung. Wenn **M** entlang [010] ausgerichtet ist, ist der elektrische Probenwiderstand niedrig und wenn **M** entlang [100] ausgerichtet ist, ist der Widerstand hoch. Ein spinventilartiges Rechtechsignal wird immer dann erzeugt, wenn die Magnetisierung während einer Messung des Magnetowiderstandes zwischen diesen beiden Richtungen hin- und herspringt.

Die Erklärung dieser Resultate basiert auf einer separaten Modellierung von magnetischer und Widerstandsanisotropie. Die magnetische Anisotropie weist einen Beitrag mit vierzähliger Symmetrie entlang der [100] und [010] Richtungen auf. Dieser Beitrag wird überlagert von einer zusätzlichen uniaxialen Anisotropie, welche die [010] Richtung bevorzugt. Ein phänomenologisches Modell das auf der Magnetisierungsumkehr mittels Domänenwänden basiert, erlaubt einen quantitativen Fit der Lage der Koerzitivfelder als Funktion des Winkels des angelegten Magnetfeldes.

Die Analyse der Widerstandsanisotropie basiert auf Berechnungen der elektrischen Zustandsdichte von (Ga,Mn)As , durchgeführt von T. Jungwirth. Das Modell beinhaltet eine biaxiale Verspannung der (Ga,Mn)As Schicht durch das darunterliegende Substrat. Zusätzlich wird ein phenomenologischer uniaxialer Verspannungsterm der Größenordnung 0.1% angenommen, um die intrinsische Symmetrie der [100] und [010] Richtungen zu brechen. Diese Verspannung führt schlussendlich zu signifikanten Anisotropien in den für den Tunnelvorgang relevanten Teilen der Zustandsdichte des (Ga,Mn)As. Das Modell zeigt, dass die Größe und sogar das Vorzeichen dieser Anisotropien empfindlich sowohl von Materialparametern wie Ladungsträgerkonzentration und Verspannung der Schicht als auch von der Beschaffenheit der Tunnelbarriere abhängen. Der besondere Einfluß der Tunnelbarriere ist dadurch zu erklären, dass die mikroskopische Beschaffenheit der Barriere effektiv eine spezifische Untermenge der anisotropen Zustandsdichte selektiert, die durch den Tunnelvorgang schlussendlich den Tunnelstrom dominiert. So sind zum Beispiel polykristalline Tunnelbarrieren in der Regel durch eine schwächere Impulserhaltung für die Impulskomponente in der Ebene der Barriere gekennzeichnet, als dies für epitaktische Barrieren zutrifft. Ein Tunnelstrom wird in der Regel durch jene Ladungsträger dominiert, deren Wellenvektoren innerhalb eines engen Kegels um die Richtung senkrecht zur Barriere liegen. Dies kommt von einer rapide absinkenden Tunnelwahrscheinlichkeit für Ladungsträger mit Wellenvektoren, die stärker von der senkrechten Richtung abweichen. Je nach Beschaffenheit der Barriere sind entweder alle Zustände innerhalb eines weit offenen ("polykristalline Barriere") oder innerhalb eines vergleichsweise engen Kegels ("epitaktische Barriere") für den Tunnelstrom verantwortlich. Auf Basis der Bandstrukturberechnungen sind hierbei größere Effekte für saubere, bzw. epitaktische Barrieren zu erwarten.

Diese Aussage wird im letzten Teil der Arbeit durch die Untersuchungen von TAMR an-

hand einer voll-epitaktischen (Ga,Mn)As/GaAs/(Ga,Mn)As Tunneldiode bestätigt. Wiederum weist der Magnetowiderstand unter verschiedenen Winkeln sowohl positive als auch negative Rechtecksignale auf, allerdings mit deutlich größerer Amplitude (300% bei T=4.2 K und niedriger Anregungsspannung). Die Symmetrie der planaren Magnetowiderstandsmessungen ähnelt sehr derjenigen der Au/AlOx/(Ga,Mn)As Probe. Wiederum gilt: wenn **M** entlang [010] ausgerichtet ist, ist der elektrische Probenwiderstand niedrig und wenn **M** entlang [100] ausgerichtet ist, ist der Widerstand hoch. Dies weist deutlich darauf hin dass auch das Transportverhalten dieser Tunneldiode von TAMR dominiert wird. Weiterhin erzeugt auch ein starkes, in der Ebene der Probe rotierendes Magnetfeld Magnetowiderstandseffekte in der Größenordnung von mehreren hundert Prozent. Während dieser Messungen sind die Magnetisierungen beider Schichten parallel ausgerichtet. Die Tatsache, dass trotzdem ein starker Magnetowiderstand auftritt ist ein direkter Beweis gegen das Vorliegen von TMR Effekten nach Julliere [Jul75]. Die Tatsache, dass Hinweise auf TMR in dieser Probe völlig fehlen legt nahe, dass früher veröffentlichte Resultate an (Ga,Mn)As -basierten TMR Proben [Hig01] eventuell im Sinne von TAMR neu interpretiert werden müssen. Zusätzlich zu dem bei 4.2 K vorliegenden Effekt von einigen hundert Prozent weist die Probe bei niedrigen Temperaturen (1.7 K) und Anregungsspannungen eine dramatische Verstärkung des Effektes auf 150 000% auf. Eine sorgfältige Untersuchung der Probeneigenschaften zeigt hier, dass die zu Grunde liegende Symmetrie von der Vergößerung der Amplitude des Effektes unangetastet bleibt. Dies legt nahe dass der TAMR Effekt bei niedrigen Temperaturen durch neu auftretende physikalische Effekte in der Bandstruktur verstärkt wird. Neuerliche Bandstrukturberechnungen zeigen, dass mit der unmodifizierten anisotropen Bandstruktur von (Ga,Mn)As Effekte von einigen hundert Prozent erklärt werden können, wie sie bei T=4.2 K auftreten. Die Modellierung für den 150 000% großen Niedertemperatureffekt ist zum gegenwärtigen Zeitpunkt noch nicht abgeschlossen. Eine der untersuchten Ursachen ist die Formierung einer Bandlücke an der Fermikante des (Ga,Mn)As wie sie von Efros und Shklovskii diskutiert wird [Efr75].

Durch die Benutzung des TAMR Effektes ist es nicht nur möglich, die Phänomenologie von TMR zu simulieren, sondern der Effekt erlaubt auch die Implementierung neuer spintronischer Funktionalitäten. Hierbei ist die hohe Empfindlichkeit einer TAMR Tunneldiode gegenüber externen Magnetfeldern zu nennen: sie erstreckt sich nicht nur auf die Amplitude sondern auch auf die Richtung eines externen Magnetfeldes. Dies eröffnet eine Reihe potentieller Anwendungsgebiete in der Magnetfeldsensorik und bei magnetischen Datenspeichern. Leider ist aber die Anwendbarkeit der denkbaren Bauelemente, soweit sie auf (Ga,Mn)As basieren, derzeit nur bei tiefen Temperaturen gegeben. Die Entwicklung neuer und geeigneter spintronischer Materialien könnte aber zukünftig Abhilfe schaffen. Ausgehend von den Erkenntnissen über TAMR in (Ga,Mn)As sollte die Suche nach diesen Materialien bei Raumtemperatur-Ferromagneten beginnen, deren Ladungsträger einer starken Spin-Bahn Wechselwirkung unterliegen.

Bibliography

[Abo01]   M. Abolfath, T. Jungwirth, J. Brum and A. MacDonald, *Theory of magnetic anisotropy in $III_{1-x}Mn_xV$ ferromagnets*. Phys. Rev. B **63**, 054418 (2001).

[Aki00]   N. Akiba, D. Chiba, K. Nakata, F. Matsukura, Y. Ohno and H. Ohno, *Spin-dependent scattering in semiconducting ferromagnetic (Ga,Mn)As trilayer structures*. J. Appl. Phys. **87**, 6436 (2000).

[Ash76]   N. Ashcroft and N. Mermin, *Solid State Physics*. Harcourt College Publishers , Fort Worth, Philadelphia (1976).

[Bai88]   M. Baibich, J. Broto, A. Fert, F. N. V. Dau, F. Petroff, P. Etienne, G. Creuzet, A. Friederich and J. Chazelas, *Giant Magnetoresistance of (001)Fe/(001)Cr Magnetic Superlattices*. Phys. Rev. Lett. **61**, 2472 (1988).

[Bar90]   J. Barnaś, A. Fuss, R. Camley, P. Grünberg and W.Zinn, *Novel Magnetoresistance Effect in Layered Magnetic Structures: Theory and Experiment*. Phys. Rev. B **42**, 8110 (1990).

[Bel05]   J. Belleson and E. Grochowski, *The Era of Giant Magnetoresistive Heads*. http://www.storage.ibm.com/hardsoft/diskdrdl/technolo/gmr/gmr.htm (2005).

[Bin89]   G. Binasch, P. Grünberg, F. Saurenbach and W. Zinn, *Enhanced Magnetoresistance in Layered Magnetic Structures with Antiferromagnetic Interlayer Exchange*. Phys. Rev. B **39**, 4828 (1989).

[Blu01]   S. Blundell, *Magnetism in Condensed Matter*. Oxford University Press Inc., New York (2001).

[Bra83]   B. Bransden and C. Joachain, *Physics of atoms and molecules*. Longman Scientific & Technical, Longman Group UK Limited,Longman House, Burnt Mill, Harlow, Essex CM20 2JE, England (1983).

[Bri70]   W. Brinkman, R. Dynes and J. Rowell, *Tunneling Conductance of Asymmetrical Barriers*. J. Appl. Phys. **41**, 1915 (1970).

[Bru99]   P. Bruno, *Geometrically Constrained Magnetic Wall*. Phys. Rev. Lett. **83**, 2425 (1999).

[Cab74]   G. Cabrera and L. Falicov, *Theory of residual resistivity of Bloch walls. I. Paramagnetic effects*. Phys. Status Solidi (b) **61**, 539 (1974).

[Cam03] R. Campion, K. Edmonds, L. Zhao, K. Wang, C. Foxon, B. Gallagher and C. Staddon, *High-quality GaMnAs films grown with arsenic dimers*. J. Cryst. Growth **247**, 42 (2003).

[Chi04] D. Chiba, F. Matsukura and H. Ohno, *Tunneling magnetoresistance in (Ga,Mn)As-based heterostructures with a GaAs barrier*. Physica E Low-Dimensional Systems and Nanostructures **21**, 966 (2004).

[Cow95] R. Cowburn, S. Gray, J. Ferré, J. Bland and J. Miltat, *Magnetic switching and in-plane uniaxial anisotropy in ultrathin Ag/Fe/Ag(100) epitaxial films*. J. Appl. Phys. **78**, 7210 (1995).

[Die00] T. Dietl, H. Ohno, F. Matsukura, J. Cibert and D. Ferrand, *Zener Model Description of Ferromagnetism in Zinc-Blende Magnetic Semiconductors*. Science **287**, 1019 (2000).

[Die01a] T. Dietl, J. König and A. H. MacDonald, *Magnetic domains in III-V magnetic semiconductors*. Phys. Rev. B **64**, 241201 (2001).

[Die01b] T. Dietl, H. Ohno and F. Matsukura, *Hole-mediated ferromagnetism in tetrahedrally coordinated semiconductors*. Phys. Rev. B **63**, 195205 (2001).

[Edm02] K. Edmonds, K. Wang, R. Campion, A. Neumann, N. Farley, B. Gallagher and C. Foxon, *High-Curie-temperature $Ga_{1-x}Mn_xAs$ obtained by resistance-monitored annealing*. Appl. Phys. Lett. **81**, 4991 (2002).

[Edm04] K. Edmonds, P. Boguslawski, K. Wang, R. Campion, S. Novikov, N. Farley, B. Gallagher, C. Foxon, M. Sawicki, T. Dietl, M. B. Nardelli and J. Bernholc, *Mn Interstitial Diffusion in (Ga,Mn)As*. Phys. Rev. Lett. **92**, 037201 (2004).

[Efr75] A. Efros and B. Shklovskii, *Coulomb gap and low temperature conductivity of disordered systems*. J. Phys. C **8**, L49 (1975).

[Fee93] R. Feenstra, J. Woodall and G. Pettit, *Observation of bulk defects by scanning tunneling microscopy and spectroscopy: Arsenic antisite defects in GaAs*. Phys. Rev. Lett. **71**, 1176 (1993).

[Fer94] A. Fert, T. Valet and J. Barnas, *Perpendicular magnetoresistance in magnetic multilayers: Theoretical model and discussion (invited)*. Journal of Applied Physics **75**, 6693 (1994).

[Fla01] M. E. Flatté and G. Vignale, *Unipolar spin diodes and transistors*. Appl. Phys. Lett. **78**, 1273 (2001).

[Gar99] N. García, M. Muñoz and Y. W. Zhao, *Magnetoresistance in excess of 200% in Ballistic Ni Nanocontacts at Room Temperature and 100 Oe*. Phys. Rev. Lett. **82**, 2923 (1999).

[Gre02] J. Gregg, I. Petej, E. Jouguelet and C. Dennis, *Spin Electronics - A Review*. J. Phys. D: Appl. Phys. **35**, 121 (2002).

[Har00]   U. Hartmann, *Magnetic Multilayers and Giant Magnetoresistance - Fundamentals and Industrial Applications*. Springer Verlag Berlin Heidelberg New York (2000).

[Hig01]   Y. Higo, H. Shimizu and M. Tanaka, *Anisotropic tunneling magnetoresistance in GaMnAs/AlAs/GaMnAs ferromagnetic semiconductor tunnel junctions*. J. Appl. Phys. **89**, 6745 (2001).

[Hua03]   S. Z. Hua and H. D. Chopra, *100,000 % ballistic magnetoresistance in stable Ni nanocontacts at room temperature*. Phys. Rev. B **67**, 060401 (2003).

[Jul75]   M. Julliere, *Tunneling between ferromagnetic films*. Physics Letters A **54**, 225 (1975).

[Ken01]   A. Kent, J. Wu, U. Rüdiger and S. Parkin, *Domain wall resistivity in epitaxial thin film microstructures*. J. Phys. Condens. Matter **13**, R461 (2001).

[Lee99]   M. Lee, J. Massey, V. Nguyen and B. Shklovskii, *Coulomb gap in a doped semiconductor near the metal-insulator transition: Tunneling experiment and scaling ansatz*. Phys. Rev. B **60**, 1582 (1999).

[Lev97]   P. Levy and S. Zhang, *Resistivity due to Domain Wall Scattering*. Phys. Rev. Lett. **79**, 5110 (1997).

[Lin97]   M. Linnarsson, E. Janzén, B. Monemar, M. Kleverman and A. Thilderkvist, *Electronic structure of the GaAs:MnGa center*. Phys. Rev. B **55**, 6938 (1997).

[McG75]   T. McGuire and R. Potter, *Anisotropic Magnetoresistance in Ferromagnetic 3d Alloys*. IEEE Transactions on Magnetics **11**, 1018 (1975).

[Moo95]   J. Moodera, L. Kinder, T. Wong and R. Meservey, *Large Magnetoresistance at Room Temperature in Ferromagnetic Thin Film Tunnel Junctions*. Phys. Rev. Lett. **74**, 3273 (1995).

[Moo03]   G. Moore, J. Ferré, A. Mougin, M. Moreno and L. Däweritz, *Magnetic anisotropy and switching process in diluted $Ga_{1-x}Mn_xAs$ magnetic semiconductor films*. J. Appl. Phys. **94**, 4530 (2003).

[Mot36a]   N. Mott, *The electrical conductivity of transition metals*. Proc. R. Soc. London, Ser. A **153**, 699 (1936).

[Mot36b]   N. Mott, *The resistance and thermoelectric properties of the transition metals*. Proc. R. Soc. London, Ser. A **156**, 368 (1936).

[Mun89]   H. Munekata, H. Ohno, S. von Molnar, A. Segmüller, L. Chang and L. Esaki, *Diluted Magnetic III-V Semiconductors*. Phys. Rev. Lett. **63**, 1849 (1989).

[Ohn96]   H. Ohno, A. Shen, F. Matsukara, A. Oiwa, A. Endo, S. Katsumoto and Y. Iye, *(Ga,Mn)As: A new diluted magnetic semiconductor based on GaAs*. Appl. Phys. Lett. **69**, 363 (1996).

[Ohn98]   H. Ohno, *Making Nonmagnetic Semiconductors Ferromagnetic*. Science **281**, 951 (1998).

[Par04]   S. Parkin, C. Kaiser, A. Panchula, P. Rice, B. Hughes, M. Samant and S. Yang, *Giant tunnelling magnetoresistance at room temperature with MgO (100) tunnel barriers*. Nature Materials **3**, 862 (2004).

[Saw04]   M. Sawicki, F. Matsukura, A. Idziaszek, T. Dietl, G. M. Schott, C. Ruester, C. Gould, G. Karczewski, G. Schmidt and L. W. Molenkamp, *Temperature dependent magnetic anisotropy in (Ga,Mn)As layers*. Phys. Rev. B **70**, 245325 (2004).

[Sch03]   G. Schott, G. Schmidt, G. Karczewski, L. Molenkamp, R. Jakiela, A. Barcz and G. Karczewski, *Influence of growth conditions on the lattice constant and composition of (Ga,Mn)As*. Appl. Phys. Lett. **82**, 4678 (2003).

[Sch04]   G. Schott, *Molekularstrahlepitaxie und Charakterisierung von (Ga,Mn)As Halbleiterschichten*. Dissertation am Lehrstuhl für Experimentelle Physik III der Bayerischen Julius - Maximilians - Universität Würzburg (2004).

[She97]   A. Shen, H. Ohno, F. Matsukura, Y. Sugawara, N. Akiba, T. Kuroiwa, A. Oiwa, A. Endo, S. Katsumoto and Y. Iye, *Epitaxy of (Ga, Mn)As, a new diluted magnetic semiconductor based on GaAs*. J. Cryst. Growth **175**, 1069 (1997).

[Shi99]   K. Shigeto, T. Shinjo and T. Ono, *Injection of a magnetic domain wall into a submicron magnetic wire*. Appl. Phys. Lett. **75**, 2815 (1999).

[Sto48]   E. Stoner and E. Wohlfarth, *A Mechanism of Magnetic Hysteresis in Heterogeneous Alloys*. Philos. Trans. London Ser. A **240**, 599 (1948).

[Szc99a]   J. Szczytko, W. Mac, A. Twardowski, F. Matsukura and H. Ohno, *Antiferromagnetic p-d exchange in ferromagnetic $Ga_{1-x}Mn_xAs$ epilayers*. Phys. Rev. B **59**, 12935 (1999).

[Szc99b]   J. Szczytko, A. Twardowski, K. Świǎtek, M. Palczewska, M. Tanaka, T. Hayashi and K. Ando, *Mn impurity in $Ga_{1-x}Mn_xAs$ epilayers*. Phys. Rev. B **60**, 8304 (1999).

[Sze81]   S. Sze, *Physics of Semiconductor devices (2nd Ed.)*. Wiley, New York page 522 (1981).

[Tan03]   H. Tang, R. Kawakami, D. Awschalom and M. Roukes, *Giant Planar Hall Effect in Epitaxial (Ga,Mn)As Devices*. Phys. Rev. Lett. **90**, 107201 (2003).

[Tho57]   W. Thomson, *On the electro-dynamic qualities of metals: Effects of magnetization on the electric conductivity of nickel and iron*. Proc. Roy. Soc. **8**, 546 (1857).

[Val93]   T. Valet and A. Fert, *Theory of the perpendicular magnetoresistance in magnetic multilayers*. Phys. Rev. B **48**, 7099 (1993).

[Vig02]   G. Vignale and M. E. Flatté, *Nonlinear Spin-Polarized Transport through a Ferromagnetic Domain Wall*. Phys. Rev. Lett. **89**, 098302 (2002).

[Wan02] K. Wang, K. Edmonds, R. Campion, L. Zhao, A. Neumann, C. Foxon, B. Gallagher and P. Main, *Anisotropic Magnetoresistance in GaMnAs films*. cond-mat/0211697 (2002).

[Weg03] J. E. Wegrowe, T. Wade, X. Hoffer, L. Gravier, J. M. Bonard and J. P. Ansermet, *Magnetoresistance of nanocontacts with constrained magnetic domain walls*. Phys. Rev. B **67**, 104418 (2003).

[Wil75] J. Wiley, *Semiconductors and Semimetals*. Academic Press, N.Y. **10**, 91 (1975).

[Yam04] M. Yamanouchi, D. Chiba, F. Matsukura and H. Ohno, *Current-induced domain-wall switching in a ferromagnetic semiconductor structure*. Nature **428**, 539 (2004).

[Yok00] Y. Yokoyama, Y. Suzuki, S.Yuasa, K. Ando, K. Shigeto, T. Shinjo, P. Gogol, J. Miltat, A. Thiaville, T. Ono and T. Kawagoe, *Kerr microscopy observations of magnetization process in microfabricated ferromagnetic wires*. J. Appl. Phys. **87**, 5618 (2000).

[Yu02] K. Yu, W. Walukiewicz, T. Wojtowicz, I. Kuryliszyn, X. Liu, Y. Sasaki and J. Furdyna, *Effect of the location of Mn sites in ferromagnetic (Ga,Mn)As on its Curie temperature*. Phys. Rev. B **65**, 201303 (2002).

[Yua04] S. Yuasa, T. Nagahama, A. Fukushima, Y. Suzuki and K. Ando, *Giant room-temperature magnetoresistance in single-crystal Fe/MgO/Fe magnetic tunnel junctions*. Nature Materials **3**, 868 (2004).

List of Publications

[1] C. Rüster, T. Borzenko, C. Gould, G. Schmidt, L.W. Molenkamp, X. Liu, T.J. Wojtowicz, J.K. Furdyna, Z.G. Yu and M. Flatté, *Very Large Magnetoresistance in Lateral Ferromagnetic (Ga,Mn)As Wires with Nanoconstrictions*, Physical Review Letters **91**, 216602 (2003).

[2] C. Gould, C. Rüster, T. Jungwirth, E. Girgis, G.M. Schott, R. Giraud, K. Brunner, G. Schmidt and L.W. Molenkamp, *Tunneling Anisotropic Magnetoresistance: A Spin-Valve-Like Tunnel Magnetoresistance Using a Single Magnetic Layer*, Physical Review Letters **93**, 117203 (2004).

[3] C. Rüster, C. Gould, T. Jungwirth, J. Sinova, G.M. Schott, R. Giraud, K. Brunner, G. Schmidt and L.W. Molenkamp, *Very Large Tunneling Anisotropic Magnetoresistance of a (Ga,Mn)As/GaAs/(Ga,Mn)As Stack*, Physical Review Letters **94**, 027203 (2005).

[4] C. Rüster and C. Gould, T. Jungwirth, E. Girgis, G.M. Schott, R. Giraud, K. Brunner, G. Schmidt and L.W. Molenkamp, *Tunneling anisotropic magnetoresistance: Creating a spin-valve-like signal using a single ferromagnetic semiconductor layer*, Journal of Applied Physics **97**, 10C506 (2005).

[5] G.M. Schott, C. Rüster, K. Brunner, C. Gould, G. Schmidt, L.W. Molenkamp, M. Sawicki, R. Jakiela, A. Barcz and G. Karczewski, *Doping of low-temperature GaAs and GaMnAs with carbon*, Applied Physics Letters **85**, 4678 (2004).

[6] M. Sawicki, F. Matsukura, A. Idziaszek, T. Dietl, G. M. Schott, C. Ruester, C. Gould, G. Karczewski, G. Schmidt and L. W. Molenkamp, *Temperature dependent magnetic anisotropy in (Ga,Mn)As layers*, Physical Review B **70**, 245325 (2004).

[7] M. Sawicki, F. Matsukura, T. Dietl, G. M. Schott, C. Ruester, G. Schmidt, L. W. Molenkamp and G. Karczewski, *Temperature Pecularities of Magnetic Anistropy in (Ga,Mn)As: the Role of the Hole Contentration*, Journal of Superconductivity **16**, 7 (2003).

[8] E. Girgis, P. Bach, C. Rüster, C. Gould, G. Schmidt, and L. W. Molenkamp, *Giant magnetoresistance in an epitaxial NiMnSb/Cu/CoFe multilayer*, Applied Physics Letters **86**, 142503 (2005).

[9] P. Bach, A.S. Bader, C. Rüster, C. Gould, C.R. Becker, G. Schmidt, L.W. Molenkamp, W. Weigand, C. Kumpf, E. Umbach, R. Urban, G. Woltersdorf and B. Heinrich, *Molecular-beam epitaxy of the half-Heusler alloy NiMnSb on (In,Ga)As/InP (001)*, Applied Physics Letters **83**, 521 (2003).

[10] A. Koveshnikov, G. Woltersdorf, J. Q. Liu, B. Kardasz, O. Mosendz, B. Heinrich, K. L. Kavanagh, P. Bach, A. S. Bader, C. Schumacher, C. Rüster, C. Gould, G. Schmidt, L. W. Molenkamp and C. Kumpf *Structural and magnetic properties of NiMnSb/InGaAs/InP(001)*, Journal of Applied Physics **97**, 073906 (2005)

[11] T. Slobodskyy, C. Rüster, R. Fiederling, D. Keller, C. Gould, W. Ossau, G. Schmidt and L.W. Molenkamp, *Molecular-beam epitaxy of (Zn,Mn)Se on Si(100)*, Applied Physics Letters **85**, 6215 (2004)

[12] C. Barglik-Chory, C. Remenyi, C. Dem, M. Schmitt, W. Kiefer, C. Gould, C. Rüster, G. Schmidt, D. M. Hofmann, D. Pfisterer und G. Müller, *Synthesis and characterization of manganese-doped CdS nanoparticles*, Phys. Chem. Chem. Phys. **5**, 1639 (2003)

Patent Application for TAMR Devices

BESCHREIBUNG

Zur internationalen Patentanmeldung PCT

(Länderbenennung gemäss separater Länderliste)

ANMELDER   ETeCH AG
c/o Dr. Bischof Pirmin, Dammstrasse 21
4502 Solothurn
Schweiz

ERFINDER   Georg SCHMIDT   Charles GOULD
Schellenberg 10   Kartause 7
97234 Lindenflur   97070 Würzburg
Deutschland   Deutschland

Laurens W. MOLENKAMP   Christian RÜSTER
Oberer Neubergweg 1   Weinbergweg 52
97074 Würzburg   97907 Hasloch
Deutschland   Deutschland

TITEL   Semiconductor device using location and sign of the spin of electrons

Lebenslauf

Persönliche Daten:

Geboren:	18. Juli 1976 in Wertheim
Staatsangeh.:	deutsch
Familienstand:	ledig

Schulische Ausbildung:

1983 - 1987	Grundschule Kreuzwertheim-Hasloch
1987 - 1996	Balthasar Neumann Gymnasium Marktheidenfeld
Jul. 1996	Abitur

Zivildienst:

1996 - 1997	Blindeninstitutsstiftung Würzburg

Studium:

1997 - 2000	Physikstudium an der Universität Würzburg
Nov. 1999	Vordiplom
2000 - 2001	Physikstudium an der State University of New York at Buffalo, USA
Feb. 2002	Master of Science in Physics, with Thesis: "Magnetotransport Studies of GaAs:Mn and $Ga_{1-x}Mn_xAs$ Alloys"

Promotionsstudium:

2001-2005	wissenschaftlicher Mitarbeiter und Promotion am Lehrstuhl EP III, Betreuer Prof. Dr. L.W. Molenkamp
WS2001 - SS2002	Student, Hf. Physik
Mai 2002	Anerkennung des Masterabschlusses als diplomäquivalent im Sinne der Promotionsordnung
SS2002 - SS2005	Student, Hf. Physik, Promotion

Erklärung an Eides statt

gemäß §5 Abs. 2 Ziff. 2 und 5
der Promotionsordnung der Fakultät für Physik und Astronomie
der Julius-Maximilians-Universität Würzburg
vom 22. September 2003

Hiermit versichere ich an Eides statt,

- dass ich die Dissertation eigenständig, d.h. selbständig und ohne Hilfe eines Promotionsberaters angefertigt und keine anderen als die angegebenen Quellen und Hilfsmittel benutzt habe.

- dass die Dissertationsschrift bisher weder in gleicher noch in anderer Form in einem anderen Prüfungsfach vorgelegen hat.

Würzburg, den 30.06.2005

(Christian Rüster)

Danksagung

Ich möchte mich bei allen Mitarbeitern des Lehrstuhls EP III für die gute Zusammenarbeit und freundliche Arbeitsatmosphäre bedanken. Insbesondere geht mein Dank an

- Prof. Dr. L.W. Molenkamp, für die Möglichkeit am Lehrstuhl EP III mit ferromagnetischen Halbleiterstrukturen arbeiten zu können, einem aufregenden und besonders dynamischen Forschungsgebiet,

- Dr. G. Schmidt als Betreuer der Gruppe Spintronik und Nanostrukturen, sowie für seinen ständigen Einsatz bei allen sich stellenden Herausforderungen der Lithographie und des Probendesigns,

- Dr. C. Gould für die kontinuierliche, intensive Betreuung und zahllose Diskussionen über wirklich jedes erdenkliche Thema,

- G. Schott für das Wachstum der (Ga,Mn)As Schichten,

- T. Borzenko und V. Hock für die Herstellung der (Ga,Mn)As Proben,

- allen oben noch nicht genannten amtierenden und ehemaligen Mitgliedern und Projektpraktikanten der (Ga,Mn)As Gruppe, A. Gröger, K. Pappert, G. Behling, D. Scheder, M. Schumm, S. Hümpfner und M. Grünewald,

- G. Manger für das Abfüllen der weit über 20000 l flüssigen Heliums, die während dieser Doktorarbeit verbraucht wurden,

- R. Ebert für die Durchführung von zahlreichen Reparaturen an der technischen Ausrüstung,

- allen technischen Mitarbeitern der Elektronik- und der Mechanik-Werkstatt.